# UNIVERSITÉ DE STRASBOURG

*ÉCOLE DOCTORALE de Physique et Chimie-Physique (ED182)*

**Institut Charles Sadron, CNRS UPR22**

# THÈSE présentée par :

## Geevarghese George

soutenue le : **17 Décembre 2020**

pour obtenir le grade de : **Docteur de l'université de Strasbourg**

Discipline/ Spécialité : Physique

---

# Propriétés rhéologiques des films polymères minces autoportants

---

**THÈSE dirigée par :**
Dr. Joachim P. Wittmer      Directeur de recherche CNRS, ICS, Strasbourg

**RAPPORTEURS :**
Dr. Anne Tanguy      Professeur, INSA Lyon
Dr. Hong Xu      Professeur, Université de Lorraine

---

**AUTRES MEMBRES DU JURY :**
Dr. Dider Long      Directeur adjoint du laboratoire mixte CNRS/Solvay, LPMA, Lyon
Dr. Pascal Hebraud      Directeur de recherche CNRS, IPCMS, Strasbourg
Dr. Fabrice Thalmann      Professeur, Université de Strasbourg

*Matha, Pitha, Guru, Deivam.*

# Acknowledgement

Several individuals have played pivotal roles in helping me complete this thesis project.

Dr. Hendrik Meyer, who introduced me to the world of polymer physics and numerical methods during my master's internship at the TSP group and primed me with the necessary skills to continue in the field of simulations.

Dr. Joachim Wittmer, my thesis supervisor, for believing in me and for all the time and effort he invested in me. I have to also acknowledge the practical recommendations he gave when something would not work, and for finding ways to keep the momentum going. He always directed me towards fruitful ideas and set the course for my thesis to progress. The past few months have been especially intense and without his help and suggestions this thesis would've been far from complete. This period has also been the most memorable and enjoyable times during my PhD as we stayed up late discussing, browsing through huge textbooks, and reworking parts of the thesis. Together we learned a lot and I am thankful for everything he helped me accomplish. Him being a person with great work ethic and keen intelligence, being his *academic descendant* is a matter of great pride to me.

Dr. Jörg Baschnagel, our team lead, has been very influential as a teacher to many and the same holds true for me. His lecture on continuum mechanics is what convinced me to apply for an internship in the group in the first place. During the first year of my PhD, he walked into the office and asked me to *fix* a data point for a film system – three years after, my entire work has become about these films! I also thank him for his recommendations that helped improve the preliminary draft of this thesis, and most importantly for his teachings and foresight.

Due credits to Joachim, Jörg and especially Dr. Alexander Semenov, for their contribution in writing down a generalized description of the fluctuations of stationary processes which has greatly influenced my outlook towards the subject, and hence the presentation of this thesis.

Dr. Olivier Benzerara, our team engineer, has been very approachable and provided supporting resources for our work to continue smoothly. I also thank him for helping me with numerous French translations, including the résumé of this thesis.

Friends/colleagues of TSP – Liudmyla, Fedir, Antony, Ricardo, Niels, Lisa, and many others – helped maintain the right ratio of fun and seriousness (me) in the office. Arghya

# Contents

# Résumé

## Introduction

Les polymères sont de larges molécules faites de la répétition de petites sous-unités appelées *monomères* [1–6]. Le nombre d´unités répétées $N$ par chaine définit le degré de polymérisation d´un polymère. Si $N$ n´est pas très grand, il est communément référé sous l´appellation *oligomère*. Tous les systèmes polymériques synthétiques ou d´origines naturelles sont constitués de plusieurs chaines de polymère $M$, de même nature chimique mais avec une certaine variabilité de longueur de chaine et de masse moléculaire. La longueur, la masse moléculaire, la nature chimique et la morphologie des différentes unités induisent la structure et les propriétés mécaniques du matériau finalement formé.

Les matériaux polymères doivent souvent être capable d´être mis en forme sous forme de couches minces de différentes épaisseurs, en fonction de leurs applications et de leurs finalités. En fonction de l´épaisseur $H$, les couches minces sont connues pour présenter de grandes différences par rapport à leur température de transition vitreuse $T_g$ [2, 7–49], particulièrement à l´échelle nanoscopique [15–21].

Mettre en forme un matériau polymère sous forme de couche mince demande à ce qu´il subisse différents régimes de températures ou même un procédé de trempe, soit en milieu confiné, soit sous la forme d´un film autoportant, en fonction du procédé de fabrication mise en œuvre. Les films minces autoportants de polymère exhibent de nombreuses propriétés physiques intéressantes, particulièrement quand elles sont couplées à la température ou à la topologie des polymères (linéaires, brosses, réticulés, etc.) [50]. Sous l'action d'une trempe, les liquides complexes vitrifiables comme les polymères ne montrent que de faibles évolutions structurales, mais l'évolution de leurs propriétés physiques[1–6] est bien plus prononcée. Ceci donne lieu à un débat intéressant sur les phénomènes physiques intervenants dans les

polymères vitreux. Le terme de *dynamique vitreuse*, qui englobe la dynamique des systèmes extrêmement lents observée dans les systèmes désordonnés autour de leur température $Tg$, n´est pas complétement compris[7–9, 15, 19, 22, 47, 49, 51–56]. C'est pour ces raisons que qu'il est important de caractériser ces phénomènes aussi bien expérimentalement que par le biais de la simulation numérique. Malgré l'importance technologique de ce type de système, de nombreuses propriétés mécaniques ou rhéologiques n'ont pas été étudiées en détails pour les couches minces de polymères [49].

Le but de cette thèse a été de simuler numériquement les couches minces de polymères et d'identifier leurs propriétés mécaniques ou rhéologiques de manières globales et locales. Le moyen principal utilisé dans cette étude est la méthode numérique de simulation de dynamique moléculaire (DM) [57, 58]. De manière simplifiée, les simulations de dynamique moléculaire fonctionnent en résolvant les équations du mouvement pour un système de particules qui interagissent au travers d´un potentiel bien défini. Notre modèle de représentation de polymères est bien connu[59–61] et référencé sous l´appellation *coarse-grained bead-spring model* [62]. Nous avons simulé les films mince autoportant (Fig. 0-1(a)) pour différentes épaisseurs en utilisant le logiciel de dynamique moléculaire LAMMPS (Large-scale Atomic Molecular Massively Parallel Simulator) [58].

# Résultats

Une des propriétés les plus basique des polymères qui puisse être mesurée expérimentalement et numériquement est la caractérisation de leur température de transition vitreuse $T_g$. En mesurant l´épaisseur des couches minces (ou de manière équivalente leur volume car dans notre cas $L$ est une constante pour l´ensemble de nos couches minces) en fonction de la température, nous permet via une expérience de dilatométrie d´observer le point d´inflexion au croisement des deux régimes linéaire pour le liquide et le solide amorphe. Ce point d´inflexion est généralement considéré comme correspondant à une pseudo-thermodynamique $T_g$ et peut-être facilement calculé pour nos modèles de couches minces comme illustré dans la Fig. 0-1(b). Un point important, présenté dans l´inclusion, une dépendance linéaire de $1/H$ en fonction de $T_g$ a aussi été observée. De nombreuses propriétés intensives $\mathcal{A}$ calculées pour nos couches minces ont aussi montré une dépendance linéaire en fonction de $1/H$. Ce comportement est attendu pour les chaînes cour-
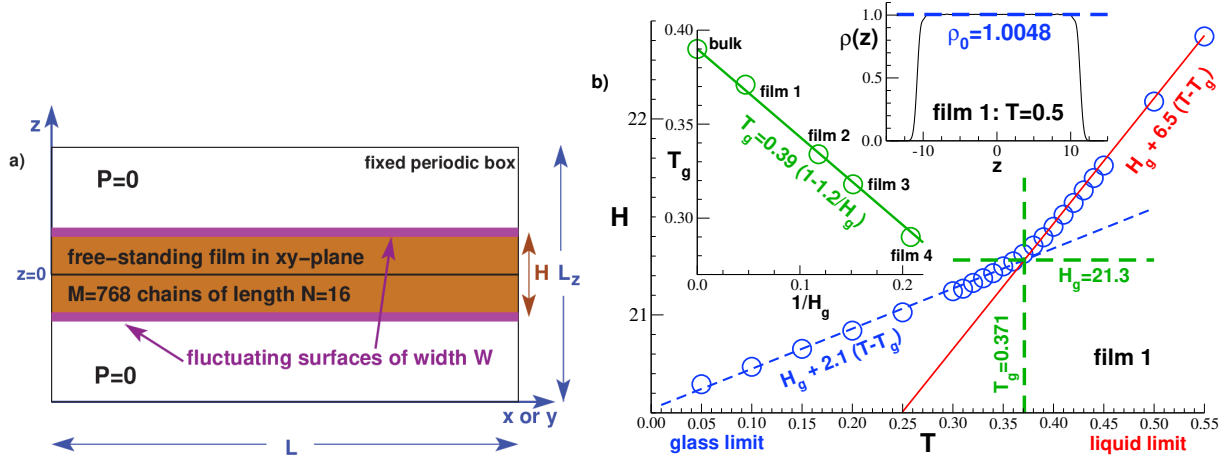
Figure 0-1: **(a)** Le protocole pour nos simulations implique un film mince de polymère auto-porté composé de $M = 768$ chaines avec chaque chaine de longueur $N = 16$, elles sont placées dans une boite de simulation tridimensionnel périodique dont la dimension latéral est fixé à $L$. L'épaisseur du film $H$ est définie selon l'axe $z$ en utilisant la méthode du "Gibbs dividing surface construction". **(b)** La température de transition vitreuse $T_{\mathrm{g}}$ peut être obtenue par dilatométrie, une méthode où un échantillon est refroidi à vitesse constante et où on mesure continuellement sa densité, cherchant à observer une rupture de pente associée à une transition. La dépendance linéaire de $T_{\mathrm{g}}$ en fonction de $1/H$ pour nos films est présentée dans le médaillon.

tes de polymères ( car leur rayon de giration $R_{\mathrm{G}} \ll H$) en considérant une description phénoménologique simple utilisant la superposition linéaire

$$\mathcal{A} \approx \frac{1}{H} \left[ \mathcal{A}_0 \ (H - W) + \mathcal{A}_s \ W \right] = \mathcal{A}_0 \left[ 1 - \frac{(1 - \mathcal{A}_s/\mathcal{A}_0)W}{H} \right]$$

d'un terme de volume $\mathcal{A}_0$ avec un poids $H - W \approx H$ et un terme de surface $\mathcal{A}_s$ avec un poids proportionnel à la largeur de la surface $W \ll H$. De manière plus générale, $\mathcal{A}$ peut être écrit comme une moyenne (possiblement avec des poids non-triviaux [47]) en fonction d'une dépendance selon $z$ de la contribution $\mathcal{A}(z)$ [30, 37, 43, 47].

L'affirmation de le correction en $1/H$ dans l'équation précédente à l'avantage de se baser sur une explication simple et transparente. Ceci peut être vu comme la contribution principale à une expansion plus générale en $1/H$. Mon Travail se focalise principalement sur une propriété mécanique importante des polymères, le module de relaxation du stress de cisaillement $G(t)$. Expérimentalement, $G(t)$ est mesuré, hors équilibre, par une expérience de réponse stresse-cisaillement. En restant dans les limites de la *réponse linéaire* et en utilisant les méthodes classiques d'analyse statistique [63–68] il est possible de calculer

ix
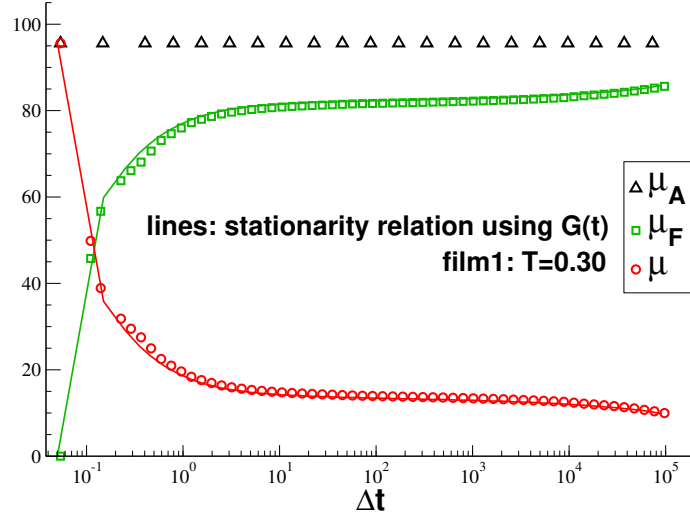
Figure 0-2: Les effets du temps d´échantillonnage pour $\mu$ et leurs contributions en se focalisant sur le *film1* et $T = 0.30$. La moyenne simple $\mu_A$ est strictement indépendante de $\Delta t$. $\mu_F$ est observé comme croissant de manière monotonique avec $\Delta t$, ce qui résulte dans une dépendance décroissante de $\mu$ en fonction de $\Delta t$, comme découlant de la formule de fluctuation du stresse. Les lignes pleines ont été obtenues en utilisant la relation stationnaire vu dans le texte principale.

numériquement $G(t)$ à partir de nos simulations numériques. Nous avons aussi calculé une dépendance générale du module de relaxation du stress de cisaillement $G(t)$ en fonction du temps d´échantillonnage $\Delta t$, appelé $\mu(\Delta t)$ en utilisant la *formule de fluctuation du stress*,

$$\mu(\Delta t) \equiv \mu_A - \mu_F(\Delta t).$$

De plus, comme observé dans la figure Fig. 0-2, la *relation stationnaire*,

$$\mu(\Delta t) = \frac{2}{\Delta t^2} \int_0^{\Delta t} \mathrm{d}t \int_0^t \mathrm{d}t' \, G(t')$$

tient pour nos couches minces à toutes les températures [66–68], ce qui implique que les valeurs attendues pour $\mu(\Delta t)$ et $G(t)$ sont numériquement équivalents. En étant une dérivée seconde sur $G(t)$, $\mu(\Delta t)$ agit une comme une fonction de lissage avec de bien meilleures propriétés statistiques que $G(t)$ (i.e. $\delta\mu \ll \delta G$). Le paragraphe suivant discutera des observations clés de notre travail.

**1) La fonction de réponse $G(t)$ et le module de stresse généralisé $\mu(\Delta t)$:** Nous avons calculé la valeur moyenne de la fonction de relaxation du stresse de cisaillement $G(t)$

(Fig. 0-3(a)) et la moyenne du module de stresse généralisé $\mu(\Delta t)$ pour une large gamme de températures et d´épaisseurs de couches minces [63–70] en utilisant la formule de fluctuation du stresse. En utilisant le principe de superposition temps-température, *Time Temperature Superposition (TTS)* [1], nous avons aussi démontré une loi d´échelle valide de type TTS pour $\mu(\Delta t)$ (Fig. 0-3(b)). En utilisant des facteurs de déplacement horizontaux utilisés pour obtenir la loi d´échelle TTS, nous avons estimé la viscosité de cisaillement $\eta$ et le temps de relaxation *relatif* alpha pour l´ensembles des couches minces. En accord avec de nombreux résultats expérimentaux qui ont été publiés [7–10, 12, 13, 27–33, 35, 36, 39–41, 45, 47–49], nous avons montré que de nombreuses propriétés intensives de nos couches minces, dépendent linéairement comme l´inverse de l´épaisseur de la couche $1/H$. Ceci indique qu´il y a une superposition linéaire des propriétés de volume et de surface [56, 71], ceci peut être résolu par une analyse effectué plan par plan de ces propriétés dans l´épaisseur de la couche mince.

**2) Transformation numérique de $G(t)$:** Le module de relaxation du cisaillement $G(t)$ a été transformé [1, 5, 72, 73] en des composants de stockage $G'(\omega)$ et de perte $G''(\omega)$ du module dynamique $G^\star(\omega)$ en utilisant des techniques classiques. A partir des asymptotes à basse fréquence de $G'(\omega)$ et $G''(\omega)$, comme présenté dans la figure 0-4(b), nous obtenons pour les températures les plus hautes la viscosité de cisaillement $\eta$ et l´état stationnaire du fluage $J_e^0$. Ceci donne une nouvelle voie pour mesurer le temps de relaxation alpha $\tau_{\alpha,1} = J_e^0 \eta$. Ceci a été utilisé pour fixer la valeur *absolue* de l´échelle de temps de la relaxation terminale $\tau_\alpha(T)$ obtenue par le moyen de la renormalisation TTS. Le temps de croisement $\tau_\times(\lambda = 3)$ obtenu à partir du premier croisement de $\lambda G'(\omega)$ et $G''(\omega)$ donne une voie plus directe et numériquement solide (La statistique étant meilleur au valeur intermédiaire -$\omega$) pour l´estimation de $\tau_\alpha$ au dessus de $T_g$.

Comme montré dans la figure. 0-4(a), nous avons de manière additionnelle vérifié l´équivalence entre la viscosité de cisaillement$\eta$ obtenu par plusieurs méthodes de calcul indépendantes – relation de Green-Kubo, relation de Einstein-Helfand, Superposition TTS et l´asymptote de $G''(\omega)$ à faible valeur de $\omega$ – pour le *film1*. Nous avons aussi vérifié que pour nos couches minces le comportement de type Vogel-Fulcher-Tammann (VFT) était maintenu.

Finalement nous avons effectué un transformation direct [5, 73] de $G(t)$ pour obtenir le
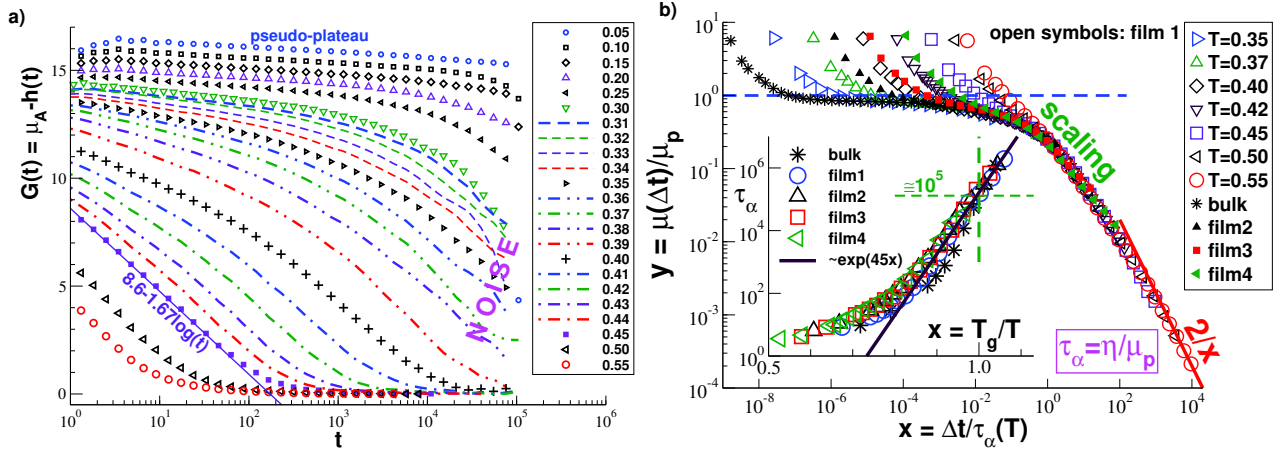
Figure 0-3: **(a)** Module de relaxation du stresse $G(t)$ en utilisant une représentation semi-logarithmique. Aucune indication d'un saut singulier respectivement à la température n'a été observé. $G(t)$ croît continuellement en fonction de la décroissance de $T$. Pour certaines températures au dessus de $T_g$ le module de relaxation est approximativement représenté par $G(t) = a - b\log(t)$ comme indiqué pour $T = 0.45$ (la ligne pleine). **(b)** Méthode TTS pour $y = \mu(\Delta t)/\mu_p$ en fonction de $x = \Delta t/\tau_\alpha(T)$ avec $\mu_p$ le plateau du module et $\tau_\alpha(T)$ le temps de relaxation indiqué dans le médaillon. Nous imposons $\tau_\alpha(T = 0.55)$ pour obtenir l'échelle de temps absolue. Les deux asymptotes de la fonction $y = f(x)$ pour $x \ll 1$ et $x \gg 1$ sont indiquées par les lignes hachurées et pleines. Nous avons une superposition des temps de relaxation terminaux $\tau_\alpha$ $vs$ $x = T_g/T$ pour tous nos températures.

fluage $J(t)$, qui a été ensuite comparé avec le fluage mesuré dans l´expérience d´expansion de micro-bulles [19]. Il a été montré que notre modèle est en agrément avec les résultats expérimentaux obtenus dans le régime du domaine vitreux. Dans le régime du fluide, nos chaines courtes de notre modèle sont bien sur incapable de révéler un *plateau caoutchouteux*.

**3) Module local de cisaillement dans le formalisme de fluctuation du stresse:** Basé sur l´hypothèse simple d´un modèle à deux couches [56, 71], il suggère une couche pseudo-liquide au niveau l´interface libre des couches minces [74], nous avons calculé le module *local* de cisaillement $\mu(z)$ pour notre couche mince la plus épaisse. En nous focalisant sur la distribution en fonction de la position en $z$, dont la contribution est supposée *linéairement additive* à la somme des propriétés de nos couches minces, nous avons vérifié par nos résultats que cette assomption est valide. En accord avec d´autres résultats de travaux expérimentaux et numériques [24, 43, 56, 75, 76], nous avons observé une décrois-sance du module de cisaillement à la surface de nos couches minces (représenté par les flèches de la Fig. 0-5). Il semble aussi que l´épaisseur de l´*interface souple*, croit en fonc-
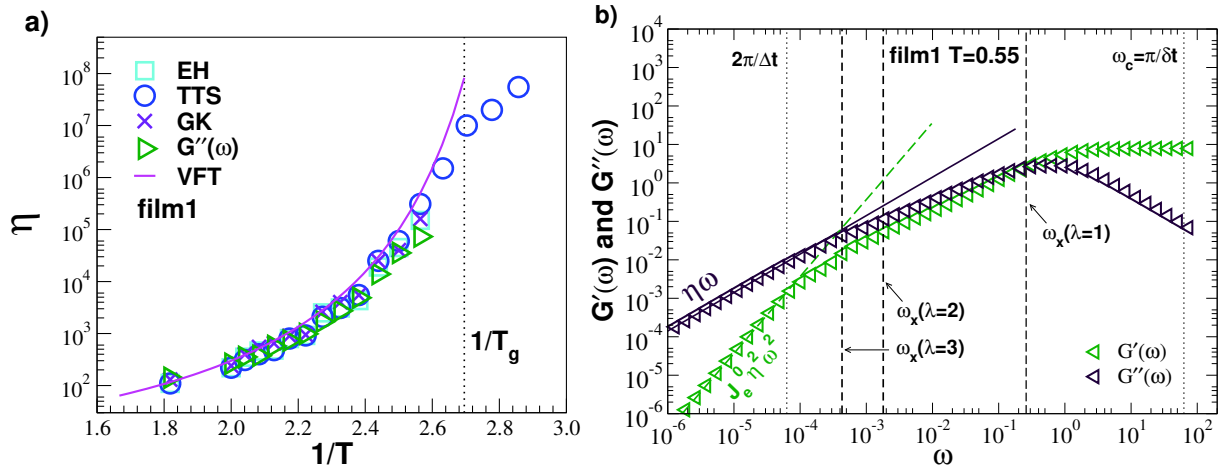
Figure 0-4: Viscosité de cisaillement $\eta$ pour le *film1* pour différentes températures $T$: **(a)** Comparaison de $\eta$ obtenu par les méthodes de la relation de Einstein-Helfand (EH), la renormalisation TTS, la relation de Green-Kubo (GK) et pour la limite des faibles valeurs de -$\omega$ pour $G''(\omega)$. Le données sont exprimées en fonction de *vs*, l'inverse de la température en utilisant une représentation semi-logarithmique. La ligne pleine indique un fit de type Vogel-Fulcher-Tammann. **(b)** $G'(\omega)$ et $G''(\omega)$ obtenus en utilisant une transformation numérique de $G(t)$- pour $T = 0.55$ et pour le *film1*, quand $\eta \approx 141$, $J_e^0 \approx 18.5$ et $\tau_{\alpha,1} \approx 2604$. La fréquence de croisement $\omega_\times(\lambda) = 1/\tau_\times(\lambda)$ pour les ratios $\lambda = 1$, $\lambda = 2$, et $\lambda = 3$ sont indiqués par les lignes pointillées verticales. Noté que $\omega_\times(\lambda = 3)$ correspond précisément à la fréquence de croisement $1/\tau_{\alpha,1}$ des deux asymptotes pour les valeurs faibles de -$\omega$ pour $G'(\omega)$ et $G''(\omega)$.

xiii
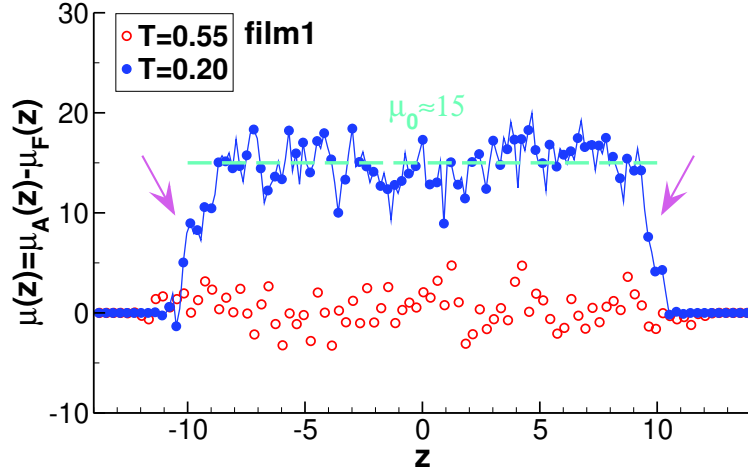
Figure 0-5: Distribution $\mu(z) \equiv \mu_{\mathrm{A}}(z) - \mu_{\mathrm{F}}(z)$ du module de cisaillement pour le *film1* et deux températures. Quand $\mu(z)$ disparait dans la limite liquide ( cercles ouverts), il devient constant en dessous de $T_{\mathrm{g}}$ avec un plateau dans la phase de volume au milieu des couches minces (ligne horizontale pointillée) prise en sandwich entre 2 couches plus flexibles marquées par les flèches.

tion de $T$. Le point principal qui émerge de ces résultats est l´évidence que la dépendance linéaire en $1/H$ des propriétés globales des couches minces vient de la contribution résolut en $z$ et supporte le modèle en deux couches [56, 71].

**4) Fluctuations d´ensemble de la function de réponse et du module de cisaille-ment:** Notre fonction de réponse linéaire $G(t)$ ou de manière équivalente $\mu$ est caractérisée par de forte fluctuations, particulièrement aux alentours de $T_{\mathrm{g}}$. Comme montré dans la Fig. 0-6(a), $\delta\mu(T) \ll \delta G(T)$ tiennent et ils sont non-monotones avec les importantes variations juste en dessous de $T_{\mathrm{g}}$. Pour des températures pas trop faibles ce comportement peut être compris en assumant que les séries temporelles du stresse instantané de cisaille-ment $\hat{\tau}$ sont stationnaires, gaussiennes et ergodiques. Comme les systèmes deviennent non-ergodique à basse température, ceci conduit à un comportement qualitativement dif-férent où $\delta\mu(\Delta t)$ devient constant, $\delta\mu(\Delta t) \to \Delta_{\mathrm{ne}}$, même pour des temps d´échantillonnage importants $\Delta t$ [69, 70, 77]. Nous observons que $\delta\mu \approx \delta\mu_{\mathrm{G}}$ devient large pour $\Delta t$ correspon-dant aux temps de relaxation $\tau_\alpha$ où $G(t)$ varie fortement (Fig. 0-6(b)). Il est aussi clair que $\delta\mu$ et $\delta\mu_{\mathrm{G}}$ diffèrent dans la limite non-ergodique pour les faibles températures.
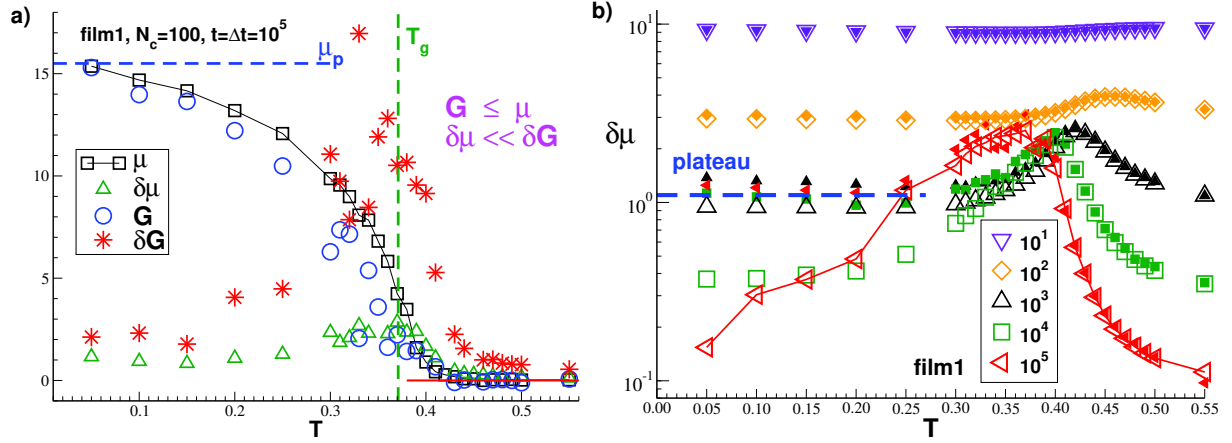
Figure 0-6: **(a)** Le module généralisé du stresse de cisaillement $\mu$, la fonction de réponse du stresse de cisaillement $G$ et les déviations standard correspondantes $\delta\mu$ et $\delta G$ prisent à $t = \Delta t = \Delta t_{\text{max}} = 10^5$ comme fonctions de $T$. Les deux inégalités observées $G \leq \mu$ et $\delta G \gg \delta\mu$ sont toutes les deux des conséquences de la relation de stationnarité. Les barres d´erreurs correspondantes $\delta\mu/\sqrt{N_c - 1}$ et $\delta G/\sqrt{N_c - 1}$ ne sont pas présentées. **(b)** Dépendance en $T$ pour des différents $\Delta t$ avec deux types de fluctuations du module de cisaillement $\mu$: $\delta\mu_{\text{Gauss}}$ (symboles ouverts) et $\delta\mu_{\text{F,tot}}$ (symboles pleins). Bien que $\delta\mu_{\text{Gauss}} \approx \delta\mu_{\text{F,tot}}$ pour les petites valeurs de $\Delta t$ et l'ensembles des $T$, elles diffèrent toutes les deux pour les températures inférieures à $T_{\text{g}}$ et pour les valeurs élevées de $\Delta t$.

# Conclusion

Nous avons réussi à démontrer que de nombreuses propriétés mécaniques et rhéologiques peuvent être estimées *numériquement* pour les couches minces de polymères linéaires, tel que le module de relaxation du cisaillement $G(t)$ la viscosité dynamique $\eta$ grâce au formalisme de la réponse linéaire des fluctuations du stresse.

De manière additionnelle, Nous avons montré qu´il existe une dépendance linéaire en fonction de $1/H$ pour de nombreuses propriétés suggérant que les effets de surface jouent un rôle important. L´analyse résolue en couche de $\mu$ montre que le module est plus faible à l´interface en comparaison du centre des couches minces. Cette *soft interface* clarifie pour nous les nombreuses dépendance en $1/H$ observées dans nos travaux. Nous avons aussi défini l´échelle pour le *relatif* temps de relaxation alpha $\tau_\alpha$ obtenu à partir de l´approche TTS de $\mu(\Delta t)$. De plus, nous avons comparé nos résultats avec les travaux expérimentaux de Ref. [19] et noté que la correspondance ne vaut que pour le régime vitreux. Finalement, nous avons caractérisé les fluctuation de notre fonction de réponse linéaire $G(t)$ dans des termes généraux en assumant un processus gaussien stationnaire (à l´équilibre)

et stochastique. Nous ne sommes pas au courant de travaux systématiques expérimentaux ou numériques de caractérisation de la réponse *step-strain* $\delta G$ ou $\delta \mu$, spécialement pour les liquides vitrifiables ou les solides amorphes. Nos affirmations que $\delta G/G$ ou $\delta \mu/\mu$ doivent généralement devenir larges (de l´ordre de l´unité) pour des temps où $G(t)$ décroit fortement, peut être source d´erreurs pour la compréhension des propriétés mécaniques et rhéologiques des *vrai* matériaux macroscopiques. Du point de vu théorique il est actuellement mal définis comment généraliser les relations de fluctuation-dissipation connectant la moyenne de la réponse linéaire hors équilibre à la moyenne de la relaxation à l´équilibre pour décrire les fluctuations entre différents échantillons.

## Perspectives

Il y a différentes pistes qui peuvent être poursuivis comme continuation de nos travaux. Tout d'abord, des simulations numériques avec $N \gg N_e$ peuvent être réalisées. Les processus dynamiques discutés dans ce manuscrits de thèse sont supposés se comporter de manières proches aux résultats expérimentaux [19] pour les valeurs larges de $N$. Le ralentissement induit de la relaxation par l´enchevêtrement va nous confirmer si la présence d´un plateau *caoutchouteux* pour la réponse de fluage $J(t)$. D´autres structures de polymères peuvent être explorées [50] et réagir de manières différentes à nos polymères linéaires.

Des simulations hors-équilibres peuvent être réalisées où un cisaillement infinitésimale est appliqué dans le plan $xy$ pour mesurer $G(t)$ ou quand un stresse constant et infinitésimale est appliqué selon $x$ et $y$ pour mesurer la réponse bi-axial $D(t)$ comme dans les protocoles expérimentaux.

Dans nos simulations, nous nous sommes focalisés aussi sur les variations de $\Delta t$ and $T$ tout en gardant les autres paramètres comme le nombre de particules dans notre système $n = N \times M \approx V$ constants. La plupart des propriétés discutées dans ce manuscrit $\mu_\mathrm{A}$, $\mu_\mathrm{F}$, $\mu$ or $h(t)$ sont définies comme des propriétés intensives, et leurs valeurs moyennes *ne doivent pas* essentiellement dépendre de la taille du système modélisé $n$ ou de son volume $V$. Cet aspect doit être vérifié pour nos couches minces. De plus, des études récentes conduits dans notre groupe de recherche sur les déviations standards des propriétés précédemment mentionnées ont montré une dépendance non triviale à la taille du système pour les systèmes non-ergodiques [69, 70, 77], et ceci doit être vérifié.

# Chapter 1

# Introduction

## 1.1 Polus meros

We know that *polymers* are macromolecules [1–6] composed of small repetitive sub-units, called *monomers* [6]. The number of repeating units $N$ per chain defines the degree of polymerization of the polymer. If $N$ is not very large, it is also quite common to refer to it as an *oligomer*. All systems of synthetic and naturally occurring polymers are composed of several polymer chains $M$ of the same chemical type with variable lengths and molecular weights. The length, molecular weight, chemical nature, and the morphology of the units impart specific structure and mechanical property to the material that is finally formed.

Polymers also demonstrate characteristically different properties based on whether we are above/below their *glass transition* temperature ($T_{\mathrm{g}}$) [7–9, 15, 22, 47, 49, 51–54]. Above $T_{\mathrm{g}}$, they are unstable melts, which means a low *modulus*; whereas below $T_{\mathrm{g}}$, they form amorphous (glassy) solids, with a finite modulus. Polymers can be made into films of varying thicknesses. Based on the thickness $H$, they are known to show characteristically different $T_{\mathrm{g}}$ [2, 7–49]. This effect is especially dramatic in the nanometric scale [15–21]. Distinguishing the temperature and thickness dependencies of polymer films are therefore of interest. For instance, in the processing of polymers to manufacture LEGO bricks, it is crucial to know how and when a thick/thin extrudate flows/freezes, before being injection molded into their final forms. The central theme of this thesis is thus to investigate mechanical and rheological properties of *freestanding polymer films* using general theoretical arguments and molecular dynamics (MD) simulations [57, 78].

1

In the following section we will summarize relevant advancements in measuring mechanical properties of polymer films over the past couple of decades. We will then briefly discuss our approach (Sec. 1.3) and summarize a few of our central findings in Sec. 1.4. Finally, in Sec. 1.5, we will provide an outline of this thesis.

## 1.2   Status quo

A general understanding is that the large surface to volume ratio of polymer films [51] impart attractive structural and dynamical properties in comparison to the bulk polymer – therefore finding its use in varied applications. The case of *lab-on-a-chip* (microfluidics) technology which has global health implications [79–81] is a great example that illustrates the need to study thin polymer films. Polystyrene (PS), polycarbonate (PC), and polymethyl methacrylate (PMMA) are some common thermoplastics that are used in this domain. These microelectromechanical chips are constantly undergoing miniaturization (with nanoscale features) to add various functionalities to the end product [19, 82–84]. Polymers, being a vital component in this technology, specifically in their thin-film geometry, has been a topic of discussion ever since. This interest is mainly due to the anomalous properties exhibited by such a geometry [2, 7–16, 19–49]. Firstly, there is no clear consensus on the thickness ($H$) dependence of the $T_g$ for thin polymer films. Secondly, based on whether the film is freestanding or supported, the $H$-dependence seems to vary. Finally, the type of measurement used to determine $T_g$ also seem to give different results. It is important to understand $T_g$ better as it dictates the processability, performance and properties of the final product. For these reasons, the glass transition emerges as one of the most interesting problems of our times.

As stated previously, the overall physics of the polymer changes near the glass transition temperature. It is a common approach to study the viscoelasticity (or mechanical response) to characterize the $T_g$ [31, 85]. Some of the well-known experimental techniques[1] that have been employed to understand the viscoelasticity of polymer films are as follows:

- nanobubble inflation method that measures the biaxial stretching [1] of a bubble formed by ultra thin polymer films by applying constant pressure through nanopores to calculate the biaxial creep compliance [17–19];

---

[1]Please note that the limitations of some of these methods are described elsewhere [49, 53, 54].

- spontaneous particle embedment method, where a submicron particle is embedded into the thin film, the viscoelastic nature of the film allows for embedment of the particle with time. Using the JKR (Johnson, Kendall, and Roberts) model [86], the force on the particle is related to the work of adhesion, and is used to calculate the modulus of the surface [87, 88];

- film dewetting method, where the surface energy difference between film and supporting liquid causes the film to uniformly shrink (homothetic deformation), while the thickness remains uniform. Creep compliance is then directly measured after verifying that the strain is linear with the surface tension induced stress [23];

- AFM based nanoindentation method, where the indentation probe is brought in contact with the free surface of the film to determine the elastic moduli [89];

- analyzing the wrinkling pattern (number, length of wrinkles, contact angle and bending modulus) formed on a free floating film placed on the water surface by the water droplet (of varying volumes in $\mu l$) on the film surface also gives a measure of the modulus [90].

While these methods do not point to a unique conclusion, reported trends from the extensive viscoelastic characterization of polymer films are that:

- below 100nm, for freestanding and supported PS films, $T_{\mathrm{g}}$ is seen to decrease with $1/H$. Note that this effect is not universal and that it will depend on the material and its interaction with the substrate;

- experiments performed on *glassy* ($T \ll T_{\mathrm{g}}$) PS films tells that there exists a $3-4$nm *soft* layer at the surface of the film, where a reduction of $T_{\mathrm{g}}$ in comparison to the center of the film is seen;

- supported films show an enhanced surface stiffness (up to 200%) at the free interface in comparison to the bulk.

From the vast number of experimental and numerical studies, it has been possible to understand the above effects to a certain extent [7–10, 12, 13, 27–33, 35, 36, 39–41, 45, 47, 48]:

- the *dramatic* depression in $T_g$ for freestanding films implies that there is an increased mobility of chains at the free interfaces. The magnitude of decrease in $T_g$ is reduced for supported films (in comparison to freestanding films) due to strong interactions with the substrate [17–19, 53, 56, 91];

- the increased mobility at the interface causes a reduction in the surface modulus, creating a *liquid–like* surface [56], and vice versa [43, 88];

- the low energy of activation (measured via lateral force microscopy) at the surface increases the mobility of the chains at the surface [92]; Globally, the energy barriers in freestanding films is lower than in bulk polymers [91, 93].

- there exists a heterogeneity in the dynamics of aggregates creating a mobility gradient within the film [75, 93, 94]. These *cooperatively rearranging regions* (CRR) diffuse from the surface into the bulk, coupling the relaxation at the mobile surface to the bulk of the film. Below $T_g$, slow–dynamics aggregates dominate contributing to the macroscopic viscosity and above $T_g$ the segmental diffusion is dominated by fast–dynamics aggregates [31, 85].

Results from neutron scattering, that probed the mean square displacement of supported thin films, showed that there is a retarded mobility of chains at the free interface, compared to the bulk [52]. An decreased mobility means an increase in $T_g$ and mechanical stiffness, which goes against our understanding of dynamics of the free surface. Whereas, the direct measurement of $T_g$ using fluorescence methods [22] has proven otherwise. In general, most experimental studies on freestanding thin films unanimously agree that there is a reduction in $T_g$ with reducing thickness [49, 53, 54]. However, only a small number of numerical studies exist at present focusing on the mechanical properties of freestanding films [38, 41–44, 46, 48]. Attempting to fill this gap, we focus on the characterization of various mechanical and rheological properties of freestanding polymer films.

## 1.3   Our approach

Using MD simulation [57, 78] of a coarse-grained bead-spring model [58, 95] we have investigated the *total* shear response function $G(t)$ and shear moduli $\mu$ of our freestanding
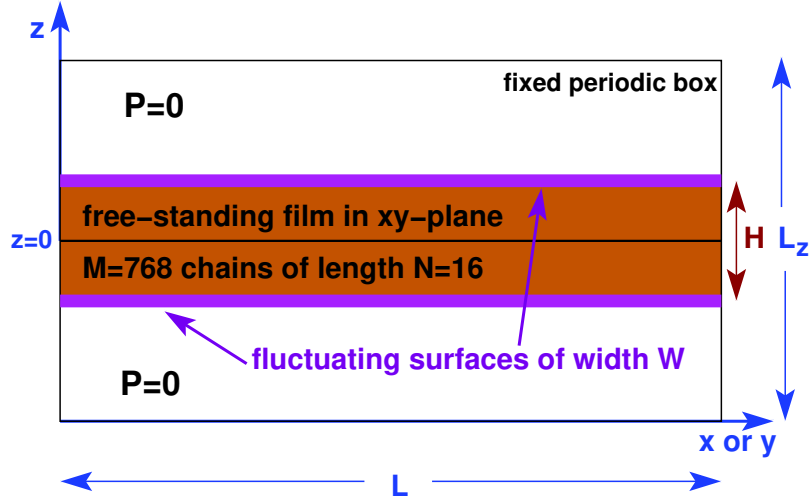
Figure 1-1: We study free-standing polymer films with $M = 768$ oligomer chains of length $N = 16$ monomers confined in periodic boxes with $L$ being the imposed lateral box size in both $x$ and $y$ directions. The film thickness $H \sim 1/L^2$ (to leading order) is operationally defined using the Gibbs dividing surface [57] as shown in Sec. 4.2.

polymer films to understand their $H$-dependent behavior. In Fig. 1-1, we present our simulation setup. We note that our films are suspended parallel to the $xy$ plane in the simulation box. To prepare films of varying thicknesses we do not directly vary $H$, but rather impose a lateral box width $L$ in both $x$ and $y$ directions. The thickness at the glass transition temperature, $H(T = T_\mathrm{g}) = H_\mathrm{g}$, of our films varies from *film1* (thickest, $H = 21.3$ LJ units) to *film4* (thinnest, $H = 4.8$ LJ units). More details on film preparation and film properties are given in Sec. 3.4. The thermodynamic equilibrium shear modulus $\mu$ is the long-time limit of the shear-stress relaxation modulus $G(t)$, i.e. the ratio of the measured shear stress $\tau(t)$ and the imposed (infinitesimal) simple shear strain $\gamma$. We remind that $\mu = 0$ for simple or complex liquids $T \gg T_\mathrm{g}$. Following the pioneering work of Barrat *et al.* [64] and related studies on elastic properties [63–67, 95–102], we determine the shear modulus $\mu$ by means of the *stress-fluctuation formula*

$$\mu \equiv \mu_\mathrm{A} - \mu_\mathrm{F} \qquad (1.1)$$

as described in detail in Appendix B. Here, $\mu_\mathrm{A}$ stands for the "affine shear modulus" (Appendix B.1) and $\mu_\mathrm{F}$ for the (rescaled) variance of the shear stresses.

5
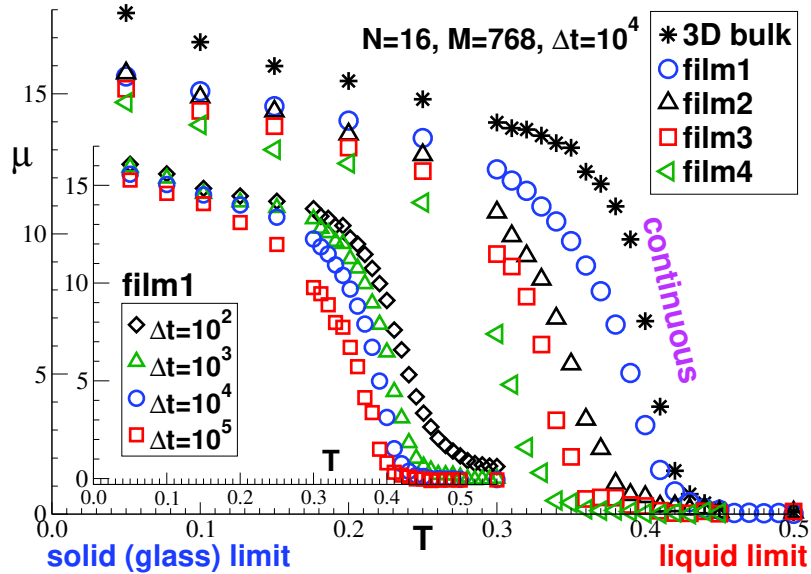
Figure 1-2: Shear modulus $\mu$ as calculated by means of Eq. 1.1. $\mu(T)$ decays continuously in all cases considered. Main panel: Data obtained at a sampling time $\Delta t = 10^4$ for three-dimensional bulks (stars) and films of different $H$. The thickness at $T_{\mathrm{g}}$ ($H_{\mathrm{g}}$) of our films varies from *film1* (thickest $H = 21.3$ LJ units) to *film4* (thinnest $H = 4.8$ LJ units). See Table 3.1 for static properties of these films. Inset: $\mu(T)$ for *film1* comparing different sampling times $\Delta t$.

## 1.4  Some key findings from our study

Summarizing our key findings we present $\mu(T)$ in Fig. 1-2 for different systems (main panel) and sampling times $\Delta t$ (inset). Primarily, we observe that, for the same $\Delta t$, $\mu(T)$ decays *continuously* from the glassy limit to the liquid limit, for all our films (and the 3D bulk system studied in Ref. [103]). In addition, it is seen that $\mu$ reduces for low-$T$ as the film gets thinner, which implies the existence of a *soft* surface. As $H$ reduces, the (low) surface contribution of $\mu$ dominates, which in effect reduces the global $\mu$ of the film. As in the previous work carried out in our group [63, 65–67, 99–101], we find that $\mu$ depends on the sampling time $\Delta t$ for our films. The $\Delta t$-dependence of the generalized shear modulus $\mu(\Delta t)$ can be traced back to the stationarity relation

$$\mu(\Delta t) = \frac{2}{\Delta t^2} \int_0^{\Delta t} \mathrm{d}t \int_0^t \mathrm{d}t'\, G(t') \tag{1.2}$$

as discussed in more detail in Sec. 2.3 and Sec. 2.4.2. Being a second integral over $G(t)$, $\mu(\Delta t)$ is a convenient smoothing function with much better statistical properties than $G(t)$.

This point will be further discussed in Sec. 2.4.2 and Sec. 7.2. As emphasized in the inset of Fig. 1-2, the effect of sampling time is more pronounced for intermediate temperatures, especially around $T_{\mathrm{g}}$. The stationarity relation Eq. 1.2 holds for all temperatures, i.e. the expectation values of $\mu(\Delta t)$ and $G(t)$ are numerically equivalent.

As we shall see in Ch. 7, this is not the case for their standard deviations $\delta\mu$ and $\delta G$ for which $\delta\mu(T) \ll \delta G(T)$ holds. $\delta\mu(T)$ and $\delta G(T)$ are seen to be non-monotonic with strong peaks slightly below $T_{\mathrm{g}}$. For not too low temperatures this behavior can be understood by assuming that the time series of instantaneous shear stresses $\hat{\tau}$ are stationary, Gaussian and ergodic stochastic processes. Since the systems become non-ergodic at low temperatures, this leads to a qualitatively different behavior where $\delta\mu(\Delta t)$ becomes constant, $\delta\mu(\Delta t) \rightarrow \Delta_{\mathrm{ne}}$, even for large sampling times $\Delta t$.

The numerical transformation of our response function $G(t)$ (cf. Appendix D) to the creep compliance $J(t)$ will allow a comparison with the nanobubble inflation experiment [19]. It will be shown in Ch. 5 that our model agrees with the experimental findings only in the glassy regime, whereas in the liquid regime our oligomer chains understandably do not reveal a *rubbery plateau*.

Following the two-layer model phenomenology observed in experiments [49, 56], suggesting a liquid–like layer at the free interface of films [74], we calculated the *local* shear modulus of our systems. Focusing on local $z$-distributions, which are *linear-additive* contributions of the total film properties, we verify that this assumption is indeed valid. Many intensive properties $\mathcal{A}$, such as $T_{\mathrm{g}}$, $\mu_{\mathrm{A}}$ or $\mu_{\mathrm{F}}$, are thus seen to depend linearly on the inverse film thickness $H$. This is expected for small chains (having a gyration radius $R_{\mathrm{G}} \ll H$) assuming as the simplest phenomenological description the linear superposition

$$\mathcal{A} \approx \frac{1}{H}\left[\mathcal{A}_0\,(H-W) + \mathcal{A}_s\,W\right] = \mathcal{A}_0\left[1 - \frac{(1-\mathcal{A}_s/\mathcal{A}_0)W}{H}\right] \tag{1.3}$$

of a bulk term $\mathcal{A}_0$ with a weight $H - W \approx H$ and a surface term $\mathcal{A}_s$ with a weight proportional to the surface width $W \ll H$. Even more generally, $\mathcal{A}$ may be written as an average (possibly non-trivially weighted [47]) over $z$-dependent contributions $\mathcal{A}(z)$ as done, e.g., for the $T_{\mathrm{g}}$ [30, 37, 47] or the storage and loss moduli $G'(\omega)$ and $G''(\omega)$ [43]. The claimed $1/H$-correction, Eq. 1.3, has merely the advantage to be based on a simple and transparent idea. It may be seen as the leading contribution of a more general $1/H$-
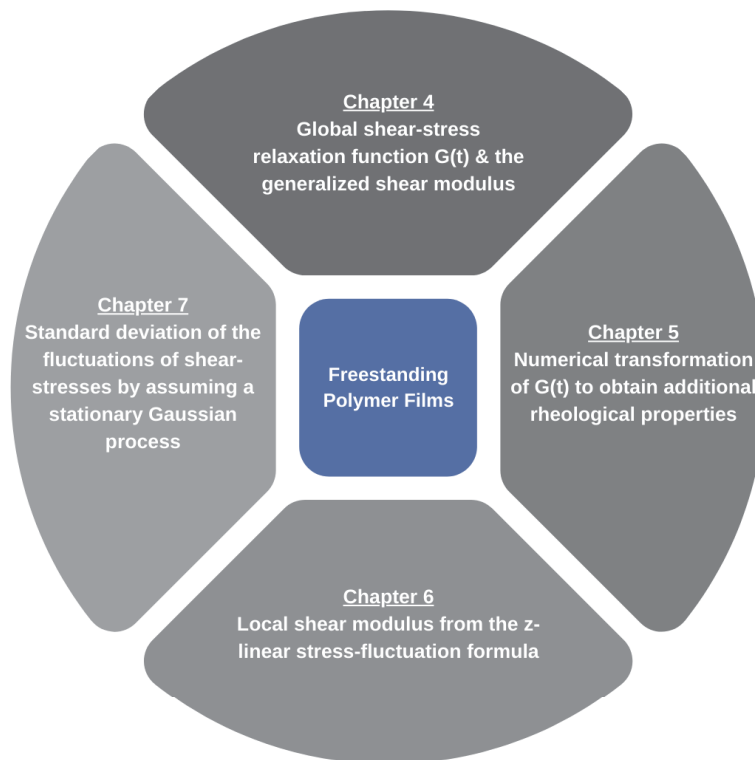
Figure 1-3: The central theme of this thesis revolves around freestanding thin polymer films in the glassy and liquid limits. We perform numerical simulations to compare our results qualitatively and quantitatively with the literature and study anomalous effects that have been reported around $T_{\mathrm{g}}$.

expansion. We remind that other $H$-dependencies have been suggested [27, 29, 30, 74] and fitted with some success [35–37, 39].

## 1.5   Thesis outline

The goal of my thesis is to simulate freestanding thin polymer films and to identify their mechanical and rheological properties both globally and locally, and to also describe the fluctuations of some of these properties. As sketched in Fig. 1-3 the central aspects my thesis tries to highlight are

- to study the shear-stress relaxation modulus $G(t)$ and the *generalized* shear modulus $\mu(\Delta t)$ of thin freestanding polymer films (Ch. 4);

- to determine their shear viscosity, complex modulus and the shear compliance (Ch. 5)

using numerical transformation methods (Appendix D);

- to measure the local, layer-resolved modulus $\mu(z)$ of our films using the stress-fluctuation formalism so as to explain the $H$-dependence of $\mu(\Delta t)$ and $\eta$ (Ch. 6);

- to understand the observed strong fluctuations of the linear response function $G(t)$ and $\mu$. This will be done by first considering quite generally the fluctuations of variances of stochastic Gaussian processes (Sec. 2.5) and by testing then some of these relations for our films (Ch. 7).

The remainder of the thesis is structured as follows: Chapter 2 introduces general theoretical considerations of sampling time dependent properties. We discuss in turn various concepts and relations related to the stationarity of stochastic processes (Sec. 2.3), to the linear response of thermalized systems to external perturbations (Sec. 2.4.1), to Gaussian fluctuations of ergodic stochastic processes (Sec. 2.5), to effects caused by an (effective) non-ergodicity of the process (Sec. 2.6) and, finally, to the scaling of various properties with the system size (Sec. 2.7). Chapter 3 presents the algorithmic and computational details. We define the simulation model in Sec. 3.2 and Sec. 3.3 and specify then in Sec. 3.4 and Sec. 3.6 the film preparation (quench protocol) and the data processing methods that we employed. The Irwing-Kirkwood scheme for measuring layer-resolved properties is outlined in Sec. 3.7. Chapter 4 discusses global properties for our films, including a successful time-temperature superposition (TTS) for all our films. This enables us to estimate the shear viscosities $\eta$ and gives a relative scale for the terminal $\alpha$-relaxation time $\tau_\alpha$. Chapter 5 focuses on the storage and loss moduli $G'(\omega)$ and $G''(\omega)$ and the creep compliance $J(t)$ for *film1*. The latter property is compared to experimental results reported in Ref. [19]. Using the complex modulus at high temperatures we shall obtain an absolute scale for the terminal relaxation time (Sec. 5.3). Chapter 6 describes a *layer-resolved* analysis method to calculate the local shear modulus $\mu(z)$ for *film1*, which will help us understand the local *linear-additive* contributions to global properties and the $H$-dependence of the films. Chapter 7 extends the work on shear stress fluctuations and describes systematically the standard deviation of the variance of shear stresses by assuming a stationary Gaussian process. We conclude and present future perspectives in Ch. 8. Appendices A, B, C and D appearing at the end of the manuscript bring together relevant supporting elements of this thesis. Appendix A gives further details on ergodic Gaussian processes (Secs. A.1-A.3) and

non-ergodic stochastic processes (Secs. A.4-A.7). Appendix B reminds the definitions of the instantaneous shear stress $\hat{\tau}$ and the instantaneous affine shear modulus $\hat{\mu}_{\mathrm{A}}$ (Sec. B.1) and gives a demonstration of the stress-fluctuation formula Eq. 1.1 (Sec. B.2). Viscoelastic properties of the discrete Rouse model for polymer chains are reminded in Appendix C. The numerical transformations between various rheological linear response functions are described in Appendix D.

# Chapter 2

# General theoretical considerations

## 2.1 Introduction

In this chapter, we will introduce general theoretical concepts (Sec. 2.2 to Sec. 2.7) that are useful for the analysis of the time-series of stationary Gaussian processes. In Sec. 2.8, we will translate these concepts and notations into specific forms useful for the characterization of shear-stress fluctuations in liquids and amorphous solids. Most of these developments are adapted from our accepted article in Ref. [69]. Based on the recent work carried out in our group focusing on stress fluctuations [63, 65–68, 77, 95, 98–102, 104] we give here a systematic and uncluttered overview of three general points of relevance for a large variety of problems in condensed matter [1, 3, 4, 6, 105–107], material modeling [108, 109] and in computational physics [57, 110].

Let us consider a general stochastic dynamical variable $x(t)$. Ensembles of discrete time series $\mathbf{x} = \{x_i = x(t_i), i = 1, \ldots, I\}$ are sampled with the data sequence taken at equally spaced times $t_i = i\delta t$ from $t_1 = \delta t$ up to the "sampling time" $\Delta t = t_I = I\delta t$. We focus on the *empirical variance* [111]

$$v[\mathbf{x}] \equiv \frac{1}{I} \sum_{i=1}^{I} x_i^2 - \frac{1}{I^2} \left[ \sum_{i,j=1}^{I} x_i x_j \right]^2 \tag{2.1}$$

and its ensemble average $v = \langle v[\mathbf{x}] \rangle$ and standard deviation $\delta v$.[2] We assume that $x(t)$ is a *stationary* stochastic process respecting the time-translational invariance [112]. Our *first*

---

[2]The empirical variance is defined here without the usual "Bessel correction" [111]. Eq. 2.1 is the formal definition of $v[\mathbf{x}]$ which coincides with the genuine variance of $x(t)$ only in the limit $\Delta t \propto I \to \infty$.

point is that the expectation value $v$ for sampling times $\Delta t$ smaller than the terminal relaxation time $\tau_\alpha$ is not necessarily constant. As demonstrated in Sec. 2.3 this is a consequence of the "stationarity relation" [65, 67, 68, 77, 99, 101, 113]

$$v = \frac{2}{I^2} \sum_{i=1}^{I-1} (I - i) \, h_i \;\; \text{with} \;\; h_{i-j} = \frac{1}{2} \left\langle (x_i - x_j)^2 \right\rangle \tag{2.2}$$

being the autocorrelation function (ACF) characterizing the mean-square displacements (MSDs) of the data entries $x_i$. Hence, $v$ generally depends on $I$ or $\Delta t$ and this is especially relevant if the ACF $h_i = h(t_i)$ increases strongly for $t \approx \Delta t$.

Our *second* point concerns the standard deviation $\delta v$ of $v[\mathbf{x}]$. It has been observed for shear-stress fluctuations [65, 67, 68, 77, 101] that $\delta v$ may become rather large and of the order of the mean value $v$ if $h(t)$ varies strongly for $t \approx \Delta t$, i.e. the mean behavior standard experimental or theoretical work focuses on [1, 3, 4, 106, 108] gets *masked* by strong fluctuations. As derived in Sec. 2.5.3, this can be simply understood assuming a stationary *Gaussian* stochastic process [77] showing that $\delta v = \delta v_{\mathrm{G}}[h]$ with $\delta v_{\mathrm{G}}[h]$ being a functional of the MSD $h$ defined by

$$\delta v_{\mathrm{G}}^2[h] \equiv \frac{1}{2I^4} \sum_{i,j,k,l=1}^{I} g_{ijkl}^2 \;\; \text{and} \;\; g_{ijkl} \equiv (h_{i-j} + h_{k-l}) - (h_{i-l} + h_{j-k}). \tag{2.3}$$

We discuss numerically more convenient representations of Eq. 2.3 in Appendix A.1. By analyzing the functional $\delta v_{\mathrm{G}}[h]$ it will be seen (Appendix A.2 and Appendix A.3) that while $\delta v(\Delta t)$ must remain small for $h(t \approx \Delta t) \approx$ constant, $\delta v(\Delta t)$ becomes generally large if $\Delta t$ is similar to the characteristic time of an efficient relaxation pathway corresponding to a strong change of $h(t)$ for $t \approx \Delta t$.

Our *third* key point emphasizes one limitation of Eq. 2.3 which hinges on the ergodicity of the stochastic process. If the system is (strictly or in practice) non-ergodic, i.e. if independently created trajectories $c$ are restricted to different meta-basins of the generalized phase space, this implies as shown in Sec. 2.6 and Appendix A.5 that

$$\delta v(\Delta t) \to \Delta_{\mathrm{ne}} = \text{constant for } \tau_\alpha \gg \Delta t \gg \tau_{\mathrm{ne}} \gg \tau_{\mathrm{b}}. \tag{2.4}$$

$\tau_{\mathrm{b}}$ denotes here the typical relaxation time of the meta-basins, $\tau_{\mathrm{ne}}$ a crossover time properly

defined in Sec. 2.6 and Appendix A.6 and $\Delta_{\mathrm{ne}}$ the static standard deviation of the quenched variances $v_c$ of the configurations $c$. Equation 2.4 implies that in this limit $\delta v(\Delta t)$ must differ from $\delta v_{\mathrm{G}}(\Delta t) \propto 1/\sqrt{\Delta t}$. Fortunately, in the common case where the observables $x(t)$ average over many, more or less decoupled microstates, $\delta v \to \delta v_{\mathrm{G}}[h]$ even for non-ergodic systems in the macroscopic limit as argued in Sec. 2.7. Simple test functions $f(t)$ are used to demonstrate $\delta v_{\mathrm{G}}[f]$ in Appendix A.3. The definitions of the instantaneous shear stress and the corresponding Born-Lamé coefficient are given in Appendix B.1.

## 2.2 Different types of averages considered

Various functionals $\mathcal{O}[\mathbf{x}]$ of $\mathbf{x}$ can be computed, for instance the moments

$$m_{\alpha\beta}[\mathbf{x}] \equiv \left( \frac{1}{I} \sum_{i=1}^{I} x_i^{\alpha} \right)^{\beta} \tag{2.5}$$

with $\alpha = 1, 2, 3, 4$ and $\beta = 1, 2$. The empirical variance of the time series $\mathbf{x}$ is then given by $v[\mathbf{x}] = m_{21}[\mathbf{x}] - m_{12}[\mathbf{x}]$. Obviously, $v[\mathbf{x}] = 0$ for $I = 1$. Functionals with a discrete time lag $s$ (with $s = 0, \ldots, I-1$) can be considered such as the *"gliding average"* [57]

$$c_s^{\mathrm{g}}[\mathbf{x}] \equiv \frac{1}{I-s} \sum_{i=1}^{I-s} c_{s,i} \text{ with } c_{s,i} = x_{i+s} x_i \tag{2.6}$$

and similarly

$$h_s^{\mathrm{g}}[\mathbf{x}] \equiv \frac{1}{I-s} \sum_{i=1}^{I-s} h_{s,i} \text{ with } h_{s,i} = \frac{1}{2} \left( x_{i+s} - x_i \right)^2 = \frac{x_i^2 + x_{i+s}^2}{2} - c_{s,i}. \tag{2.7}$$

Note that $c_0^{\mathrm{g}}[\mathbf{x}] = m_{21}[\mathbf{x}]$ and $h_0^{\mathrm{g}}[\mathbf{x}] = 0$. Averages over a given time series are often called here *"t-averages"*. Since the functionals $\mathcal{O}[\mathbf{x}]$ are obtained in general from *correlated* data entries, ensemble averages $\langle \ldots \rangle$ of fluctuation-type functionals may depend on the sampling time $\Delta t$. This is not the case for *"simple averages"* [57, 100, 101] for which the ensemble average over independent trajectories and the $t$-average *commute*. For instance, we have

$$m_{\alpha 1} \equiv \langle m_{\alpha 1}[\mathbf{x}] \rangle = \left\langle \frac{1}{I} \sum_{i=1}^{I} x_i^{\alpha} \right\rangle = \frac{1}{I} \sum_{i=1}^{I} \langle x_i^{\alpha} \rangle \propto \Delta t^0 \tag{2.8}$$

since the ensemble average $\langle x_i^\alpha \rangle$ is $\Delta t$-independent. Interestingly, the commutation of both averaging-operators is not possible for $m_{\alpha\beta}$ with $\beta \neq 1$. An argument $\Delta t$ often marks in this thesis a property being *not* a simple average.

## 2.3   Stationarity

We suppose that the time series is taken from a *stationary* stochastic process whose unconditional joint probability distribution does not change when shifted in time [112]. Correlation functions such as $\langle x_i x_j \rangle$ thus only depend on the difference $s = |i - j|$ of the discrete indices $i$ and $j$. We thus define

$$c_s = \langle c_s^{\mathrm{g}}[\mathbf{x}] \rangle \ \text{ and } \ h_s = c_0 - c_s = \langle h_s^{\mathrm{g}}[\mathbf{x}] \rangle \tag{2.9}$$

with $0 \leq s < I$ in terms of the gliding averages $c_s^{\mathrm{g}}[\mathbf{x}]$ and $h_s^{\mathrm{g}}[\mathbf{x}]$ defined in Sec. 2.2. Note that both $c_s$ and $h_s$ are simple averages, i.e. their expectation values do not depend on the sampling time $\Delta t$ of the time series [101, 113]. Due to the assumed stationarity, the variance $v = \langle v[\mathbf{x}] \rangle$ becomes [57, 65–68, 77, 99, 101, 110, 113]

$$\begin{aligned} v(I) &= \frac{1}{I} \sum_{i=1}^{I} \langle x_i^2 \rangle - \left( \frac{1}{I^2} \sum_{i=1}^{I} \langle x_i^2 \rangle + \frac{2}{I^2} \sum_{k=1}^{I-1} (I - k) \langle x_{k+1} x_1 \rangle \right) \\ &= c_0 \, (1 - I^{-1}) - \frac{2}{I^2} \sum_{k=1}^{I-1} (I - k) c_k = \frac{2}{I^2} \sum_{i=1}^{I-1} (I - i) \, h_i \end{aligned} \tag{2.10}$$

which demonstrates the stated Eq. 2.2. In the last step we used $h_s = c_0 - c_s$ and

$$\frac{2}{I^2} \sum_{k=1}^{I-1} (I - k) = 1 - 1/I. \tag{2.11}$$

Albeit the mentioned $\Delta t$-dependence is well known [57, 110] it is emphasized here for systematic reasons and since $\Delta t$-effects for such fluctuations are rarely checked [63, 95]. We also remind that in the continuum limit for large $I = \Delta t/\delta t$, Eq. 2.10 reads

$$v(\Delta t) = \frac{2}{\Delta t^2} \int_0^{\Delta t} \mathrm{d}t \, (\Delta t - t) \, h(t) \tag{2.12}$$

with $h(t)$ being the continuum limit of $h_s$. This result may be restated equivalently using the inverse relation $h(t) = [v(t)t^2/2]''$ with a prime denoting a derivative with respect to time [65, 77]. Using that $m_{21}$ is a simple average Eq. 2.12 implies that

$$m_{12}(\Delta t) = m_{21} - \frac{2}{\Delta t^2} \int_0^{\Delta t} dt \, (\Delta t - t) \, h(t). \tag{2.13}$$

The ensemble averages $v(\Delta t)$ and $m_{12}(\Delta t)$ thus depend in general on the sampling time $\Delta t$. However, the $\Delta t$-dependence disappears, if $h(t)$ becomes constant. For instance, this is the case, if $h(t)$ plateaus in an intermediate, sufficiently large, time window, i.e. $h(t) \approx h_p = c(0) - c_p$ with $h_p$ and $c_p$ being constants. We then have

$$v(\Delta t) \approx h_p = c(0) - c_p = \text{constant},$$
$$m_{12}(\Delta t) \approx m_{21} - h_p = c_p = \text{constant}. \tag{2.14}$$

Equation 2.14 also holds, if $c(t)$ tends to a constant for times much longer than the terminal relaxation time $\tau_\alpha$ of the system. Then, $c_p$ in Eq. 2.14 is replaced by the long-time limit $c_\infty = \lim_{t \to \infty} c(t) = \lim_{\Delta t \to \infty} m_{12}(\Delta t)$.

## 2.4 Linear response

### 2.4.1 Linear response function $R(t)$

The functions $h(t)$ and $c(t)$ can be related to the linear response to an external perturbation conjugate to $x(t)$. Let $R(t)$ denote the linear response function of the system to a weak external perturbation that is instantaneously switched on at $t = 0$ and held constant for $t > 0$. By virtue of the fluctuation-dissipation theorem one can show that [3, 99, 101, 105]

$$R(t) = R_A - h(t) = (R_A - c(0)) + c(t) \tag{2.15}$$

with $R_A = R(0)$ being a constant characterizing the initial response of the system after the external perturbation is applied.[3] For elastic properties, this constant is given by a Born-Lamé affine modulus (Appendix B.1). $R(t)$ is a simple average just as $h(t)$ and $c(t)$.

---

[3]Equation (2.15) holds if the perturbation is a "deformation" (thermodynamical extensive variable). In the case of an externally applied "force" (thermodynamical intensive variable) it becomes $R(t) = h(t)$ [3].

### 2.4.2 Generalized dynamical modulus $M(\Delta t)$

It is of importance that Eq. 2.12 can be rewritten in terms of $R(t)$ as

$$M(\Delta t) \equiv R_A - v(\Delta t) = \frac{2}{\Delta t^2} \int_0^{\Delta t} dt \ (\Delta t - t) R(t) \tag{2.16}$$

with $M(\Delta t)$ being the *generalized dynamical modulus* [101]. The corresponding equation for the (generalized) shear modulus $M = \mu$ and the shear relaxation function $R(t) = G(t)$ was highlighted in the Introduction, Eq. 1.2. Although the generalized modulus does in general depend on $\Delta t$, it becomes constant

$$M(\Delta t) \to R_\infty \equiv R_A - c(0) + c_\infty \text{ for } \Delta t/\tau_\alpha \to \infty. \tag{2.17}$$

The corresponding stress-fluctuation formula for the shear modulus, Eq. B.7, is derived in Appendix B.2. Being a second integral over $R(t) = [M(t)t^2/2]''$, $M(\Delta t)$ is a natural smoothing function statistically better behaved than $R(t)$ and containing in general information about both the reversibly stored energy and the dissipation processes.

### 2.4.3 Green-Kubo and Einstein relations

In statistical mechanics Eq. 2.10 and Eq. 2.16 are closely related to the equivalence of the Green-Kubo and the Einstein relations for transport coefficients [57, 65, 68, 105, 110]. This is seen by rewriting Eq. 2.16 as

$$\eta(t) \equiv \int_0^t ds \ (R(s) - R_\infty) = \frac{d}{dt} [(M(t) - R_\infty) \ t^2/2]. \tag{2.18}$$

If the integral $\eta(t)$ converges to a constant $\eta$ for $t \gg \tau_\alpha$, this implies the Einstein relation

$$(M(t) - R_\infty)t^2 \to 2\eta t \text{ for } t \gg \tau_\alpha. \tag{2.19}$$

We denote $\eta$ without an argument for the $t$-independent long time limit of $\eta(t)$. Since the statistics quite generally deteriorates for large $t$, it is for numerical reasons useful to trace and analyze $\eta(t)$ or $(M(t) - R_\infty)t$ for the determination of $\eta$. This is shown in Sec. 5.2 for the Green-Kubo relation. The Einstein relation Eq. 2.19 will be applied in Sec. 4.8 for the

diffusion constant $D$ and in Sec. 4.5 for the shear viscosity $\eta$. Since $M(t)$ is an integral over $R(t)$, the Einstein relation is generally numerically better behaved than the Green-Kubo relation, however, on the downside it also converges more slowly to $\eta$ [57].

### 2.4.4 Reciprocal space properties

Since we characterize a stationary process it is natural to describe the linear response function $R(t)$ in reciprocal frequency ($\omega$) space. Importantly, the components of the Fourier transform $R^\star(\omega) = R'(\omega) + iR''(\omega)$ of $R(t)$ may directly be measured in an oscillatory experiment varying the associated extensive variable (strain). These components are quite generally given by [1, 4, 6]

$$R'(\omega) - R_\infty = \int_0^\infty d(\omega t) \, \cos(\omega t) \, (R(t) - R_\infty) \quad \text{and} \tag{2.20}$$

$$R''(\omega) = \int_0^\infty d(\omega t) \, \sin(\omega t) \, (R(t) - R_\infty). \tag{2.21}$$

For (visco)elastic response functions $R'(\omega)$ is called the "storage modulus" and $R''(\omega)$ the "loss modulus". We shall use these definitions in Ch. 5, Appendix C and Appendix D. Note for later convenience that $R'(\omega)$ becomes constant, $R'(\omega) \to R_A$, in the high-$\omega$ limit while $R''(\omega)$ must vanish inversely with $\omega$ [104].[4] Quite generally, $R'(\omega) \propto \omega^2$ and $R''(\omega) \propto \omega$ in the low-$\omega$ limit, i.e. for $\omega$ smaller than the inverse of the largest relaxation time $\tau_\alpha$. Using standard notations [1] we write

$$R'(\omega)/\omega^2 \to J_e^0 \eta^2 \text{ and } R''(\omega)/\omega \to \eta \text{ for } \omega\tau_\alpha \to 0 \tag{2.22}$$

with $\eta$ being the transport coefficient already seen in Eq. 2.18 and $J_e^0$ the "steady-state creep compliance".

### 2.4.5 Terminal relaxation time $\tau_\alpha$

We have used above the "terminal relaxation time" $\tau_\alpha$ of the stochastic process without giving an operational definition. Various definitions are stated in the literature [105, 106], especially in the standard textbooks on rheology and complex fluids [1, 4, 6]. While all these definitions are equivalent from the scaling point view [2], they may not be equally

---

[4]For elastic or viscoelastic properties $R_A$ is thus often called "high frequency modulus".

useful in experimental or computational studies. Several of these definitions consider ratios of the moments $m_k \equiv \int_0^\infty \mathrm{d}t\, t^k\, (R(t) - R_\infty)$, e.g.,

$$\tau_{\alpha,0} \equiv \frac{m_0}{R_A} = \frac{\eta}{R_A}, \quad \tau_{\alpha,1} \equiv \frac{m_1}{m_0} = J_e^0 \eta \quad \text{or} \quad \tau_{\alpha,2} \equiv \frac{m_2}{m_1} = \frac{m_2}{J_e^0 \eta^2} \tag{2.23}$$

where we have used that $\eta = m_0$ and $J_e^0 = m_1/\eta^2$. One problem of these definitions is that the long-time limit $R_\infty$ must be known to high precision.[5] Even more importantly, in numerical studies the statistics for $R(t)$ strongly deteriorates for large $t$. The numerically most convenient definition $\tau_{\alpha,0}$ unfortunately uses $R_A = R(t=0)$ which is experimentally often not available and, moreover, corresponds to microscopic physics which has little to do with the long-time relaxation processes one wishes to characterize.[6] The determination of moments $m_k$ with $k > 1$ becomes quite generally very demanding and is in practice often impossible. We thus focus below on $\tau_{\alpha,1} = J_e^0 \eta$. Interestingly, the low-$\omega$ asymptotes of $R'(\omega)$ and $R''(\omega)$, Eq. 2.22, cross at $\omega = 1/\tau_{\alpha,1}$. This suggests to characterize both in experiments as in numerical studies the terminal relaxation time by [1, 6]

$$\tau_\times(\lambda) \equiv 1/\omega_\times(\lambda) \quad \text{with } \lambda \equiv \tan(\delta) = \frac{R''(\omega_\times)}{R'(\omega_\times)} \quad \text{with } \lambda \approx 1 \tag{2.24}$$

using the (first) crossing of $\lambda R'(\omega)$ and $R''(\omega)$. Due to the generic flattening of both $R'(\omega)$ and $R''(\omega)$ for frequencies around the terminal relaxation time, it is normally best to chose a value slightly above unity, e.g., $\lambda = 2$, to obtain one characterization of the *terminal relaxation time*.[7] This is illustrated in Appendix C for the Rouse model. We compare $\tau_{\alpha,1} = m_1/m_0$ and $\tau_\times$ in Ch. 5 for our numerical film data and in Appendix C for the Rouse model.[8]

---

[5]Fortunately, $R_\infty \equiv 0$ by symmetry for the shear-stress relaxation function $R(t) = G(t)$ this thesis focuses on.

[6]$R_A$ is thus often replaced by an intermediate plateau value of $R(t)$.

[7]For too low $\lambda$-values $\tau_\times(\lambda) \ll \tau_\alpha$ characterizes local relaxation processes.

[8]We note for completeness that very often $\tau_\alpha$ is also estimated roughly as the time where $R(t) - R_\infty$ has decayed to a given fraction of the signal at short times. This is used in Ref. [70] for the computation of the basin relaxation time $\tau_b$ for non-ergodic stochastic processes.
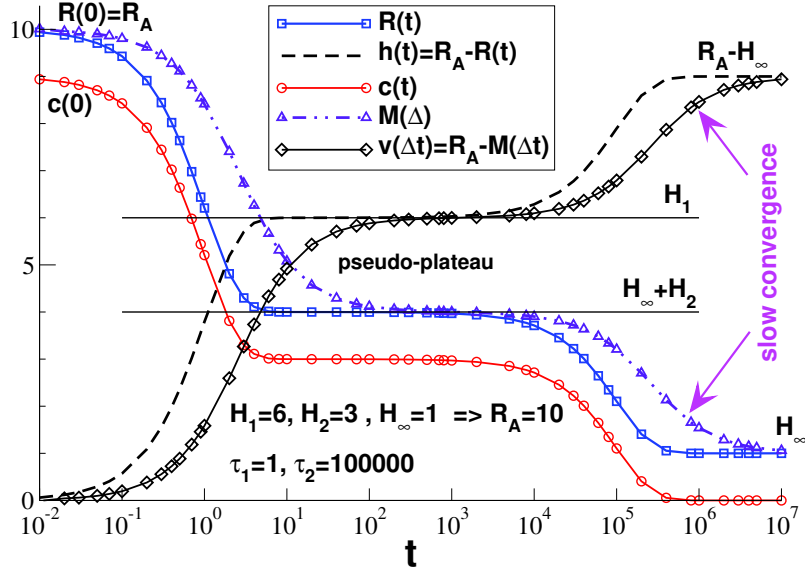
Figure 2-1: Illustration of properties discussed in Sec. 2.4.1 using a two-modes version of Eq. 2.25 with amplitudes $R_\infty = 1$, $H_1 = 6$, $H_2 = 3$, i.e. $R(0) = R_A = R_\infty + H_1 + H_2 = 10$, and relaxation times $\tau_1 = 1$ and $\tau_2 = 100000$. $h(t)$ and $c(t)$ are given by Eq. 2.15, where we have additionally set $c_\infty = 0$, and $M(\Delta t)$ and $v(\Delta t)$ by means of Eqs. 2.16 and 2.28. The two solid horizontal lines mark the intermediate pseudo-plateau for $\tau_1 \ll t \ll \tau_2$. $v(\Delta t)$ and $M(\Delta t)$ are seen to converge much slower to the respective plateau values than the corresponding response functions $h(t)$ and $R(t)$.

## 2.4.6 Generalized Maxwell model

Response functions are often fitted using the generalized Maxwell model[9]

$$R(t) = R_\infty + \sum_{p=1}^{p_{\max}} H_p \exp(-t/\tau_p) \tag{2.25}$$

with $H_p$ and $\tau_p$ being, respectively, the amplitude and the relaxation time of the mode $p$ [1, 4, 6]. Note that $R(0) = R_\infty + \sum_{p=1}^{p_{\max}} H_p$ and $\lim_{t\to\infty} R(t) = R_\infty$. Commonly, one considers logarithmic time scales for $R(u)$ with $u \propto \log(t)$ and the modes are distributed logarithmically in time [1]. As summarized in Appendix C, an important example of a generalized Maxwell model is given by the Rouse model for the polymer dynamics of un-entangled and non-interacting chains in the melt [1, 3–6]. Being of relevance for Ch. 5 and

---

[9] Equation 2.25 will be used in Sec. 5.3 and Appendix D to decompose $R(t) = G(t)$ into modes.

Appendix D we also remind that [1, 6]

$$R'(\omega) = \sum_{p=1}^{p_{\max}} H_p \frac{(\tau_p \omega)^2}{1 + (\tau_p \omega)^2} \text{ and } R''(\omega) = \sum_{p=1}^{p_{\max}} H_p \frac{\tau_p \omega}{1 + (\tau_p \omega)^2}. \quad (2.26)$$

Using the notations of Eq. 2.22 we obtain [1]

$$\eta = \sum_{p=1}^{p_{\max}} H_p \tau_p \text{ and } J_{\mathrm{e}}^0 = \sum_{p=1}^{p_{\max}} H_p \tau_p^2 / \eta^2 \quad (2.27)$$

which in turn determines the terminal relaxation time $\tau_{\alpha,1} = J_{\mathrm{e}}^0 \eta$. Coming back to Eq. 2.16 the generalized modulus can be rewritten as [101]

$$M(\Delta t) = R_\infty + \sum_{p=1}^{p_{\max}} H_p \ g_{\mathrm{Debye}}(\Delta t / \tau_p) \text{ with } g_{\mathrm{Debye}}(x) = \frac{2}{x^2} \left[ \exp(-x) - 1 + x \right] \quad (2.28)$$

being the "Debye function" well known in polymer science [3, 6]. Fig. 2-1 presents both $R(t)$ and $M(\Delta t)$ for a generalized Maxwell model with two modes with $\tau_1 \ll \tau_2$. The upper solid horizontal line indicates an intermediate pseudo-plateau, Eq. 2.14. Note also that $h(t) \approx v(\Delta t) \approx R_A - R_\infty$ for $t \approx \Delta t \gg \tau_2$. Since $v(\Delta t)$ and $M(\Delta t)$ are second integrals over $h(t)$ and $R(t)$, they converge much slower to the respective intermediate or terminal plateau values. ($h(t)$ being a monotonically increasing function implies $h(t) > v(t)$ and $R(t) < M(t)$.) As shown by Fig. 2-1, the determination of a plateau value by means of Eq. 2.12 or Eq. 2.16 may thus be tedious [63, 99, 101].

## 2.5 Gaussian stochastic processes

### 2.5.1 Gaussian variables

Let us consider a Gaussian variable $y$ of variance $\sigma^2$. Since $\langle (y - \langle y \rangle)^4 \rangle = 3\sigma^4$ we have

$$\langle z^2 \rangle - \langle z \rangle^2 = 2\sigma^4 \text{ for } z = (y - \langle y \rangle)^2, \quad (2.29)$$

i.e. the variance of the variance $z$ of $y$ is twice the squared variance of $y$. We assume now that the time series $\mathbf{x}$ is a Gaussian process [112]. (The main physical reason why this assumption holds for many systems is discussed in Sec. 2.7.) The mean $m_{11}[\mathbf{x}]$ is thus a

Gaussian variable and Eq. 2.29 holds for $y = m_{11}[\mathbf{x}]$. Assuming that $\langle y \rangle = m_{11} = 0$ by symmetry or by shifting of the data and using that $m_{\alpha 1}[\mathbf{x}]^\beta = m_{\alpha \beta}[\mathbf{x}]$ this implies [77]

$$\delta m_{12}^2 = m_{14} - m_{12}^2 = 2(\delta m_{11}^2)^2 = 2m_{12}^2, \qquad (2.30)$$

i.e. the variance $\delta m_{12}^2(\Delta t)$ is given by $m_{12}(\Delta t)$.

## 2.5.2 $\delta h^2$ for Gaussian processes

Let us next discuss the typical fluctuations of the ACFs $c_s$ and $h_s$ defined in Sec. 2.3. There are *two* meaningful ways to define the variances. One may characterize the fluctuations of $c_s^{\mathrm{g}}[\mathbf{x}]$ and $h_s^{\mathrm{g}}[\mathbf{x}]$ by

$$\delta c_s^{\mathrm{g}2} = \left\langle c_s^{\mathrm{g}}[\mathbf{x}]^2 \right\rangle - \left\langle c_s^{\mathrm{g}}[\mathbf{x}] \right\rangle^2 \text{ and } \delta h_s^{\mathrm{g}2} = \left\langle h_s^{\mathrm{g}}[\mathbf{x}]^2 \right\rangle - \left\langle h_s^{\mathrm{g}}[\mathbf{x}] \right\rangle^2. \qquad (2.31)$$

This allows to get the variances and the error bars for the numerical most accurate way to compute $c_s$ and $h_s$. The trouble with this definition is that, since the gliding averages are preformed first and since the data entries $x_i$ are correlated in time, Eq. 2.31 depends on these correlations in an intricate way.[10] This may mask the fact that the data have a Gaussian distribution. A second way to characterize the fluctuations is to measure in a first step $c_{s,i}$ and $h_{s,i}$ (Sec. 2.2), to take then the ensemble averages

$$\delta c_{s,i}^2 = \left\langle c_{s,i}^2 \right\rangle - \left\langle c_{s,i} \right\rangle^2 \text{ and } \delta h_{s,i}^2 = \left\langle h_{s,i}^2 \right\rangle - \left\langle h_{s,i} \right\rangle^2 \qquad (2.32)$$

and only as the last step (last loop) to take the arithmetic average over all $I - s$ possible indices $i$

$$\delta c_s^2 = \frac{1}{I-s} \sum_{i=1}^{I-s} \delta c_{s,i}^2, \ \delta h_s^2 = \frac{1}{I-s} \sum_{i=1}^{I-s} \delta h_{s,i}^2. \qquad (2.33)$$

Assuming $\mathbf{x}$ to be Gaussian, $y = (x_{i+s} - x_i)/\sqrt{2}$ is a Gaussian variable of zero mean. According to Eq. 2.29 this implies the important relation

$$\delta h_s^2 = \left\langle y^4 \right\rangle - \left\langle y^2 \right\rangle^2 = 2 \left\langle y^2 \right\rangle^2 = 2h_s^2. \qquad (2.34)$$

---

[10]The variances increase with $s$ since the number of data entries decreases linearly with $s$.

In a similar way we find: $\delta c_s^2 = c_0^2 + c_s^2$. We shall put Eq. 2.34 to the test in Sec. 7.3 for our polymer films. For the fluctuations of $R_s = R_A - h_s$ with $R_A$ being constant Eq. 2.34 yields in turn $\delta R_s^2 = 2h_s^2$. The latter relation may even hold if $R_A$ is not strictly constant. This is relevant for the fluctuations of the shear-stress relaxation function $G(t)$ and the shear modulus $\mu(\Delta t)$ considered in Ch. 7.

### 2.5.3   $\delta v_G$ for Gaussian processes

We turn now to the derivation of Eq. 2.3 for the variance $\delta v^2 \equiv \langle v[\mathbf{x}]^2 \rangle - \langle v[\mathbf{x}] \rangle^2$. Using Eq. 2.1 this may be written as

$$\delta v^2 = T_2 + T_4 - T_3 \text{ with} \tag{2.35}$$

$$T_2 \equiv \delta m_{21}^2 = \langle m_{21}[\mathbf{x}]^2 \rangle - \langle m_{21}[\mathbf{x}] \rangle^2 = \frac{1}{I^2} \sum_{ij} \langle x_i^2 x_j^2 \rangle - \frac{1}{I^2} \sum_{ij} \langle x_i^2 \rangle \langle x_j^2 \rangle$$

$$T_4 \equiv \delta m_{12}^2 = \langle m_{12}[\mathbf{x}]^2 \rangle - \langle m_{12}[\mathbf{x}] \rangle^2 = \frac{1}{I^4} \sum_{ijkl} \langle x_i x_j x_k x_l \rangle - \frac{1}{I^4} \sum_{ijkl} \langle x_i x_j \rangle \langle x_k x_l \rangle$$

$$T_3 \equiv 2 \operatorname{cov}(m_{21}, m_{12}) \equiv 2 \left( \langle m_{21}[\mathbf{x}] m_{12}[\mathbf{x}] \rangle - \langle m_{21}[\mathbf{x}] \rangle \langle m_{12}[\mathbf{x}] \rangle \right)$$

$$= \frac{2}{I^3} \sum_{ikl} \langle x_i^2 x_k x_l \rangle - \frac{2}{I^3} \sum_{kl} \langle x_i^2 \rangle \langle x_k x_l \rangle$$

where the sums run over all $I$ data entries. As we have assumed that the stochastic process is stationary and Gaussian, Wick's theorem must hold [3, 112]:

$$\langle x_i x_j x_k x_l \rangle = \langle x_i x_j \rangle \langle x_k x_l \rangle + \langle x_i x_k \rangle \langle x_j x_l \rangle + \langle x_i x_l \rangle \langle x_j x_k \rangle . \tag{2.36}$$

Setting in addition $c_{i-j} = \langle x_i x_j \rangle$ the three terms in Eq. 2.35 can be rewritten as

$$T_2(\Delta t) = \frac{2}{I^2} \sum_{ij} \langle x_i x_j \rangle^2 = \frac{2}{I^2} \sum_{ij} c_{i-j}^2 \tag{2.37}$$

$$T_4(\Delta t) = \frac{2}{I^4} \left( \sum_{ij} \langle x_i x_j \rangle \right)^2 = \frac{2}{I^4} \left( \sum_{ij} c_{i-j} \right)^2 \tag{2.38}$$

$$T_3(\Delta t) = \frac{4}{I^3} \sum_s \sum_i \langle x_i x_s \rangle \sum_j \langle x_j x_s \rangle = \frac{4}{I^3} \sum_{s,i,j} c_{i-s} c_{j-s}. \tag{2.39}$$

22

Note that $T_4 = \delta m_{12}^2 = 2m_{12}^2$ in agreement with Eq. 2.30. Importantly, Eqs. 2.35, 2.37, 2.38, 2.39 are equivalent to the more compact formula [77],

$$\delta v_{\rm G}^2 = \frac{1}{2I^4} \sum_{i,j,k,l} g_{ijkl}^2 \text{ with } g_{ijkl} = (c_{i-j} + c_{k-l}) - (c_{i-l} + c_{j-k}) \qquad (2.40)$$

which looks already rather similar as Eq. 2.3. That this holds can be verified by straight-forward expansion of Eq. 2.40. Note that the squared terms $c_{i-j}^2 + \ldots$ with two different indices contribute to $T_2$, the terms $c_{i-j}c_{k-l} + \ldots$ with four different indices to $T_4$ and the terms $c_{i-j}c_{i-l} + \ldots$ with three different indices to $T_3$. (Numerically convenient reformulations of $T_2$, $T_3$, and $T_4$ are given in Appendix A.1.) With $a$ and $b$ being real constants it follows directly from Eq. 2.40 that

$$\delta v_{\rm G}[a] = 0 \text{ and } \delta v_{\rm G}[b(f - a)] = |b| \ \delta v_{\rm G}[f] \qquad (2.41)$$

for any function $f(t)$. Specifically, $\delta v_{\rm G}[c] = \delta v_{\rm G}[h]$. This demonstrates finally that Eq. 2.3 is equivalent to Eq. 2.40 and, hence, to Eqs. 2.35, 2.37, 2.38, 2.39. It may also be useful to replace $c(t)$ by $c(t) - c_\infty$ or — for thermodynamic equilibrium systems — by the linear response function $R(t)$, Eq. 2.15. See Appendix A.2 for some general properties of $\delta v_G[f]$ and Appendix A.3 for the behavior of $\delta v_G[f]$ for various test functions $f(t)$.

## 2.6   Non-ergodic stochastic processes

Our key relation Eq. 2.3 and its various reformulations may obviously fail if one of the stated or implicit assumptions does not apply for the particular ensemble of time series. For instance, strong non-Gaussian contributions may be present in a specific time or frequency range leading to the failure of Wick's theorem, Eq. 2.36. We will address here an important assumption not yet explicitly stated. In fact it was assumed that the stochastic process under consideration is *ergodic*, i.e. all independently created trajectories, called here *configurations*, are able to explore given enough time the complete (generalized) phase space. The averages which appear in Wick's theorem, Eq. 2.36, can thus be either obtained by averaging over independent configurations $c$ or by averaging over subsets of one extremely long trajectory. To see that this condition matters let us consider a strictly non-ergodic

23

system where the configurations $c$ are trapped in subspaces of the total phase space (since the terminal relaxation time $\tau_\alpha$ of the system diverges). If $t$ and $\Delta t$ exceed the typical relaxation time $\tau_b$ of these basins, $h(t)$ and $v(\Delta t)$ must become constant. As shown in Appendix A.5 and Appendix A.6, $\delta v_G \propto 1/\sqrt{\Delta t}$ for $\Delta t \gg \tau_b$. At variance to this $\delta v \to \Delta_{ne}$ becomes constant with,

$$\Delta_{ne}^2 \equiv \text{var}(v_c) = \frac{1}{N_c} \sum_{c=1}^{N_c} v_c^2 - \left( \frac{1}{N_c} \sum_{c=1}^{N_c} v_c \right)^2 \tag{2.42}$$

being the variance of the $N_c$ quenched variances $v_c = \lim_{\Delta t \to \infty} v[\mathbf{x}_c]$ of the independent configurations. Obviously, $\Delta_{ne}$ vanishes for identical $v_c$. This holds indeed for ergodic systems for $\Delta t \gg \tau_\alpha$ with the finite terminal relaxation time $\tau_\alpha$ replacing $\tau_b$, but in general not for non-ergodic systems. On the other side, for small $\Delta t$ the non-ergodicity constraint should not matter much and one expects $\delta v \approx \delta v_G$ to approximately hold. Interpolating between both $\Delta t$-limits a useful approximation for non-ergodic systems may be written as,

$$\delta v^2(\Delta t) \approx \delta v_G^2(\Delta t) + \Delta_{ne}^2 \text{ for } \tau_b \ll \Delta t \ll \tau \tag{2.43}$$

motivated by the idea that $\delta v^2$ is the sum of two variances describing the independent fluctuations within each configuration and between the different configurations. Moreover, Eq. 2.43 suggests the operational definition,

$$\delta v_G(\Delta t \stackrel{!}{=} \tau_{ne}) = \Delta_{ne} \tag{2.44}$$

identifying $\tau_{ne}$ as the crossover time between both limits. Quite generally, $\tau_{ne} \gg \tau_b$ holds. As shown in the Appendix A.6, to understand the discrepancy between $\delta v$ and $\delta v_G$ for (strictly) non-ergodic systems it is necessary to introduce an extended ensemble of time series $\mathbf{x}_{ck}$ where for each of the $N_c$ independent configurations $c$ one samples $N_k$ time series $k$. Obviously, the time series $k$ of the same configuration $c$ are correlated (being all confined into the same basin) and $k$-averaged expectation values and variances may then depend on the configuration $c$. It thus becomes relevant in which order $c$-averages over configurations $c$ and $k$-averages over time series $k$ of a given configuration $c$ are performed. Three variances

of $v[\mathbf{x}_{ck}]$ must be distinguished. The total variance

$$\delta v_{\text{tot}}^2 = \delta v_{\text{int}}^2 + \delta v_{\text{ext}}^2 \tag{2.45}$$

and its two contributions $\delta v_{\text{int}}^2$, the typical internal variance within each meta-basin, and $\delta v_{\text{ext}}^2$, characterizing the dispersion between the different basins. Importantly, *if* the trajectory of each confined configuration $c$ remains essentially Gaussian, Wick's theorem can be applied to $\delta v_{\text{int}}$ as before (see Appendix A.6). This implies $\delta v_{\text{int}} \approx \delta v_{\text{G}}$ according to Eq. A.32. Moreover, since $\delta v_{\text{ext}}(\Delta t) \approx \Delta_{\text{ne}}$ for $\tau_{\text{b}} \ll \Delta t \ll \tau_\alpha$, this leads finally to Eq. 2.43.

Variances due to independent physical causes are naturally additive. We remind that the variance of the blackbody radiation is thus the sum of a variance describing the Rayleigh-Jeans part of the spectrum (wave aspect) and of a variance describing the Wien part (discrete particle aspect) [114]. Interestingly, as in the blackbody radiation analogy the two contributions $\delta v_{\text{int}}$ (internal fluctuations within each basin) and $\delta v_{\text{ext}}$ (fluctuations between the different basins) to $\delta v_{\text{tot}}$ have also in general different statistics. This is manifested by their different system size dependencies as will be shown now.

## 2.7  Microscopic variables and system-size effects

Due to the central limit theorem [112] the stochastic process of many systems is to a good approximation Gaussian since the data entries $x_i$ are averages over $N_{\text{m}} \gg 1$ microscopic contributions $x_{im}$. These contributions are often not known or accessible. Specifically, we shall consider in this thesis the instantaneous shear stress $\hat{\tau}_i = \int d\underline{r}\, \hat{\tau}_{i,\underline{r}}/V$ being the volume average over the local shear stress $\hat{\tau}_{i,\underline{r}}$. For such intensive field averages $N_{\text{m}}$ corresponds to the number of local volume elements $dV$ computed, i.e. $N_{\text{m}} \approx V/dV$. Albeit these microscopic contributions $x_{im}$ may be correlated, i.e. they may not all fluctuate independently, the fluctuations of the $x_i$ commonly decrease with increasing $N_{\text{m}}$. Since $v \propto 1/N_{\text{m}}$ for uncorrelated variables $x_{im}$, it is often useful to incorporate this reference in the definition of the data entries by rescaling $x_i \Rightarrow \sqrt{N_{\text{m}}}x_i$. Summarizing the scaling for the trivial case of perfectly uncorrelated variables $x_{im}$ we thus have

$$v \propto h \propto \delta v_{\text{G}} \propto N_{\text{m}}^0 \text{ and } \Delta_{\text{ne}} \propto 1/N_{\text{m}}^{\gamma_{\text{ext}}} \text{ with } \gamma_{\text{ext}} = 1/2 \tag{2.46}$$

if the microscopic states are subject to an uncorrelated quenched random field. That this holds is shown in Appendix A.7. Due to Eq. 2.3 the $N_{\mathrm{m}}$-independence of $\delta v_{\mathrm{G}}$ is implied by the $N_{\mathrm{m}}$-independence of $h$. Equation 2.46 also holds for fluctuating density fields with a finite $V$-independent correlation length $\xi$ for sufficiently large systems ($V \gg \xi^d$). In this case $N_{\mathrm{m}}$ in Eq. 2.46 is simply replaced by the number of independent subvolumes $V/\xi^d$. A smaller exponent $\gamma_{\mathrm{ext}} < 1/2$ is expected for long-range and scale-free spatial correlations. The important point here is that $\Delta_{\mathrm{ne}}$ must decrease with the system size *if $\gamma_{\mathrm{ext}} > 0$* and thus $\delta v \to \delta v_{\mathrm{G}}$ for $N_{\mathrm{m}} \to \infty$ according to Eq. 2.43.

## 2.8 Shear-stress fluctuations

The notions and results presented in this chapter should be useful for the analysis of general time series **x**. We apply them in the following to the shear-stress fluctuations in film systems using the more common notations in the literature [1, 3, 6, 63, 65–67, 77, 101, 105]. The entries $x_i$ of the time series thus correspond to $\sqrt{\beta V}\hat{\tau}$ with $\beta = 1/T$ being the inverse temperature (setting Boltzmann's constant $k_{\mathrm{B}}$ to unity), $V$ the volume of the system and $\hat{\tau}$ to the instantaneous shear stress measured at a time $i\delta t$. The relevant Born-Lamé coefficient $R_{\mathrm{A}}$ is now called $\mu_{\mathrm{A}}$ and its instantaneous value $\hat{\mu}_{\mathrm{A}}$. The definitions of $\hat{\tau}$ and $\hat{\mu}_{\mathrm{A}}$ are detailed in Appendix B.1. The ensemble-averaged time-averaged variance $v(\Delta t)$ becomes the *shear-stress fluctuation*, the overbar denoting the $t$-average over time series:

$$v(\Delta t) \to \mu_{\mathrm{F}}(\Delta t) \equiv \mu_0 - \mu_1(\Delta t) \text{ with} \tag{2.47}$$

$$m_{21} \to \mu_0 \equiv \beta V \left\langle \overline{\hat{\tau}^2} \right\rangle \text{ and} \tag{2.48}$$

$$m_{12}(\Delta t) \to \mu_1(\Delta t) \equiv \beta V \left\langle \overline{\hat{\tau}}^2 \right\rangle. \tag{2.49}$$

The linear response function $R(t)$ and the modulus $M(\Delta t)$ are written now as [65–67, 77, 101]

$$R(t) \to G(t) = \mu_{\mathrm{A}} - h(t) = (\mu_{\mathrm{A}} - c(0)) + c(t) \tag{2.50}$$

$$M(\Delta t) \to \mu(\Delta t) = \mu_{\mathrm{A}} - \mu_{\mathrm{F}}(\Delta t) = (\mu_{\mathrm{A}} - \mu_0) + \mu_1(\Delta t) \tag{2.51}$$

with the single averages $c(0) = \mu_0$ and $\mu_A = G(0) = \mu(0)$. Eq. 2.50 is the fluctuation dissipation relation [3] for the shear-stress relaxation after an infinitesimal change of the shear strain, Eq. 2.51 the corresponding relation for the shear modulus (Appendix B.2). The *additional* assumption $\mu_A = \mu_0$ implies

$$G(t) = c(t) \text{ and } \mu(\Delta t) = \mu_1(\Delta t). \tag{2.52}$$

Unfortunately, while $\mu_A = \mu_0 = c(0)$ holds indeed under liquid equilibrium conditions,[11] this may become incorrect in general [63, 101]. Eq. 2.50 and Eq. 2.51 must thus be used in the more general case.

As discussed in Sec. 2.6 and Appendix A.5, three different types of standard deviations will be distinguished in Ch. 7:

- $\delta v_{\text{tot}} \to \delta\mu_{\text{F,tot}}$ by lumping all $N_c \times N_k$ time series together (Eq. A.24);

- $\delta v_{\text{int}} \to \delta\mu_{\text{F,int}}$ by "$c$-averaging" the "$k$-averaged variances" $\delta\mu_{\text{F,c}}^2$ (Eq. A.25);

- $\delta v_{\text{G}} \to \delta\mu_{\text{F,G}}$ according to Eqs. 2.35, A.1, A.2, A.3 using the measured correlation function $h(t)$ or, equivalently, $c(t)$ or $G(t)$.

Rephrasing the general relation Eq. 2.43 for shear-stress fluctuations we shall verify numerically that,

$$\delta\mu_{\text{F,int}} = \delta\mu_{\text{F,G}} \text{ and } \delta\mu_{\text{F,tot}} \approx \sqrt{\delta\mu_{\text{F,int}}^2 + \Delta_{\text{ne}}^2} \tag{2.53}$$

where the non-ergodicity parameter $\Delta_{\text{ne}} \geq 0$ characterizes the dispersion of $v_c \to \mu_{\text{F,c}}$ for different configurations $c$ (cf. Appendix A.6). As we will see in Ch. 7, $\delta\mu_{\text{F,int}} \sim 1/\sqrt{\Delta t}$ vanishes rapidly with $\Delta t$. Therefore, we may determine $\Delta_{\text{ne}}$ from the $\Delta t$-independent plateau of $\delta\mu_{\text{F,tot}}$ in this limit.

---

[11] $\mu = \mu_A - \mu_0 + \mu_1$ must vanish for liquids, $\mu \approx 0$, and since $\mu_1 \approx 0$ by symmetry, this implies $\mu_A \approx \mu_0$.

This page intentionally left blank.

# Chapter 3

# Computational model and some technical details

## 3.1 Introduction

The preceding chapter has summarized useful general theoretical relations. These relations can of course be tested computationally once we identify a suitable computational model system. The primary computational tool that we use in our study is molecular dynamics (MD) simulations [57, 58]. Molecular dynamics works by solving classical equations of motion for a system of particles that interact with a well defined potential. One of the most modern programs that can perform this job using task parallelism is the Large-scale Atomic Molecular Massively Parallel Simulator, also known as LAMMPS [58]. We describe in this chapter the specific features of our polymer model (Sec. 3.3), the configuration ensembles used (Sec. 3.4), the quench protocol (Sec. 3.5) and the data handling (Sec. 3.6). How the layer-resolved film properties discussed in Ch. 6 are computed is shown in Sec. 3.7.

## 3.2 Lennard-Jones particles

As in a huge number of similar numerical studies of coarse-grained model systems [36, 37, 40, 47, 63–70, 93, 95, 98, 102, 104, 115–119] we use the $12 - 6$ Lennard-Jones (LJ) pair potential [57, 78]

$$u_{\text{LJ}}(r) = \epsilon_{\text{LJ}} \left( (\sigma_{\text{LJ}}/r)^{12} - (\sigma_{\text{LJ}}/r)^6 \right) \qquad (3.1)$$

to characterize the monomers of our polymer chains.[12] Here, $r$ is the distance between the interacting beads, $\sigma_{\mathrm{LJ}}$ and $\epsilon_{\mathrm{LJ}}$ are the characteristic LJ distance and energy units. Please note that the LJ potential is usually truncated for computational efficiency at $r_{\mathrm{cut}} = 2.3 \approx 2r_{\mathrm{min}}$, with $r_{\mathrm{min}} = 2^{1/6}$ being the potential minimum, and shifted to make it continuous:

$$u_{\mathrm{LJ}}(r) \; \Rightarrow \; u_{\mathrm{LJ,trunc}}(r) = u_{\mathrm{LJ}}(r) - u_{\mathrm{LJ}}(r_{\mathrm{cut}}) \text{ for } r \leq r_{\mathrm{cut}}. \tag{3.2}$$

Unfortunately, the truncated and shifted potential is *not* continuous with respect to its first derivative.[13] Therefore, impulsive truncation corrections are required for the determination of the affine shear modulus $\mu_{\mathrm{A}}$ (Appendix B.1) [63, 78, 98].[14] All quantities reported are in LJ units, i.e. the parameters of the LJ potential are set to unity, $\epsilon_{\mathrm{LJ}} = 1$, $\sigma_{\mathrm{LJ}} = 1$, $m = 1$, and $k_{\mathrm{B}} = 1$. It is implied that they are also non-dimensional (denoted with a star superscript $^{\star}$), for instance the reduced distance $r^{\star} = r/\sigma_{\mathrm{LJ}}$, the reduced time $t^{\star} = t/\tau_{\mathrm{LJ}}$ with $\tau_{\mathrm{LJ}} = (m\sigma_{\mathrm{LJ}}^2/\epsilon_{\mathrm{LJ}})^{1/2}$ and the reduced temperature $T^{\star} = T/(\epsilon_{\mathrm{LJ}}/k_{\mathrm{B}})$. In the following, we will drop the star in order to simplify the notation.

## 3.3 Coarse-grained polymer chains

As already mentioned in Ch. 1, we are primarily interested in freestanding polymer films. Computationally it is not trivial to simulate an all-atom polymer model to prepare such films. We thus work with a variant of a widely-used coarse-grained bead-spring model [58, 62]. In this model variant the interaction potential between permanently bonded neighboring monomers of the chain is a spring potential:

$$u_{\mathrm{bond}}(r) = \frac{k_{\mathrm{bond}}}{2} \left( r - l_{\mathrm{bond}} \right)^2. \tag{3.3}$$

Here, $r$ is the distance between the permanently connected beads, $k_{\mathrm{bond}} = 1110$ the spring constant, and $l_{\mathrm{bond}} = 0.967$ the bond length. All *inter*-chain monomers interact via the 12-6 LJ potential [57] defined in Eq. 3.1. All *intra*-chain monomers that are not connected

---

[12]Naturally, LJ beads are of interest for an enormously large class of models in statistical mechanics far beyond the polymer model they are used for in the present thesis. In fact, our group recently studied [69, 70] a glass former composed of polydisperse LJ beads to verify many properties discussed in Ch. 2.

[13]This is problem is nicely resolved in Procaccia's work [118].

[14]The additive correction $\Delta\mu_{\mathrm{A}}$ due to this truncation effect can be estimated using the methods developed in Ref. [98] as $\Delta\mu_{\mathrm{A}} \approx -0.2$. Temperature effects are negligible.
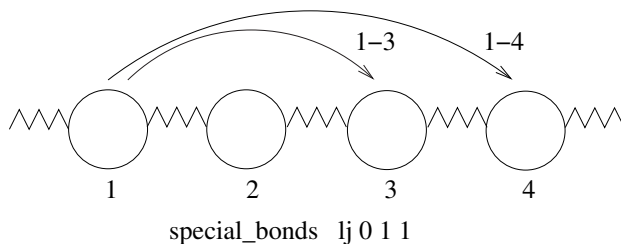
Figure 3-1: Intra-chain monomers that are not connected by permanent bonds interact via the 12-6 LJ potential but with a weight specified in LAMMPS [58]. By doing so, the interaction to the nearest bead in the same chain is turned off (as it is handled by Eq. 3.3)

permanently also interact via the same potential but with a weight[15] (cf. Fig. 3-1) using the `special_bonds lj 0 1 1` command in LAMMPS [58]. These model parameters make the chains flexible in nature. This coarse-grained model was not only chosen due to its simplicity, but also due to its good correspondence (mapping) to experimental results [59–61]. Moreover, the present model has been used in several other recent publications of the Strasbourg polymer theory and simulation group (ETSP-ICS) [36, 37, 61, 65–70, 95]. Importantly, the model parameters are chosen such that the crossing of chains is in practice impossible in our model. Hence, reptational chain dynamics [2, 3, 6] would become important for long chains with $N \gg N_e$. However, since the entanglement length $N_e \approx 100$ [62, 120–122] is much larger than the chain length $N = 16$ used in the present study, Rouse-type dynamics (Appendix C) [6] is observed at high temperatures. All results presented in this thesis have been obtained by means of MD simulation performed using LAMMPS [58]. We use a velocity-Verlet scheme [57] with a time step $\delta t_{MD} = 0.005$. Temperature is imposed by means of the Nosé-Hoover algorithm also provided by LAMMPS.

## 3.4 Film and bulk ensembles

In Fig. 1-1 we showed the general setup of our free-standing polymer films. As visualized from an actual simulation, the snapshot Fig. 3-2 shows a film suspended parallel in the $(x, y)$-plane of a simulation box with lateral box size $L_x = L_y = L$. To prepare[16] films

---

[15]These weights are set to unity, except for the nearest bead in the same chain. The nearest bead interaction weight is set to zero, as this interaction is already handled by the bond (spring) potential.

[16]All of the LAMMPS input scripts used to simulate our freestanding films can be found in the following University of Strasbourg (GitLab) code repository (project visibility – internal): https://git.unistra.fr/thatgeeman/nvtf
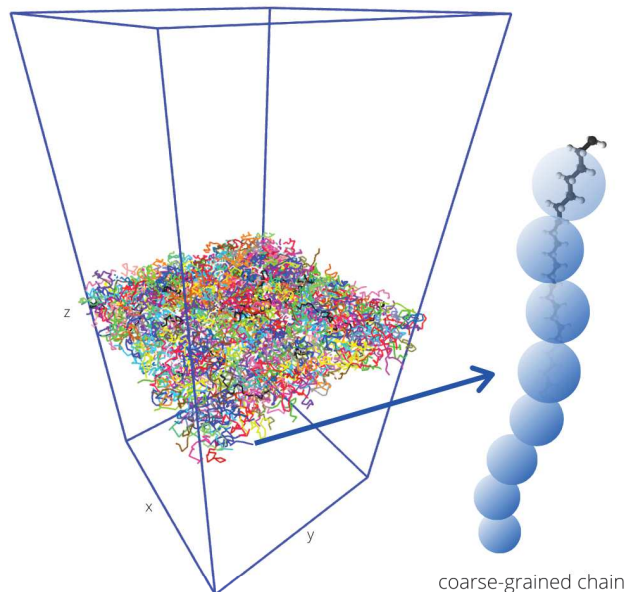
Figure 3-2: Our films consists of $M = 768$ coarse-grained polymer chains of length $N = 16$. The visualization on the left is obtained using VMD [123] for *film4* with $L = 49$ (Sec. 3.4). The illustration on the right shows the essence of coarse-graining for a single chain where chemical details are deemed irrelevant.

of varying thicknesses we do not directly vary the film thickness $H$, but rather impose the lateral box size $L$. We simulate ensembles with either $L = 23.5$ (*film1*), $L = 37.1$ (*film2*), $L = 42$ (*film3*) or $L = 49$ (*film4*). The smallest $L$ corresponds to our thickest film, *film1*, which will be the main subject of discussion in Chs. 5-7 of this thesis. For our polymer model, we prepare a system with $M = 768$ chains of length $N = 16$ (with uniform dispersity), i.e. a total of $n = 12288$ beads (monomers) in a periodic box. Please note that ensemble averages over $N_c = 120$ independently quenched configurations are performed for *film1*, much more than the $N_c = 10$ configurations considered for all other ensembles.

As shown in Fig. 3-2 the vertical box size $L_z$ is chosen sufficiently large ($L_z \gg H$) to avoid any interaction in this direction arising from the periodic boundary conditions. The instantaneous stress tensor [57] thus vanishes rigorously outside the films. While this implies for all $z$-planes within the films that the average vertical normal stress $\sigma_{zz}(z)$ must vanish [34], some of the (average) tangential normal stresses $\sigma_{xx}(z)$ and $\sigma_{yy}(z)$ must be finite. The surface tension $\Gamma$ [34, 57] would otherwise vanish and the films become unstable. Note that $\Gamma$ is of order unity for temperatures close to the glass transition as indicated in Table 3.1.

| System | $L$ | $N_c$ | $T_g$ | $H$ | $\mu_A$ | $\mu_F$ | $\mu$ | $R_G$ | $R_e$ | $H/R_G$ | $\rho_0$ | $\Gamma$ |
|---|---|---|---|---|---|---|---|---|---|---|---|---|
| 3D bulk | - | 10 | 0.395 | - | 93.3 | 84.6 | 8.7 | 1.9 | 4.6 | - | - | - |
| film1 | 23.5 | 120 | 0.371 | 21.3 | 93.9 | 85.6 | 8.3 | 1.9 | 4.6 | 11.3 | 1.045 | 0.89 |
| film2 | 37.1 | 10 | 0.334 | 8.5 | 94.2 | 86.1 | 8.1 | 1.9 | 4.6 | 4.5 | 1.054 | 1.58 |
| film3 | 42 | 10 | 0.318 | 6.6 | 94.3 | 86.5 | 7.8 | 1.9 | 4.6 | 3.5 | 1.057 | 1.57 |
| film4 | 49 | 10 | 0.290 | 4.8 | 94.9 | 87.4 | 7.5 | 1.8 | 4.4 | 2.6 | 1.063 | 1.61 |

Table 3.1: Some properties at the glass transition for the bulk and for films of different lateral box sizes $L$ ensemble-averaged over $N_c$ independent configurations: glass transition temperature $T_g$, film thickness $H$, affine shear modulus $\mu_A$, shear-stress fluctuation $\mu_F$, shear modulus $\mu$ according to Eq. 1.1, radius of gyration $R_G$ and end-to-end distance $R_e$ [3, 6], ratio $H/R_G$, the plateau density $\rho_0$ and the surface tension $\Gamma$ discussed in Sec. 6.4. The bulk results have been obtained at a pressure $P = 0$ using cubic periodic boxes. As emphasized in Sec. 4.4, $\mu_F$ and $\mu$ have been obtained for a sampling time $\Delta t = 10^4$.

Details on the surface tension are given in Sec. 6.4. As clarified in Appendix B.1 for $\mu_A$, it is thus generally not appropriate to neglect the surface tension contribution to the Born-Lamé coefficients of thermodynamically stable films [44].

For comparison we also look at three-dimensional (3D) bulk systems with same chain length $N$ and chain number $M$. These bulk systems have been computed in the NPT-ensemble using cubic periodic boxes and imposing an average pressure $P = 0$.[17] The ensembles used for bulk and film systems are in-effect similar, but not exactly identical as it would have been the case by imposing a vanishing normal stress $\sigma_{zz}$ in the $z$-direction at a constant linear box length $L$ in $x$- and $y$-directions. Fortunately, as will be shown in Ch. 4, this difference appears irrelevant since the film data properly extrapolate to the bulk data if plotted as a function of $1/H$, i.e. the bulk data corresponds formally to the limit $1/H \to 0$. Table 3.1 summarizes some static properties and relevant information regarding all ensembles taken at the glass transition temperature $T_g$.

## 3.5    Quench protocol

Starting with an equilibrated three-dimensional polymer melt at $P = 0$ and $T = 0.7$ simulated in a cubic simulation box with $L_x = L_y = L_z$ the vertical box dimension $L_z$ is strongly increased leading to a thin polymer film suspended in the $(x, y)$-plane. This film

---

[17]These systems have been prepared by Ivan Kriuchevskyi during his PhD at the Strasbourg polymer theory and simulation group (ETSP-ICS) [65–67, 103].
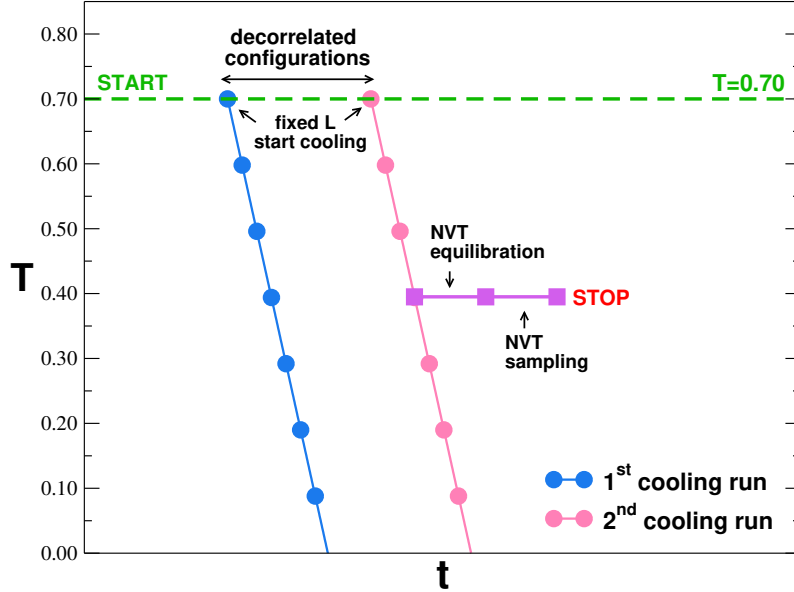
Figure 3-3: Quench protocol as described in the text. The lateral and perpendicular box dimensions $L$ and $L_z$ are imposed. While the total box volume $L^2 L_z$ and the film surface $A = L^2$ for each film are thus kept constant, the actual film volume $V = L^2 H$ is an observable depending on the temperature $T$ and the quench protocol.

with $L = 23.5$ (*film1*) was equilibrated at $T = 0.7$. Starting from this configuration *film2*, *film3* and *film4* were created by gently increasing the lateral box dimension to, respectively, $L = L_x = L_y = 37.1$, 42.0 and 49.0. All four films were again thoroughly equilibrated at $T = 0.7$. We thus generate $N_c = 120$ independent configurations for *film1* and $N_c = 10$ independent configurations for *film2*, *film3* and *film4* (Table 3.1). We then quench each of the independent configurations at a fixed lateral box size $L$, i.e. at an imposed film area $A = L^2$, using a constant cooling rate, $T(t) = 0.7 - 2 \times 10^{-5} t$. See Fig. 3-3 for an illustration. Note that $L_z$ is always sufficiently large to be irrelevant for all films. While we impose the total box volume $L^2 L_z$ and the film area $A = L^2$, the film volume $V = L^2 H$ is a freely fluctuating observable which needs to be determined as discussed in Sec. 4.2. From each cooling run, configurations at several temperatures[18] (from $T = 0.55 \to 0.05$, with 0.05 spacing) are picked and stored. Imposing then a constant temperature, each stored configuration is tempered ($\Delta t_{temp} = 10^5$) and then sampled ($\Delta t_{max} = \Delta t = 10^5$). The quench and production protocols are the same for all films and 3D bulk systems.

---

[18]The temperature at a given time during the cooling run is known from the cooling rate. In addition, the log file produced during the cooling run provides the instantaneous temperature fixed by the thermostat, allowing for comparison.

## 3.6  Data sampling and processing

Instantaneous observables $x_i$ (for instance, stresses $\hat{\sigma}_{\alpha\beta}$) are sampled every $10\delta t_{\mathrm{MD}}$ with $\delta t_{\mathrm{MD}} = 0.005$ being the time increment of the velocity-Verlet scheme used. This corresponds to a data file with entries every $\delta t = 0.05$ step. Whereas LAMMPS trajectory files with particle coordinates are written every $10^5 \times \delta t_{\mathrm{MD}}$ timestep ($\delta t_{\mathrm{trj}} = 500$ LJ timestep). An additional set of configurations $N_{\mathrm{c}} = 10$ for *film1* was prepared using $500 \times \delta t_{\mathrm{MD}}$ timestep ($\delta t_{\mathrm{trj}} = 2.5$ LJ timestep), so as to improve the resolution of our findings[19] in Ch. 6 for layer-resolved properties (Sec. 3.7.) Of central importance are the excess contributions of instantaneous shear stress $\hat{\tau}$ and the instantaneous affine shear modulus $\hat{\mu}_{\mathrm{A}}$ defined in Appendix B.1.[20] As discussed in Sec. 2.2 and Sec. 2.8, the stored time-series $\mathbf{x} = \{x_i, i = 1, \ldots I\}$ for each $N_{\mathrm{c}}$ configuration $c$ are used to compute various *t-averages*. By averaging over the $N_{\mathrm{c}}$ independent configurations, we obtain then *ensemble averages* or "c-averages".

In addition to this we need to compute for Ch. 7 "*k*-averages" and "*k*-variances" over $N_{\mathrm{k}}$ time series $\mathbf{x}_{ck}$ of each configuration $c$ as described in detail in Appendix A.4 and Appendix A.5. Since we want to investigate the dependence of various properties on the sampling time $\Delta t$ we probe for each $\Delta t_{\max}$-trajectory $N_{\mathrm{k}}$ equally spaced subintervals $k$ of length $\Delta t \leq \Delta t_{\max}$ with $I = \Delta t / \delta t$ entries. It is inessential for all properties discussed in the present work whether these subintervals do partially overlap or do not. Since overlapping subintervals probe similar information it is, however, numerically not efficient to pack them too densely. We use generally $N_{\mathrm{k}} = \Delta t_{\max} / \Delta t$, i.e. $N_{\mathrm{k}}$ and $\Delta t$ are thus coupled and the accuracy is better for small $\Delta t$. Essentially, the same data averaging procedure is used for the bulk systems the only difference being that we average finally in addition over the three equivalent shear planes.

## 3.7  Calculation of layer resolved properties

We shall investigate in Ch. 6 the local $z$-distributions of many properties such as the distributions $\hat{\rho}(z)$ of the number density $\hat{\rho}$ (Sec. 6.2), $\hat{e}(z)$ of the energy density $\hat{e}$ (Sec. 6.3),

---

[19]Layer-resolved analysis of dynamic properties requires access to the instantaneous particle positions, i.e. $\delta t_{\mathrm{trj}} \to \delta t$ ideally.

[20]All intensive properties are to be re-normalized using the effective film volume $V = L^2 H$ with $H$ being the film thickness defined in Sec. 4.2. This is an essential step for freestanding films as LAMMPS computes all intensive properties with respect to the simulation box volume $V = L^2 L_{\mathrm{z}}$ instead.

$\hat{\sigma}_{\alpha\beta}(z)$ of the stresses $\sigma_{\alpha\beta}$ (Sec. 6.4), $\hat{\mu}_{\mathrm{A}}(z)$ of the affine shear modulus $\hat{\mu}_{\mathrm{A}}$ (Sec. 6.5) and $\mu_{\mathrm{F}}(z)$ of the stress fluctuation term $\mu_{\mathrm{F}}$ (Sec. 6.6). All these distributions are computed following the Irving-Kirkwood convention [34, 57, 78]:

- The ideal contributions for each bin are due to the particles located in the bin.

- The excess contributions due to the bonded and non-bonded pair potentials are distributed equally with a weight $1/n_{ij}$ to the $n_{ij} = |z_{bi} - z_{bj}|/\delta z_{\mathrm{b}} + 1$ bins containing the line that connects a particle $i$ at $z_i$, located in a bin at $z_{bi}$, with a particle $j$ at $z_j$, located in a bin at $z_{bj}$.

It is useful to write the Irving-Kirkwood convention compactly in terms of two normalized weighting functions. With $z_b$ and $z_i$ being, respectively, the $z$-coordinates of a bin and a particle the weighting function $w_{\mathrm{id}}(z_b; z_i)$ of the ideal contributions is given by

$$V_{\mathrm{b}} \ w_{\mathrm{id}}(z_b; z_i) = \begin{cases} 1 & \text{if } |z_b - z_i| < \delta z_{\mathrm{b}}/2 \\ 0 & \text{otherwise.} \end{cases} \tag{3.4}$$

The weighting function $w_{\mathrm{ex}}(z_b; z_i, z_j)$ used for the excess contributions is defined by

$$V_{\mathrm{b}} w_{\mathrm{ex}}(z_b; z_i, z_j) = \begin{cases} 0 & \text{if } \max(z_{bi}, z_{bj}) < z_b \\ 0 & \text{if } \min(z_{bi}, z_{bj}) > z_b \\ 1/n_{ij} & \text{otherwise.} \end{cases} \tag{3.5}$$

Note that the two weighting functions are normalized as

$$V_{\mathrm{b}} \sum_{b=1}^{n_{\mathrm{b}}} w_{\mathrm{id}}(z_b; z_i) = 1 \tag{3.6}$$

$$V_{\mathrm{b}} \sum_{b=1}^{n_{\mathrm{b}}} w_{\mathrm{ex}}(z_b; z_i, z_j) = 1 \tag{3.7}$$

with $n_{\mathrm{b}}$ being the number of bins (slabs). The implementation used for the calculation of $\sigma_{\alpha\beta}(z)$ and $\mu_{\mathrm{F}}(z)$ is available on GitLab.[21] Note that by using these normalized weighting functions the distributions are the *linear-additive* contributions to the total film properties

---

[21] The following University of Strasbourg (GitLab) repository (project visibility – internal) contains the code for this method: `https://git.unistra.fr/thatgeeman/elastic_layered`

following the (exact) *sum rule*

$$\hat{a} \overset{!}{=} \frac{\delta z_{\mathrm{b}}}{H} \sum_{b=1}^{n_{\mathrm{b}}} \hat{a}(z_b) \approx \frac{1}{H} \int \mathrm{d}z \; \hat{a}(z) \tag{3.8}$$

with $\hat{a}$ being the (instantaneous) *total* intensive film property and $\hat{a}(z_b)$ its contribution in bin $b$. Note also that using this convention the total film property $\hat{a}$ has the same dimension as its $z$-distribution $\hat{a}(z)$.

This page intentionally left blank.

# Chapter 4

# Total properties of polymer films

## 4.1 Introduction

We now discuss some global static and dynamical properties of our free-standing films. The outline of this chapter is as follows: In Sec. 4.2, we characterize the film thickness $H$ and identify the pseudo-thermodynamic glass transition temperature $T_\mathrm{g}$. In Sec. 4.3 and Sec. 4.4, we discuss the (generalized) shear modulus $\mu$ as a function of temperature $T$ and sampling time $\Delta t$. In Sec. 4.5, we use the Einstein relation to obtain the shear viscosity $\eta$ for $T \gg T_\mathrm{g}$, which is then used to obtain a relative scale for the terminal relaxation time $\tau_\alpha$. The TTS scaling of $\mu$ is presented in Sec. 4.6. In Sec. 4.7, we present the response function $G(t)$ and use the same shift parameters as for $\mu$ to obtain a TTS scaling. The total monomer mean-square displacements (MSD) will be discussed in Sec. 4.8. A summary is given in Sec. 4.9.

## 4.2 Film thickness and glass transition temperature

A central (geometric) parameter describing our films is its thickness $H$ (cf. Fig. 1-1). We determine $H$ using a Gibbs dividing surface construction [36, 39, 124]. With $\rho_0 \equiv \rho(z \approx 0)$ being the midplane density of the density profile $\rho(z)$, this implies

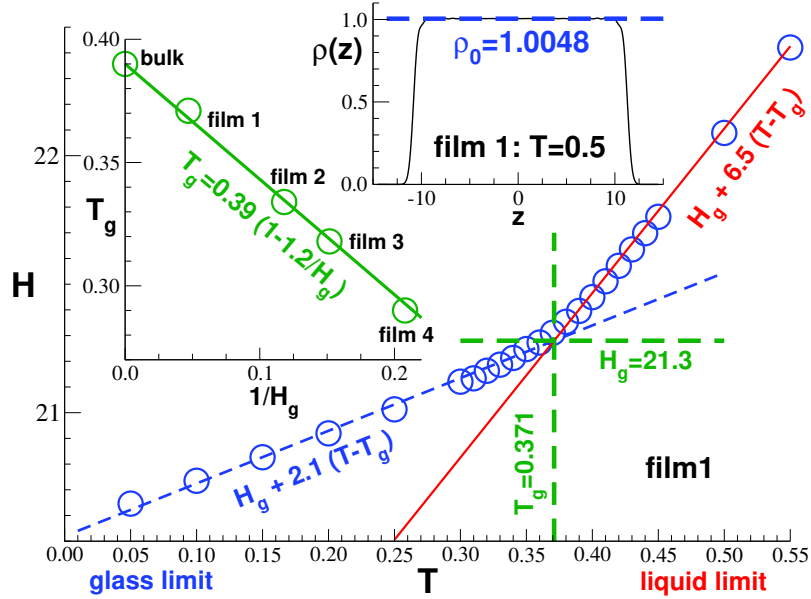$$H \equiv n/\rho_0 L^2 \quad \text{with } n = NM \tag{4.1}$$

Figure 4-1: Film thickness and glass transition temperature. Top inset: Number density profile $\rho(z)$ for $T = 0.50$ with $z = 0$ corresponding to the center of mass of each film. The midplane density $\rho_0 \approx 1$ is indicated by the dashed horizontal line. Main panel: $H$ as a function of temperature $T$ for *film1*. The glass transition temperature $T_{\mathrm{g}}$ and the film thickness $H_{\mathrm{g}}$ at the transition (bold dashed lines) are operationally defined by the intercept of the linear extrapolations of the glass (dashed line) and liquid (solid line) limits. Left inset: $T_{\mathrm{g}}$ as a function of $1/H_{\mathrm{g}}$ confirming the linear superposition, Eq. 1.3.

being the number of monomers. As seen for one example in the top inset of Fig. 4-1, $\rho(z)$ is always uniform and smooth around the midplane in agreement with the data presented in previous studies [41].[22] The plateau density $\rho_0$ can thus be fitted to high precision and, hence, also $H$. Since $\rho_0$ is always very close to unity, varying only little with $L$, Eq. 4.1 implies that (to leading order) $H \sim 1/L^2$ changes strongly with $L$. We present in the main panel of Fig. 4-1 the film thickness as a function of temperature. As emphasized by the dashed and the solid lines, $H$ decreases monotonically upon cooling with the two linear branches fitting reasonably the glass (dashed line) and the liquid (solid line) limits. The intercept (horizontal and vertical dashed lines) of both asymptotes allows to define the pseudo-thermodynamic $T_{\mathrm{g}}$ and the film thickness $H_{\mathrm{g}}$ at the transition (given in Table 3.1) [36, 41, 47]. (See Ref. [65] for bulk systems.)

As expected from a wealth of literature [8–10, 12, 13, 35–37, 39, 41, 45], $T_{\mathrm{g}}$ increases with $H$. More precisely, as seen in the left inset of Fig. 4-1, $T_{\mathrm{g}}$ extrapolates linearly with the

---

[22]The shape of the density profile is discussed in more detail in Sec. 6.2.
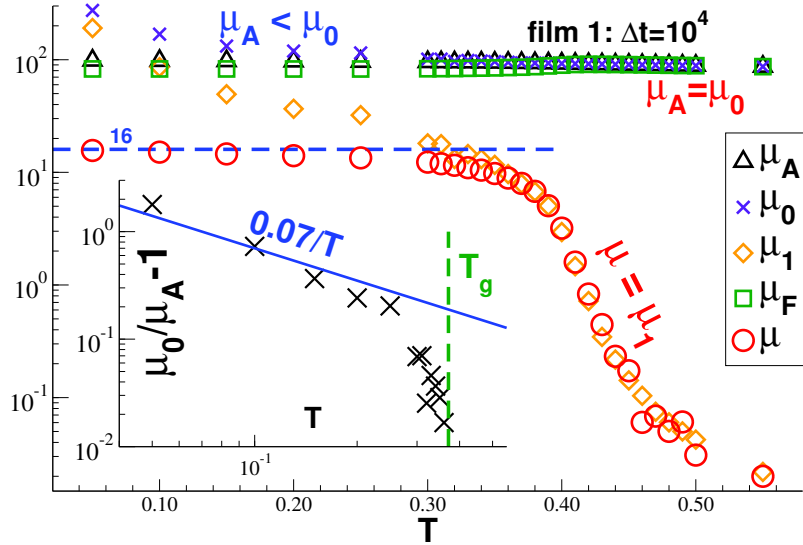
Figure 4-2: Comparison of the different contributions to the shear modulus $\mu = \mu_A - \mu_F = (\mu_A - \mu_0) + \mu_1$ as functions of $T$ focusing on data obtained for *film1* and $\Delta t = 10^4$. Inset: Double-logarithmic representation of $\mu_0/\mu_A - 1$ *vs* $T$.

inverse film thickness to the thick-film limit. The value $T_g = 0.395$ indicated at $1/H_g = 0$ stems from our bulk simulations.) This is consistent with the linear superposition, Eq. 1.3, of a thickness-independent bulk glass transition temperature $T_{g0}$ and an effective surface temperature $T_{gs}$.[23] The negative sign of the correction implies $T_{gs} < T_{g0}$, i.e. surface relaxation processes are *faster* than processes around the film midplane. This finding is also consistent with the higher monomer mobilities observed at the film surfaces in previous studies [7, 24, 26, 36, 39, 48]. We emphasize finally that many more data points covering a much broader range of orders of magnitude in $1/H$ are required to find or to rule out numerically higher orders of a systematic $1/H$-expansion of $T_g$.

## 4.3   Stress-fluctuation formula at fixed sampling time

Instantaneous values of the shear stress $\hat{\tau}$ and of the affine shear modulus $\hat{\mu}_A$ have been computed as described in Appendix B.1. The time and ensemble averaged affine shear modulus $\mu_A \equiv \langle \overline{\hat{\mu}_A} \rangle$ is presented in the main panel of Fig. 4-2 as a function of temperature using half-logarithmic coordinates. The averaged shear stress $\tau \equiv \langle \overline{\hat{\tau}} \rangle$ is not indicated since it vanishes rapidly due to symmetry with increasing ensemble size $N_c$ and sampling time

---

[23]As we shall demonstrate in Sec. 5.5 the linear superposition is also seen for real experimental data.
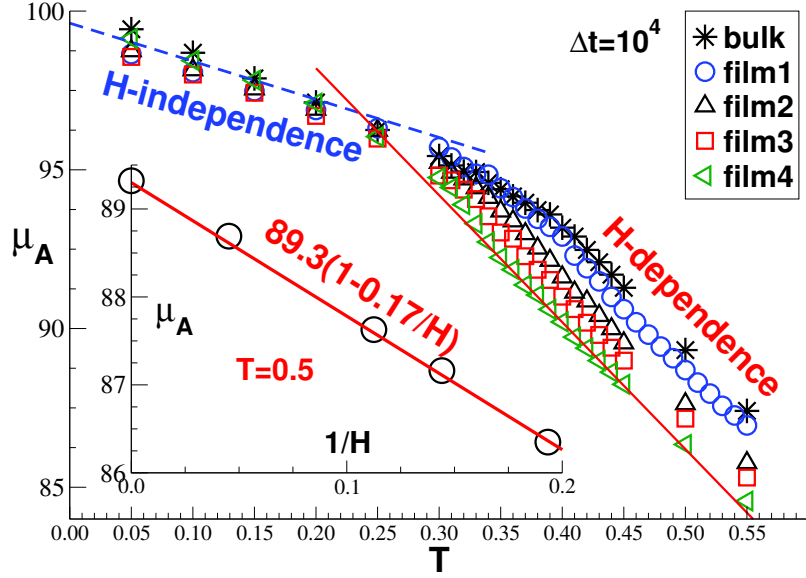
Figure 4-3: Affine shear modulus $\mu_A$. Main panel: $\mu_A(T)$ for all systems studied. Inset: As shown for $T = 0.50$, $\mu_A$ decreases linearly with $1/H$ in the liquid limit.

$\Delta t$. As seen from Fig. 4-2, this is not the case for the moments (with $\beta = \frac{1}{k_B T}$ being the inverse temperature) describing the non-affine contributions to the stress-fluctuation formula for the shear modulus (Appendix B.2)

$$\mu_0 \equiv \beta V \left\langle \overline{\hat{\tau}^2} \right\rangle, \ \mu_1 \equiv \beta V \left\langle \overline{\hat{\tau}}^2 \right\rangle \ \text{and} \ \mu_F \equiv \mu_0 - \mu_1. \tag{4.2}$$

Note that $\mu_F$, $\mu_0$ and $\mu_A$ depend only weakly on $T$ and are all similar on the logarithmic scale used in Fig. 4-2. As stressed by Eq. 2.52 and footnote 11, $\mu_A = \mu_0$ for an equilibrium liquid. Frozen-in out-of-equilibrium stresses are observed upon cooling below $T_g$ as made manifest by the dramatic increase of the dimensionless ratio $\mu_0/\mu_A - 1$. The $\beta$-prefactor of $\mu_0$, Eq. 4.2, implies that due to the frozen stresses,

$$\mu_0/\mu_A - 1 \sim 1/T \ \text{for} \ T \ll T_g \tag{4.3}$$

to leading order. This is consistent with the data presented in the inset of Fig. 4-2. Similar behavior has been reported for 3D polymer bulks [65].

Using a linear representation, the main panel of Fig. 4-3 presents $\mu_A(T)$ for all ensembles. This shows (more clearly than Fig. 4-2) that $\mu_A$ decreases continuously with temperature with two (approximately) linear branches in the glass and the liquid regimes as indicate by
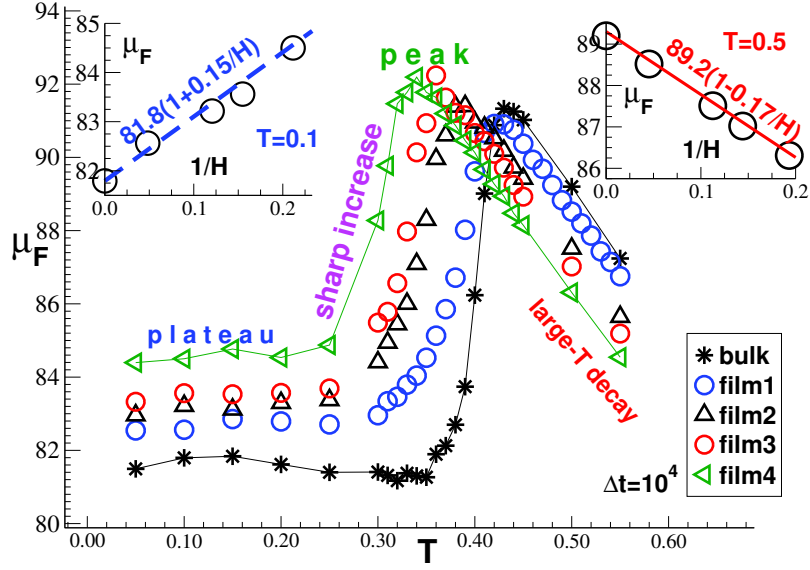
Figure 4-4: Shear-stress fluctuation $\mu_F$ for $\Delta t = 10^4$. Main panel: $\mu_F(T)$ for all systems. Right inset: $\mu_F$ decreases linearly with $1/H$ in the liquid limit ($T = 0.50$). Left inset: $\mu_F$ increases linearly with $1/H$ in the solid limit ($T = 0.10$).

the two lines. While $\mu_A$ barely depends on $H$ in the glass limit (suggesting a weak surface contribution $\mu_{As}$), it increases with $H$ in the liquid limit. As demonstrated in the inset, $\mu_A$ decreases in fact linearly with $1/H$ in agreement with Eq. 1.3. More details regarding the local characterization of $\mu_A$ are given in Sec. 6.5.

Using again a linear representation, $\mu_F(T)$ is presented in the main panel of Fig. 4-4. Upon cooling it increases linearly, goes through a well-defined peak located around $T_g$ and drops then rapidly albeit continuously. It becomes constant for $T \ll T_g$ when the shear stresses get quenched. Since $\mu_A \approx \mu_F$ at high temperatures, the same linear $1/H$-dependencies are naturally observed as shown in the right inset of Fig. 4-4 for $T = 0.50$. At variance to this, $\mu_F$ *increases* linearly with $1/H$ at low temperatures as seen for $T = 0.10$ in the left inset, i.e. the non-affine contributions are the largest for our thinnest films. Both linear $1/H$-relations for $\mu_F$ are consistent with Eq. 1.3. The negative sign of the correction for large $T$ suggests that the bulk value $\mu_{F0}$ in the middle of the films must exceed the value $\mu_{Fs}$ at the surfaces while the opposite behavior occurs in the low-$T$ limit. The shapes of the $z$-distribution $\mu_F$ in both temperature limits will be discussed in Sec. 6.6.

As already highlighted in the Introduction (main panel of Fig. 1-2) the shear modulus $\mu = \mu_A - \mu_F(\Delta t)$ depends on the film thickness just as its affine (Fig. 4-3) and non-affine (Fig. 4-4) contributions. As can also be seen there, $\mu(T)$ decays *continuously* in all cases
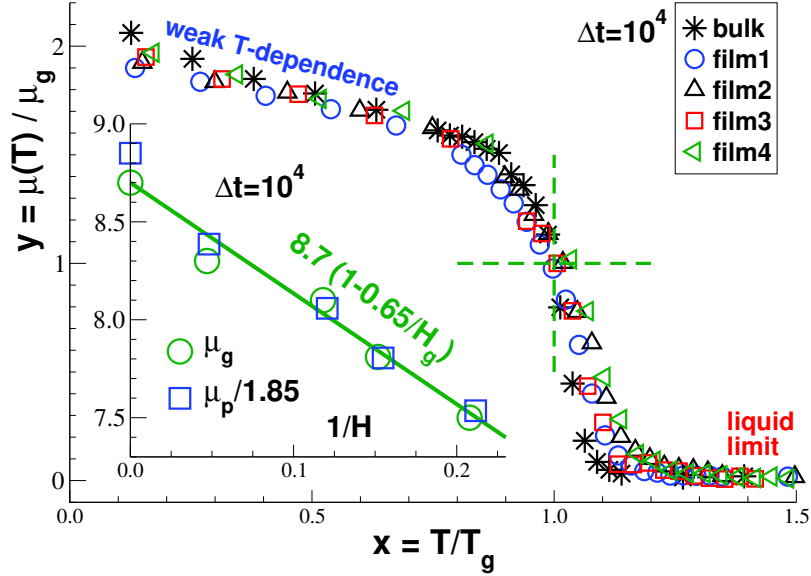
Figure 4-5: Film thickness dependence of $\mu(T)$ for $\Delta t = 10^4$. Main panel: Scaling collapse of $y = \mu(T)/\mu_\mathrm{g}$ vs $x = T/T_\mathrm{g}$. Inset: $\mu_\mathrm{g} \equiv \mu(T_\mathrm{g})$ and $\mu_\mathrm{p} \equiv \mu(T = 0.10)$ vs the inverse film thickness $1/H$ of the respective temperature. As emphasized by the bold line, both shear moduli are consistent with Eq. 1.3. We shall use $\mu_\mathrm{p}$ in Sec. 4.6 and Sec. 4.7 for the TTS scaling of $\mu(\Delta t)$ and $G(t)$ comparing different ensembles.

considered and no indication of a jump singularity is observed [125–129]. In the high-$T$ limit, $\mu$ vanishes $\mu \approx 0$. In the low-$T$ limit, the shear modulus becomes finite as expected. For our thinner films, as a consequence of reduced $T_\mathrm{g}$ and associated increase in mobility, $\mu$ vanishes for a wider range of temperatures. As shown in the main panel of Fig. 4-5, the shear moduli $\mu$ for films of different thickness can be brought to collapse on the $H$-independent mastercurves. (All data for the same fixed $\Delta t$.) The horizontal axis is rescaled with the reduced temperature $T/T_\mathrm{g}$ using the apparent glass transition temperature $T_\mathrm{g}$ defined in Sec. 4.2. The values $\mu_\mathrm{g} \equiv \mu(T_\mathrm{g})$ used to make the vertical axes dimensionless are indicated in Table 3.1 and plotted in the inset of Fig. 4-5. Consistently with the linear superposition relation, Eq. 1.3, $\mu_\mathrm{g}$ is a linear function of $1/H_\mathrm{g}$. Similar scaling plots could be given for the contributions $\mu_\mathrm{A}(T)$, $\mu_0(T)$, $\mu_1(T)$ and $\mu_\mathrm{F}(T)$.

## 4.4 Effective time-translational invariance

All data presented in the previous section have been obtained for one sampling time $\Delta t = 10^4$. We turn now to the characterization of the $\Delta t$-effects observed for $\mu$ in the inset of Fig. 1-2. Focusing on one temperature ($T = 0.30$) in the glass limit, we compare in
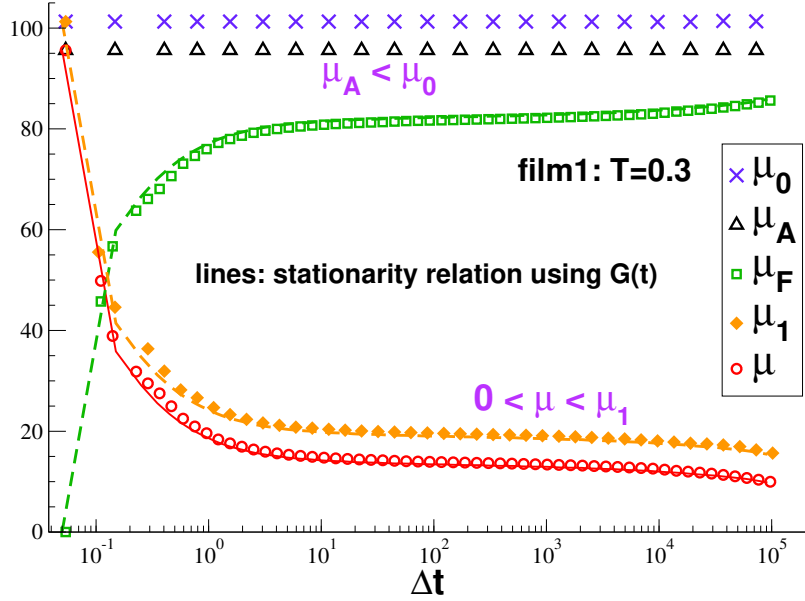
Figure 4-6: Sampling time effects for $\mu$ and its contributions focusing on *film1* and $T = 0.30$. Only the simple averages $\mu_A$ and $\mu_0$ are strictly $\Delta t$-independent. $\mu_1$ and (hence) $\mu$ decrease monotonically. The solid and dashes lines have been obtained using Eq. 1.2.

Fig. 4-6 the $\Delta t$-dependencies of $\mu_A$, $\mu_0$, $\mu_1$, $\mu_F$ and $\mu$. As expected from Eq. 2.8, the simple averages $\mu_A$ and $\mu_0$ are found to be strictly $\Delta t$-independent. Importantly, time and ensemble averages do not commute for $\mu_1$ since $0 = \beta V \overline{\langle \hat{\tau} \rangle^2} < \beta V \langle \overline{\hat{\tau}}^2 \rangle \equiv \mu_1(\Delta t)$, i.e. $\mu_1$ is not a simple average, but a fluctuation. As seen in Fig. 4-6, $\mu_1(\Delta t)$ decays in fact monotonically and, as a consequence, $\mu_F(\Delta t) = \mu_0 - \mu_1(\Delta t)$ increases and $\mu(\Delta t) = (\mu_A - \mu_0) + \mu_1(\Delta t)$ decreases monotonically. Interestingly, as indicated by the thin solid line, the stationarity relation Eq. 1.2 holds, i.e. $\mu(\Delta t)$ can be traced back from the independently determined shear-stress relaxation modulus $G(t)$ discussed below. (The visible minor differences are due to numerical difficulties related to the finite time step and the inaccurate integration of the strongly oscillatory $G(t)$ at short times.) Since $\mu_A$ and $\mu_0$ are $\Delta t$-independent simple averages, one can rewrite Eq. 1.2 to also describe $\mu_1(\Delta t)$ and $\mu_F(\Delta t)$. This is indicated by the two dashed lines. Note that Eq. 1.2 has been shown to hold for all temperatures and ensembles. The observed $\Delta t$-dependence of the shear modulus $\mu$ is thus not due to aging effects, but arises naturally from the effective time translational invariance of our systems. This does, of course, not mean that no aging occurs in our glassy systems, but just that this is irrelevant for the time scales and the properties considered here. We shall now use the decay of $\mu(\Delta t) \approx \mu_1(\Delta t)$ for large $T$ and $\Delta t$ to characterize the shear viscosity $\eta(T)$.
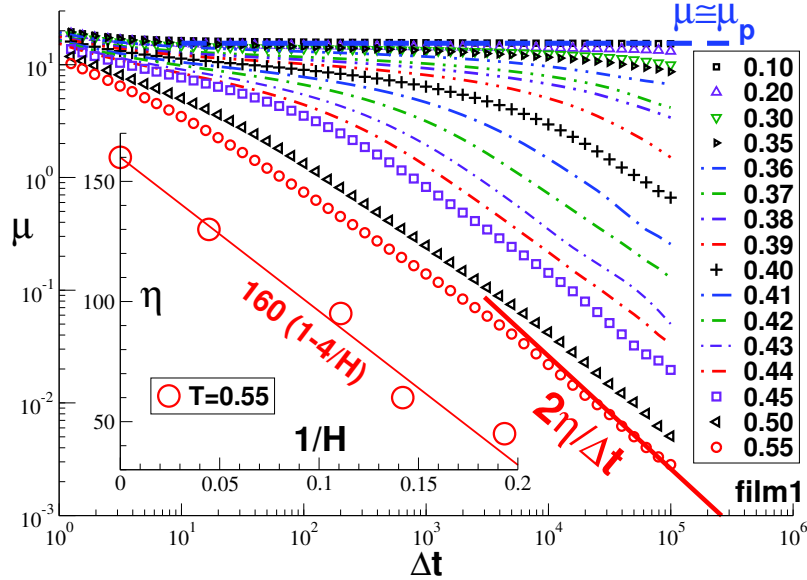
Figure 4-7: Double-logarithmic representation of $\mu(\Delta t)$ for a broad range of temperatures $T$ focusing on *film1*. $\mu(\Delta t; T)$ decreases continuously with both $\Delta t$ and $T$. A pseudo-elastic plateau is observed in the solid limit with $\mu \approx \mu_\mathrm{p} \approx 15.5$ (horizontal dashed line). The $1/\Delta t$-decay in the liquid limit (bold solid line) is expected from the Einstein-Helfand (EH) relation, Eq. 4.5. Inset: Shear viscosity $\eta(1/H)$ for $T = 0.55$. The values are used in Sec. 4.6 to define a relative scale for $\tau_\alpha(T)$. The line presents a linear fit according to Eq. 1.3.

## 4.5 Plateau modulus $\mu_\mathrm{p}$ and shear viscosity $\eta$

In the main panel of Fig. 4-7, we see that $\mu$ decreases monotonically with $\Delta t$ for a broad range of temperatures (double-logarithmic representation). As already pointed out above (Fig. 1-2), it also decreases continuously with $T$ and no indication of a jump singularity is observed. We emphasize that the same qualitative behavior is found for all systems we have investigated. (Similar plots have been obtained for glass-forming colloids in 2D [63] and for 3D polymers [65].) As one expects, the $\Delta t$-dependence of $\mu$ becomes extremely weak in the solid limit, i.e. a plateau (shoulder) $\mu(\Delta t) \approx \mu_\mathrm{p} = const$ appears for a broad $\Delta t$-window. Since the plateau value $\mu_\mathrm{p}$ depends somewhat on $T$ and on the $\Delta t$-window fitted, it is convenient for the dimensionless scaling plots presented in the next two sections to define $\mu_\mathrm{p}(H) \equiv \mu(T = 0.10, \Delta t = 10^4, H)$. The value for *film1* is indicated by the horizontal dashed line. As may be seen from the inset of Fig. 4-5,

$$\mu_\mathrm{p}(H) \approx 16.1 \, (1 - 0.65/H) \approx 1.85 \mu_\mathrm{g}(H) \tag{4.4}$$

46

in agreement with Eq. 1.3. As emphasized by the bold solid line in the main panel of Fig. 4-7, $\mu(\Delta t)$ decreases inversely with $\Delta t$ in the high-$T$ limit. This is expected from the Einstein or "Einstein-Helfand" (EH) relation, Eq. 2.19, which may be rewritten as

$$\mu(\Delta t) \to 2\eta/\Delta t \text{ for } \Delta t \gg \tau_\alpha \qquad (4.5)$$

with $\eta$ being the shear viscosity and $\tau_\alpha$ the terminal shear stress relaxation time [57, 65]. A technical point must be mentioned here. We remind that $\mu_A = \mu_0$ in the liquid limit implies $\mu(\Delta t) = \mu_1(\Delta t)$. Since the impulsive corrections needed for the calculation of $\mu_A$ (cf. Sec. 3.2) and, hence, of $\mu$ are not sufficiently precise for the logarithmic scale used here, it is for numerically reasons best to simply replace $\mu$ by $\mu_1$ to avoid an artificial curvature of the data for large $\Delta t$. Using the EH relation it is then possible to fit $\eta(T)$ above $T \approx 0.50$. For smaller temperatures this method only allows the estimation of lower bounds. As shown in the inset of Fig. 4-7 for $T = 0.55$, the shear viscosity decreases systematically for thinner films and the linear superposition relation (solid line) describes reasonably all available data. We now show how $\eta(T)$ may be extrapolated to much smaller temperatures by means of the "time-temperature-superposition" (TTS) scaling of $\mu(\Delta t)$.

## 4.6 Time-temperature superposition of $\mu(\Delta t)$

The TTS scaling of $\mu(\Delta t)$ is presented in the main panel of Fig. 4-8 using dimensionless coordinates and a double-logarithmic representation. Data for a broad range of temperatures are given for *film1* (open symbols) while we focus for clarity on one temperature ($T = 0.35$) for the other films (filled symbols) and the 3D bulk ensembles (stars). A good data collapse is achieved by plotting the rescaled shear modulus $y = \mu(\Delta t)/\mu_p$ as a function of the reduced sampling time $x = \Delta t/\tau_\alpha$ using the relaxation time $\tau_\alpha(T)$ indicated in the inset. The scaling function $y = f(x)$ is given by $f(x) \to const \approx 1$ for $x \ll 1$ (dashed horizontal line) and by $f(x) \to 2/x$ for $x \gg 1$ (bold solid line) for consistency with the EH relation. The vertical axis is made dimensionless using the plateau modulus $\mu_p$ introduced in Sec. 4.5. Please note that since according to Eq. 4.4 the $H$-dependence of $\mu_p$ is rather small on the logarithmic scales we are interested in, a similar good data collapse may also be achieved by simply setting $\mu_p = 1$. Much more important is the rescaling of the hori-
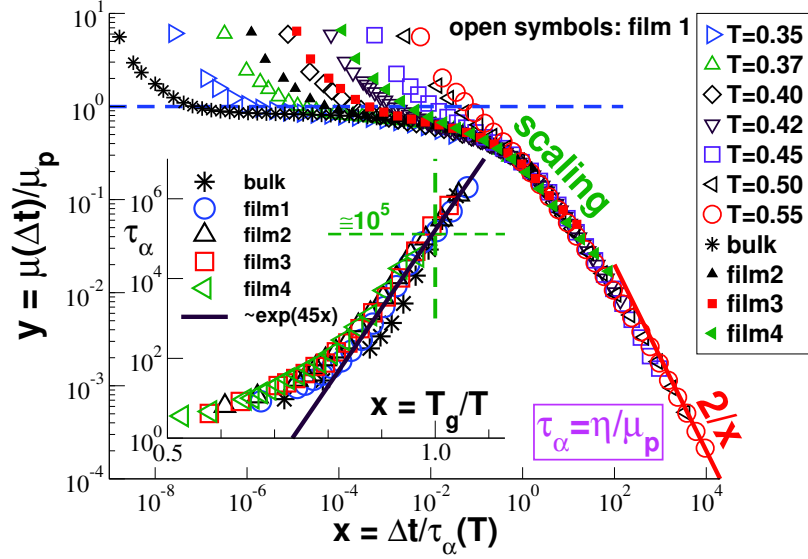
Figure 4-8: TTS scaling for $y = \mu(\Delta t)/\mu_{\mathrm{p}}$ as a function of $x = \Delta t/\tau_\alpha(T)$ with $\mu_{\mathrm{p}}$ being the plateau modulus defined in Sec. 4.5 and $\tau_\alpha(T)$ the relaxation time indicated in the inset. We impose $\tau_\alpha(T = 0.55)$ according to Eq. 4.6 to have an *arbitrary* time scale. The two asymptotics of the scaling function $y = f(x)$ for $x \ll 1$ and $x \gg 1$ are indicated by dashed and solid lines. Note the broad crossover regime between these limits. Inset: Data collapse of terminal relaxation time $\tau_\alpha$ *vs* $x = T_{\mathrm{g}}/T$ for all our ensembles. Arrhenius behavior (bold solid line) is observed around the glass transition ($x \approx 1$).

zontal axis by means of the terminal relaxation time $\tau_\alpha(T, H)$ which depends strongly on both temperature and film thickness. Note that the strong $H$-dependence is masked by the rescaling of the horizontal axis using $x = T_{\mathrm{g}}(H)/T$ in the inset of Fig. 4-8.

Some remarks are in order to explain how the scaling plot was achieved. We have in fact followed in a first step the standard prescription [1, 6] fitting the relative dimensionless factors $a_T$ and $b_T$ for the horizontal and vertical rescaling of $\mu(\Delta t, T)$ for temperatures $T$ close to certain reference temperatures $T_0$. As one may expect [1], $b_T$ can safely be set to unity for the entire temperature range we are interested in. In turn this justifies the temperature independent factor $\mu_{\mathrm{p}}$ used to rescale the vertical axis. Naturally, merely tuning $a_T = \tau_\alpha(T)/\tau_\alpha(T_0)$ only sets the *relative* scale of $\tau_\alpha(T)$. In order to fix the missing prefactor we impose,

$$\tau_\alpha(T) = c\,\eta(T)/\mu_{\mathrm{p}}(H) \text{ with } c = 1 \text{ for } T = T_0 = 0.55 \tag{4.6}$$

using the shear viscosity $\eta$ determined in the high-$T$ limit by means of Eq. 4.5. Due to the

somewhat arbitrary constant $c/\mu_{\mathrm{p}}$ the strongest curvature of the rescaled shear modulus $y(x)$ coincides with $x \approx 1$. (Using instead $c \approx 100$ the crossover to the EH decay would occur at about $x \approx 1$.) Consistency of $\mu(\Delta t) = \mu_{\mathrm{p}} f(x) \approx \mu_{\mathrm{p}} \tau_\alpha / \Delta t$ for $x \gg 1$ and the EH relation, Eq. 4.5, implies interestingly that Eq. 4.6 must hold for all temperatures. In other words, the relaxation time $\tau_\alpha(T)$, shown in the inset of Fig. 4-8, and the shear viscosity $\eta(T)$ are equivalent up to a trivial prefactor. We emphasize that the stated proportionality hinges on the observation that $b_T \approx 1$. As shown in the inset, a remarkable scaling collapse is achieved by plotting $\tau_\alpha$ or $\eta$ as a function of $x = T_{\mathrm{g}}/T$. Especially, this implies that

$$\tau_\alpha(T \approx T_{\mathrm{g}}) = c\ \eta(T \approx T_{\mathrm{g}})/\mu_{\mathrm{p}}(H) \approx 10^5 \qquad (4.7)$$

for all our ensembles as shown by the horizontal and vertical dashed lines. In other words, the dilatometric criterion (Sec. 4.2) and the rheological criterion, fixing a characteristic viscosity for defining $T_{\mathrm{g}}$ [1], are numerically consistent on the logarithmic scales considered here. Anticipating better statistics and longer production runs (improving thus the precision of the TTS scaling), this suggests that Eq. 4.7 may be used in the future to define $T_{\mathrm{g}}$. We finally note that an Arrhenius behavior $\tau_\alpha \sim \exp(45x)$ is observed for $x \approx 1$ (bold solid line) and that for $x \ll 1$ a Vogel-Fulcher-Tammann (VFT) behavior holds (cf. Sec. 5.2) as expected [1].

## 4.7 Shear-stress relaxation modulus $G(t)$

While the (shear strain) creep compliance $J(t)$ [1] of polymer films has been obtained experimentally (by means of a biaxial strain experiment using effectively the reasonable approximation of a time-independent Poisson ratio $\nu$ near $1/2$) [15, 19, 20, 23], this seems not to be the case for the shear-stress relaxation modulus $G(t)$. This could in principle be done by suddenly tilting the frame on which a free-standing film is suspended and by measuring the shear stress $\tau(t)$ needed to keep constant the tilt angle $\gamma$. The direct numerical computation of $G(t)$ by means of an out-of-equilibrium simulation tilting the simulation box in a similar manner, is a feasible procedure in principle as shown in Ref. [43]. However, for general technical reasons [57] this procedure remains tedious.[24] Fortunately,

---

[24]Being limited to the high-frequency limit, it is difficult to get $G(t)$ by Fourier transformation of the storage and loss moduli $G'(\omega)$ and $G''(\omega)$ [1] obtained by applying an oscillatory simple shear [43].
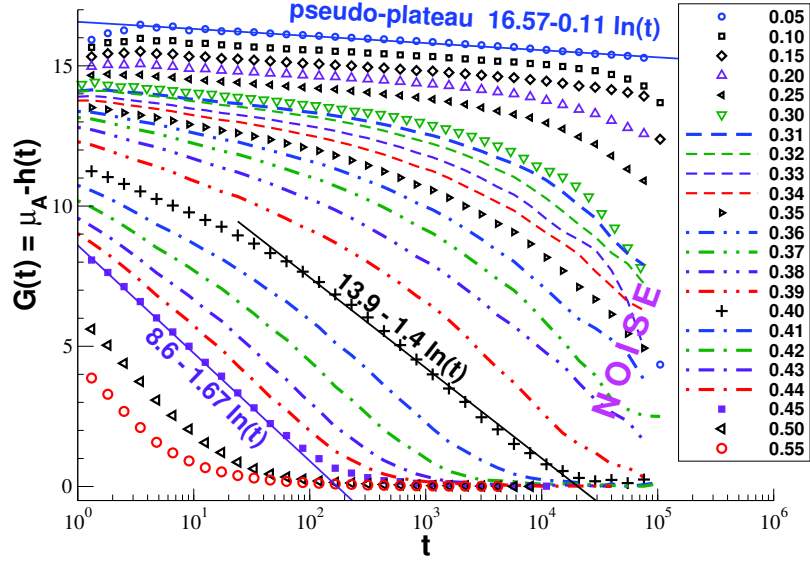
Figure 4-9: Unscaled stress relaxation modulus $G(t)$ for *film1* using half-logarithmic coordinates. $G(t)$ increases continuously with decreasing $T$. For some temperatures above $T_g$ and for very low $T \ll T_g$ a logarithmic creep $G(t) = a - b\log(t)$ is observed (thin solid lines). We shall come back to this logarithmic creep behavior in Sec. 7.4.

$G(t)$ can be computed using the stored time-series of $\hat{\tau}$ and $\hat{\mu}_A$ by means of the appropriate linear-response fluctuation-dissipation relation $G(t) = \mu_A - h(t)$, Eq. 2.50. Note that $G(t=0) = \mu_A$ as it should if an affine strain is applied at $t = 0$.

Focusing on our thickest films and using a half-logarithmic representation, Fig. 4-9 presents $G(t)$ for all temperatures $T \leq 0.45$. Please note that albeit we ensemble-average over $N_c$ independent configurations it was necessary for the clarity of the presentation to use in addition gliding averages over the total production runs, i.e. the statistics becomes worse for $t \to \Delta t_{max} = 10^5$, and, in addition, to strongly bin the data logarithmically. Without this strong averaging the data would appear too noisy for temperatures around $T_g$. (See Sec. 7.2 for a discussion of the standard deviation $\delta G(t)$ of $G(t)$.) However, it is clearly seen that $G(t)$ increases *continuously* with decreasing $T$ without any indication of the suggested jump-singularity [125–129]. This is consistent with the continuous decay of the storage modulus $G'(\omega = const, T)$ as a function of temperature $T$ shown in Fig. 6 of Ref. [43]. Similar continuous behavior has also been reported for the Young modulus of polymer films [44].

Using a similar double-logarithmic representation as in Fig. 4-8, we demonstrate in Fig. 4-10 that a successful TTS scaling can be achieved for $G(t)$ just as for $\mu(\Delta t)$. While
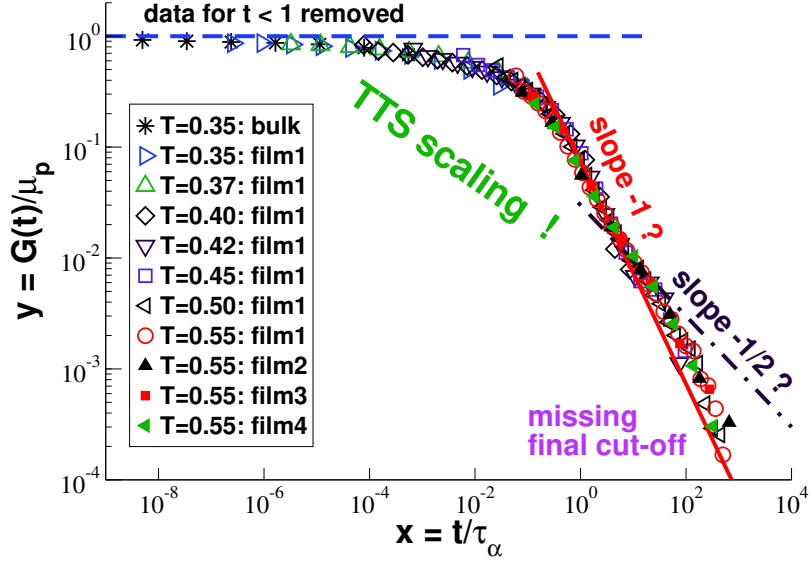
50

Figure 4-10: Successful TTS scaling plot of $y = G(t)/\mu_p$ as a function of reduced time $x = t/\tau_\alpha$ using the same relaxation times as in Fig. 4-8. The two indicated power laws (bold and dash-dotted lines) are given for comparison. Unfortunately, our production runs are too short to reveal the expected final exponential cut-off even for the highest temperatures.

several temperatures are again indicated for *film1*, only one temperature is indicated for the other ensembles. The effective power law $-1$ seen for $x \approx 1$ (solid line) can of course not correspond to the asymptotic long-time behavior since the viscosity $\eta$ and the terminal relaxation $\tau_\alpha = \tau_{\alpha,1}$ given according to Eq. 2.23 by the moments [1]

$$m_0 \equiv \int_0^\infty \mathrm{d}t \; G(t) = \eta \text{ and } m_1 \equiv \int_0^\infty \mathrm{d}t \; t \; G(t) = J_e^0 \eta^2 = \tau_{\alpha,1}\eta \qquad (4.8)$$

must then diverge. We remind that the Rouse behavior (Appendix C) corresponds to a cut-off with $y(x) \approx \exp(-x)/\sqrt{x}$ [3, 6] for which all moments of $G(t)$ converge. Basically, due to the inaccessible final cut-off it is impossible for any temperature $T \leq 0.55$ to determine $\eta$ and $\tau_\alpha$ merely by integrating $G(t)$ as in Eq. 4.8. Due to this reason we proceeded here using the EH relation and the TTS scaling to estimate $\eta$ and $\tau_\alpha$.[25] The unfortunate intermediate effective power-law slope $-1$ is mainly due to the shortness of our chains as seen in Appendix C for the Rouse model of short chains (Fig. C-1a). Additionally, the local glassy dynamics and the polymer dynamics are clearly not separated. Longer production runs are warranted to clarify this issue.

---

[25] As shown in Sec. 5.2 to obtain the shear viscosity $\eta$ from the Green-Kubo (GK) relation one needs to investigate the time dependent viscosity $\eta(t)$, Eq. 2.18.
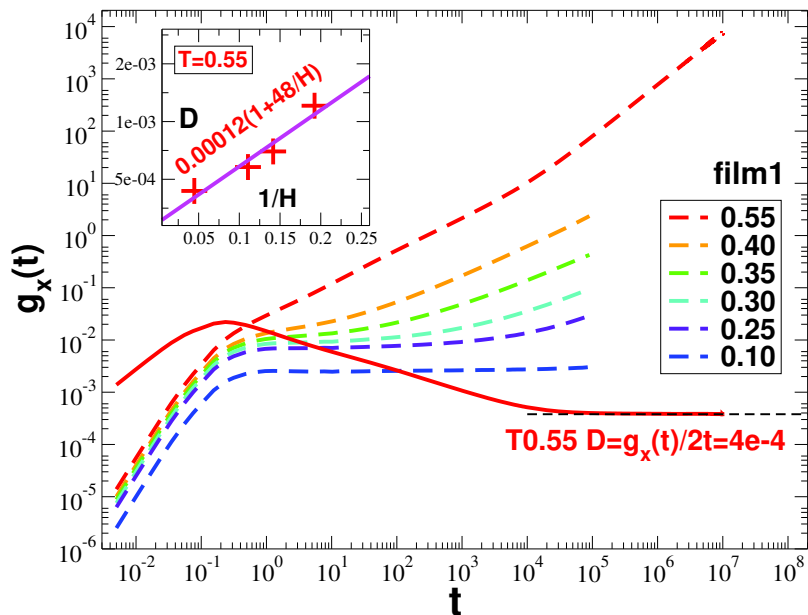
Figure 4-11: Monomer mean-square displacement (MSD) $g_x(t)$ along the $x$-axis for *film1* for various temperatures (dashed lines). $g_x(t)/2t$ (solid line) is seen to converge to a diffusion constant $D \approx 0.0004$ for the highest temperature $T = 0.55$. Inset: Comparison of the diffusion coefficients $D$ for $T = 0.55$ for our four films demonstrating $D \propto 1/H$ (solid line).

## 4.8 Monomer mean square displacement

Up to now we have only considered static and quasi-static properties and the response function $G(t)$. It was shown that that thinner films appear to be softer in agreement with a two layer model with (more) fluid surfaces and a more rigid bulk in the center of the films. We verify now whether this idea also holds for a simple straightforward dynamical property, the monomer mean-square displacement (MSD) averaged over all monomers of the film [3, 6]. As shown in Fig. 4-11 we focus on the MSD $g_x(t)$ along the $x$-axis of the films. As can be seen by the dashed lines in the main panel for *film1*, $g_x(t)$ systematically decreases upon lowering the temperature. While for high temperatures $g_x(t) \to 2Dt$ in the large time limit for $t \gg \tau_\alpha$, a plateau (shoulder) appears below $T \approx 0.30$ when the monomers get confined within "local cages" [106]. That we are able to easily extract the diffusion constant $D$ in the free-diffusion limit for high temperatures is shown by the solid line for $T = 0.55$.[26]  As shown in the inset of Fig. 4-11 for one temperature ($T = 0.55$) we have compared the diffusion coefficients of the different films. Using linear coordinates

---

[26]Naturally, the determination of $D$ becomes increasingly difficult if one approaches the glass transition, but an upper bound for $D$ can still be estimated.

we trace $D(T)$ as a function of the inverse film thickness $H(T)$. In agreement with other findings presented in this chapter, especially the relaxation time $\tau_\alpha(T)$ and the viscosity $\eta(T)$, it is seen that the the general linear superposition assumption, Eq. 1.3, again holds as emphasized by the solid line.

## 4.9 Major results

As suggested from a large number of experimental and computational studies, many (intensive) properties, such as $T_g$, $\mu$ or $g_x(t)$, were shown to depend linearly on the inverse film thickness $H$ [68]. This agrees with the two-layer model [49, 56] assumption that we made in the Introduction, Eq. 1.3. Building up on our methods applied to 3D polymer melts [65, 66], we observed that $\mu(T)$ decays continuously for our free standing films. As emphasized in Sec. 4.3, $\mu$ systematically depends on $\Delta t$, i.e. larger $\Delta t$ implies a sharper glass transition at smaller temperatures. In addition it is seen in the main panel of Fig. 1-2 that $\mu$ becomes finite at lower temperatures for thinner films. The sampling time $\Delta t$ dependence of $\mu$ can be traced back to the stationarity relation in Eq. 1.2 [57, 66]. We demonstrated in Sec. 4.6 that time translational invariance is applicable for general viscoelastic fluids and that it fits our model systems perfectly. Using the accurate TTS scaling of $\mu$ (Fig. 4-8) we are able to estimate $\eta(T) \sim \tau_\alpha(T)$ for an even broader temperature range down to around $T_g$. The TTS scaling of $G(t)$ is then possible (Fig. 4-10) using the same rescaling parameters.

This page intentionally left blank.

# Chapter 5

# Various rheological properties and comparison to experiments

## 5.1 Introduction

Assuming linear response, we calculated in Ch. 4 $\mu(\Delta t)$ and $G(t)$ for our polymer films. Using these quantities and the TTS scaling, we obtained for $T > T_{\mathrm{g}}(H)$ the absolute values of the shear viscosity $\eta(T, H)$ and the relative scale of the terminal relaxation time $\tau_\alpha(T, H)$. As shown in Fig. 4-10 the problem with the latter quantity is that our $G(t)$-data does not allow, even for the highest temperatures, its direct determination using the moments $m_k$ of $G(t)$ for $k \geq 1$ according to Eq. 2.23 [1, 6]. In Sec. 5.2 we discuss first the shear viscosity $\eta$ comparing values obtained by different techniques. We turn then in Sec. 5.3 to the calculation of the storage and loss moduli $G'(\omega)$ and $G''(\omega)$. An attempt is made to estimate the steady-state creep compliance $J_{\mathrm{e}}^0$ in the high temperature limit and thus using $\tau_{\alpha,1} = J_{\mathrm{e}}^0 \eta$ to give an absolute scale for the relaxation time $\tau_\alpha$. In addition, we compare our data with real experiments. This is done for the glass transition temperature $T_{\mathrm{g}}(H)$ in Sec. 5.5 and for the creep compliance $J(t)$ in Sec. 5.6. A summary is given in Sec. 5.7.
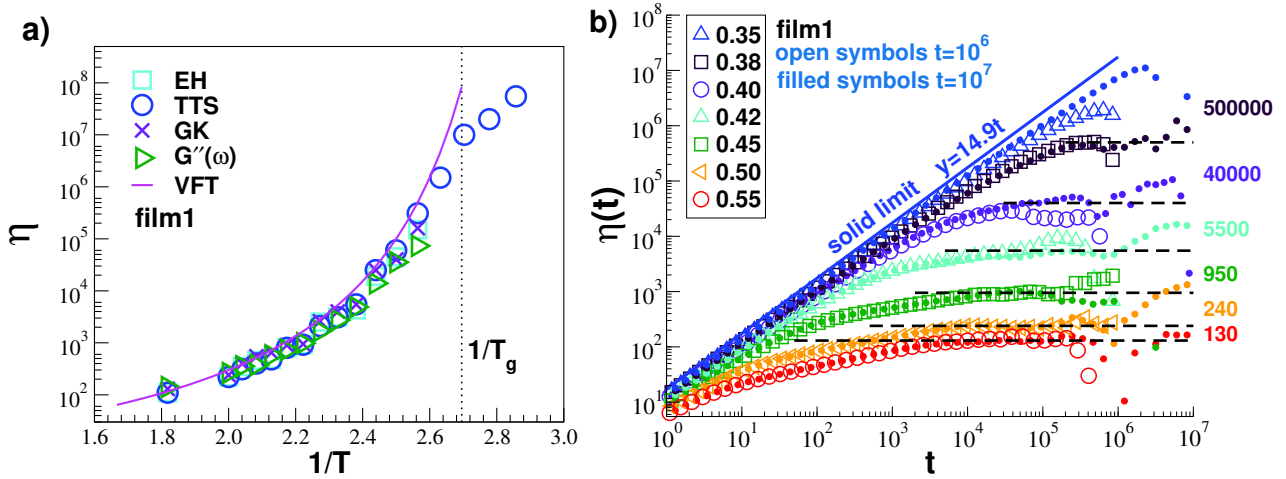
Figure 5-1: Shear viscosity $\eta$ for *film1* for different temperatures $T$: **(a)** Comparison of $\eta$ obtained by means of the EH relation, the TTS scaling, the GK relation and the low-$\omega$ limit of $G''(\omega)$. The data is plotted *vs* the inverse temperature using a half-logarithmic representation. The line indicates a Vogel-Fulcher-Tammann fit according to Eq. 5.2. **(b)** Dynamic shear viscosity $\eta(t)$ calculated using Eq. 5.1 for *film1* ($T_g = 0.37$). We compare the results obtained for two sampling runs, $t = 10^6$ (open symbols) and $t = 10^7$ (filled symbols). A reasonable estimate of $\eta$ (dashed lines) can only be obtained for large $T$.

## 5.2 Shear viscosity

The shear viscosity $\eta$ measures the resistance of a viscoelastic fluid to an imposed shear rate $\dot{\gamma}$ [1, 4, 6]. Panel (a) of Fig. 5-1 presents a summary of the shear viscosities obtained by different methods for *film1*. Importantly, a good agreement between all methods is observed, down to around the glass transition temperature $T_g$. The data obtained using the EH relation and the TTS scaling have already been discussed in, respectively, Sec. 4.5 and Sec. 4.6. As expected [1, 4, 6], the TTS scaling allows a reliable estimation of $\eta$ over a much broader range of temperatures than all other methods. We also include viscosities obtained using the GK relation, Eq. 2.18, and from the low-frequency limit of the loss modulus $G''(\omega) \approx \eta\omega$ described in more detail below in Sec. 5.3.[27] The use of the GK relation is illustrated in panel (b) of Fig. 5-1 where we plot the "dynamical viscosity"

$$\eta(t) \equiv m_{k=0}(t) \equiv \int_0^t \mathrm{d}s \ G(s) \approx \int_0^t \mathrm{d}s \ c(s) \tag{5.1}$$

---

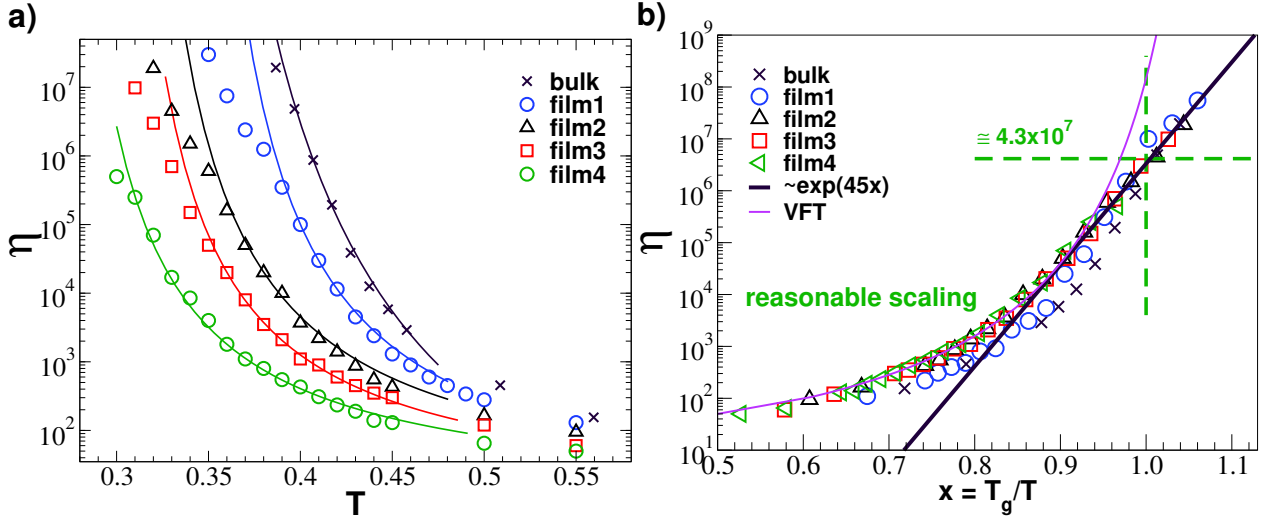[27]Appendix D.3 demonstrates this method for the Rouse model [1, 6].

Figure 5-2: Scaling of $\eta$ focusing on data obtained from the TTS of $\mu(\Delta t)$ for all films and the bulk system: **(a)** Vogel-Fulcher-Tammann (VFT) fits (continuous lines) for $\eta$ as a function of $T$. **(b)** Scaling of $\eta$ as a function of $x = T_{\mathrm{g}}/T$.

for a broad range of temperatures. As already stated in Sec. 2.4.3, the GK method, using a first integral over $G(t)$ is expected to have poorer statistics than the EH method, computed by means of a second integral over $G(t)$, Eq. 2.19. For sufficiently long times $t \gg \tau_\alpha$, the dynamical viscosity $\eta(t)$ must reach a plateau value, the viscosity $\eta$, as indicated by the dashed horizontal lines for the higher temperatures. These values are included in panel (a). Since the relaxation function $G(t)$ becomes increasingly constant, $G(t) \approx \mu_{\mathrm{p}}$, for $T \to T_{\mathrm{g}}$, one naturally observes a linear increase with $\eta(t) \approx \mu_{\mathrm{p}} t$ in this limit.

We analyze now in Fig. 5-2 the scaling of $\eta$ focusing on the data obtained using the TTS scaling. Using half-logarithmic coordinates panel (a) presents $\eta$ as a function of the (unscaled) temperature $T$ and panel (b) as a function of the reduced inverse temperature $x = T_{\mathrm{g}}/T$. The thin solid lines in panel (a) and panel (b) demonstrate that our film data are consistent with the Vogel-Fulcher-Tammann (VFT) law [1]

$$\eta(T, H) = \eta_\infty \cdot \exp\left(\frac{B}{T - T_\infty(H)}\right) \tag{5.2}$$

in the high temperature limit with $T_\infty(H)$ being the Vogel temperature [1].[28] Consistently with the inset of Fig. 4-8, the data presented in panel (b) scales and an Arrhenius behavior

---

[28]We have fitted for $T_\infty(H)$ with the WLF scaling approach using several reference temperatures $T_0$. The fit values of $T_\infty(H)$ are, as expected, slightly smaller than $T_{\mathrm{g}}$ [1] and scale again according the linear-superposition relation Eq. 1.3.
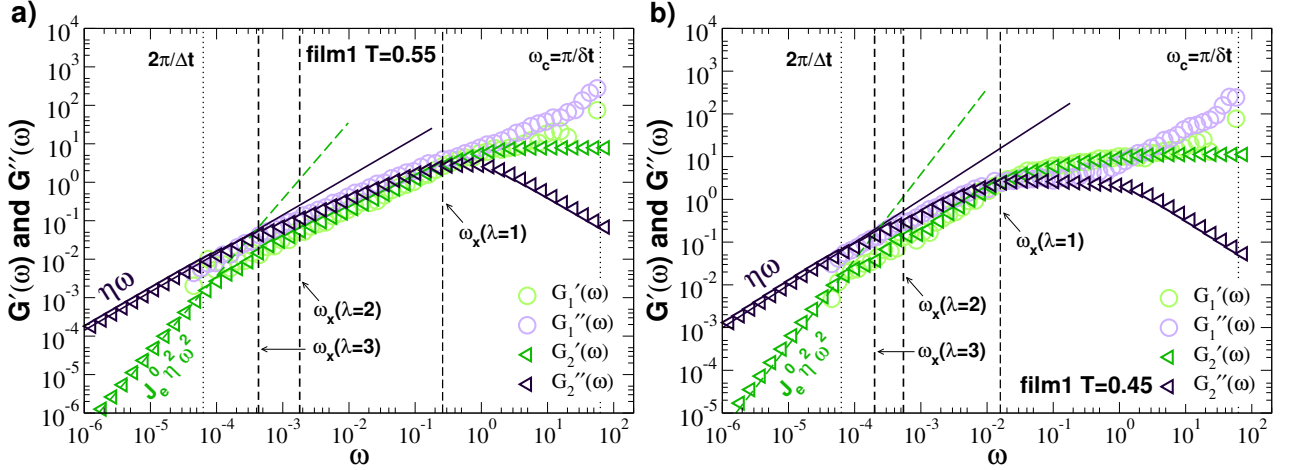
Figure 5-3: $G'(\omega)$ and $G''(\omega)$ obtained using the FFT and SMD methods from the $G(t)$-data for two high temperatures for *film1*: **(a)** $T = 0.55$ where $\eta \approx 141$, $J_e^0 \approx 18.5$ and $\tau_{\alpha,1} \approx 2604$ and **(b)** $T = 0.45$ where $\eta \approx 986$, $J_e^0 \approx 4$ and $\tau_{\alpha,1} \approx 3944$. The crossing frequencies $\omega_\times(\lambda) = 1/\tau_\times(\lambda)$ for the ratios $\lambda = 1$, $\lambda = 2$, and $\lambda = 3$ are indicated by dashed vertical lines. Note that $\omega_\times(\lambda = 3)$ corresponds nicely to the crossing frequency $1/\tau_{\alpha,1}$ of the two low-$\omega$ asymptotes for $G'(\omega)$ and $G''(\omega)$ for all temperatures $T \gg T_g$.

with $\eta \sim \exp(45x)$ is observed for $x \approx 1$ (bold solid line).

## 5.3  Complex modulus of polymer films

In this section, we perform the numerical transformation [1, 130, 131] of $G(t)$ calculated for *film1* to the corresponding complex modulus $G^\star(\omega) = G'(\omega) + iG''(\omega)$ by means of Eq. 2.20 and Eq. 2.21. This can be done using the Spectral Mode Decomposition (SMD) method [1] and the Fast Fourier Transformation (FFT) [111]. Details and analytical tests for these methods are provided in Appendix D.2 and Appendix D.3. In the following, we use the notations $G'_1(\omega)$ and $G''_1(\omega)$ for FFT and $G'_2(\omega)$ and $G''_2(\omega)$ for SMD.

We focus on the high temperature limit well above the glass transition. $G'(\omega)$ and $G''(\omega)$ are shown in Fig. 5-3 for *film1* $T = 0.55$ and $T = 0.45$. As discussed in Appendix D.3, FFT data is only available in a frequency window between $2\pi/\Delta t$ (marked by the left vertical dotted lines) and the Nyquist critical frequency $\omega_c = \pi/\delta t$ (marked by the vertical dotted lines on the right-hand sides of both panels) while the SMD method allows (with some care) the extrapolation to a broader frequency regime. In agreement with Appendix C and Appendix D.3 three main frequency regimes can be distinguished. We focus here on

58

the low-$\omega$ limit[29] where the SMD data exhibit the expected asymptotic behavior, Eq. 2.22, emphasized by dashed lines for $G'(\omega)$ and by solid lines for $G''(\omega)$. (Much larger production times are required to show this limit directly with the FFT method.) As noted in the caption of Fig. 5-3, viscosities $\eta$ may be obtained from the linear $\omega$-dependence of $G''(\omega)$. These values, also indicated in Fig. 5-1, compare well with $\eta$ from other methods. Using these $\eta$ we determine in turn the steady-state creep compliances $J_e^0$ from the limit $G'(\omega) \to J_e^0 \eta^2 \omega^2$. (The latter limit is less reliable since $G'(\omega) \ll G''(\omega)$ in this regime.) Importantly, using $\eta$ and $J_e^0$ this implies the indicated terminal relaxation times $\tau_{\alpha,1} = J_e^0 \eta$ corresponding to the crossing of the two low-$\omega$ asymptotes (Sec. 2.4.5). We thus obtain by setting

$$\tau_\alpha \stackrel{!}{=} \tau_{\alpha,1} \text{ for } T = 0.55 \tag{5.3}$$

for the highest temperature with the most reliable data an *absolute scale* for the terminal relaxation times $\tau_\alpha(T)$ obtained in Sec. 4.6 from the directly measured viscosities and the TTS scaling. This finally fixes the coefficient $c$ introduced in Eq. 4.6 as

$$c = J_e^0(T = 0.55) \, \mu_p(H) \approx 286. \tag{5.4}$$

Unfortunately, $J_e^0$ is not very precise even for $T = 0.55$ due to the extrapolation of $G'(\omega)$ with the SMD method. It would thus be nice to have an independent means to characterize the terminal relaxation time for other temperatures using the more restricted FFT data for $\omega \gg 2\pi/\Delta t$ without using the asymptotic low-$\omega$ behavior. As shown by the dashed vertical lines in Fig. 5-3 we attempt this by determining the crossover frequency $\omega_\times(\lambda)$ as defined by Eq. 2.24 marking the (first) crossing of $\lambda G'(\omega)$ and $G''(\omega)$. We use the values $\lambda = 1$, 2 and 3. As can be seen this corresponds to frequencies $\omega_\times(\lambda)$ where similar values of $G'(\omega)$ and $G''(\omega)$ have be obtained with *both* methods to a reasonably good precision. As can be seen $\omega_\times(\lambda) = 1/\tau_\times(\lambda)$ systematically decreases with increasing $\lambda$. As discussed in Appendix C $\omega_\times(\lambda = 2) \approx 1/\tau_{\alpha,1}$ for the Rouse model. This suggests to use a $\lambda$ larger unity. Consistently, we find empirically that $\tau_\times(\lambda \approx 3) \approx \tau_{\alpha,1}$ for the highest temperatures. Moreover, after rescaling with the constant $c$ of Eq. 5.4 the terminal relaxation times $\tau_\alpha$

---

[29]In addition there is an intermediate frequency regime where $G'(\omega)$ and $G''(\omega)$ are similar and a high-frequency regime corresponding to times smaller that the local monomer relaxation time where $G'(\omega)$ becomes constant and $G''(\omega) \propto 1/\omega$ for the SMD method and where the FFT method becomes inaccurate.

obtained by means of the TTS scaling, Fig. 4-8, we obtain that $\tau_\times(\lambda = 3) \approx \tau_\alpha$ holds for all temperatures above the glass transition (not shown). Albeit the value $\lambda = 3$ may be specific for our numerical system, we believe that this procedure might be generally useful.

## 5.4   Comparison with the nanobubble inflation method

Experimentally, only a few methods have attempted to directly measure the creep compliance of freestanding polymer films [19, 132]. Of particular interest is the novel nanobubble inflation method developed by O'Connell and McKenna [19] for the measurement of viscoelastic properties of freestanding polymer films and associated developments [15, 132]. In brief, the nanobubble inflation experiment characterizes thin films that are subjected to constant pressure from below via nanometer sized perforations, causing the formation and growth of bubbles that creep with time. Using interferometry [132] or near-contact AFM method [19], measurements of the bubble profile as a function of time are taken. The biaxial compliance $D(t)$ of the material is then calculated by measuring the time-dependent strain as a function of constant stress. In this method, the radius of curvature of the bubble changes as it grows, and the stress acting on the bubble is not kept a constant. The above experiment is interesting for us since it characterizes the mechanical properties of freestanding polystyrene (PS) thin films. Furthermore, our bead-spring model has historically shown good correspondence with experimental studies of PS films [53, 60, 61].

Interestingly, a different protocol for analyzing the data was developed in Ref. [19]. From the set of creep compliance curves measured at different temperatures and a given thickness, a TTS mastercurve can be obtained along with its horizontal shift factors $a_\mathrm{T}$. These shift factors can be fit to a VFT (or equivalently WLF) law. The change in $T_\mathrm{g}$ of a film from the $T_\mathrm{g}$ of the bulk, $\Delta T_\mathrm{g} = T_\mathrm{g} - T_\mathrm{g}{}^B$, can be calculated as the shift in the VFT curves from that of the thickest sample.[30] This can be repeated for all thicknesses to get $\Delta T_\mathrm{g}$ as a function of film thickness [19]. This study also matches with our finding concerning the reduction in $T_\mathrm{g}$ with decreasing $H$ [11, 16, 18, 19, 76, 133].
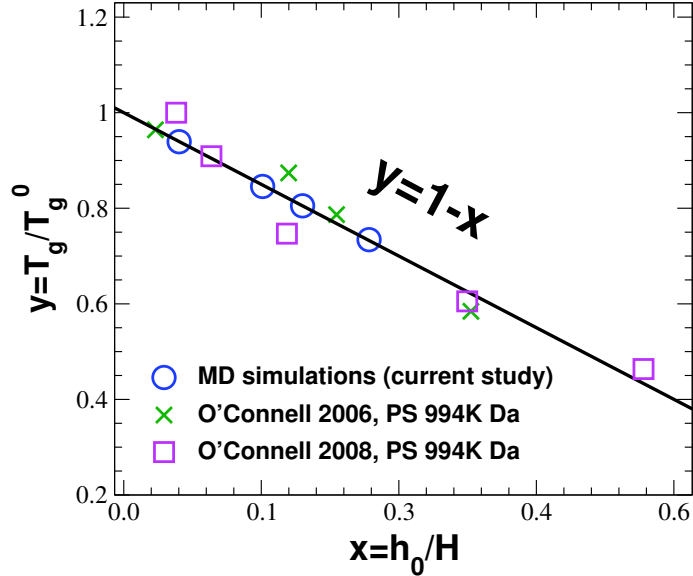
Figure 5-4: Collapse of $T_{\mathrm{g}}/T_{\mathrm{g}}^{\mathrm{B}}$ vs $h_0/H$ comparing our simulation data (circles) with experimental data from Ref. [19] (O'Connell 2008) and Ref. [18] (O'Connell 2006). The simulation data for $H$ and $T_{\mathrm{g}}$ are summarized in Table 3.1. $h_0$ is a system-dependent length scale needed to collapse the data. We have set $h_0 = 1.28$ for our simulations and $h_0 = 7.2nm$ (O'Connell 2006) and $h_0 = 6.4nm$ (O'Connell 2008) for the experimental systems. The solid line indicates Eq. 1.3. The experimental data were kindly provided by C. Roth.

## 5.5 Glass transition temperature $T_{\mathrm{g}}(H)$ revisited

In Fig. 5-4, we compare the glass transition temperature obtained for our freestanding films with the data reported in Refs. [18, 19]. We plot here the reduced glass transition temperature $y = T_{\mathrm{g}}/T_{\mathrm{g}}^{\mathrm{B}}$ as a function of the rescaled inverse film thickness $x = h_0/H$. This confirms that both the experimental and the numerical data follow the relation [36, 71, 74]

$$y = T_{\mathrm{g}}/T_{\mathrm{g}}^{\mathrm{B}} = 1 - h_0/H = 1 - x \tag{5.5}$$

implied by the two-layer model, Eq. 1.3. The system-depending length $h_0$ allows to collapse all data onto $y = 1 - x$ (solid line). Specifically, we fitted $h_0 = 1.28$ for the numerical data, $h_0 = 7.2nm$ for the experimental data of Ref. [18] and $h_0 = 6.5$ nm for the data from Ref. [19]. Note that the thinnest PS film (11nm) studied in Ref. [19] is similar in thickness to our thickest film (*film1*, $H_g = 21.3$ LJ units) when converted to physical units. We have made here the following choices for an approximate conversion from LJ to physical units

---

[30]The thickest sample ($H = 112nm$) is assumed to show bulk behavior in this case.
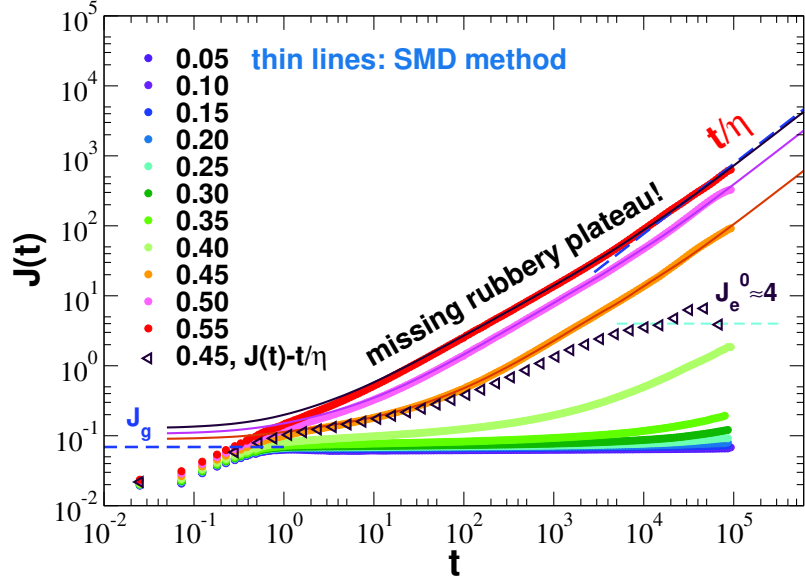
Figure 5-5: $J(t)$ calculated using the HH (dots) and SMD (lines) methods for various temperatures. For high-$T$, it is also seen that the system reaches *flow* and $\eta = 130$ for $T = 0.55$ is observed in the long time limit. As seen from the open triangles the same steady-state creep compliance $J_e^0 \approx 4$ for $T = 0.45$ is obtained as in Sec. 5.3.

[25]: $\sigma_{\mathrm{LJ}} = 5 \cdot 10^{-10}$m, $\epsilon_{\mathrm{LJ}}/k_{\mathrm{B}} = 450$K, and $\tau_{\mathrm{LJ}} = 2 \cdot 10^{-12}$s, we get for our *film1*, a thickness of $\approx 10.65$nm.

## 5.6   Creep compliance of polymer films

The creep compliance for our films can be obtained via two routes: *(short route)* Direct application of the HH transformation to $G(t)$ (Sec. D.4) and *(long route)* conversion of the complex modulus obtained by FFT/SMD to the complex compliance ($J'(\omega)$ and $J''(\omega)$ in Eq. C.7) and then calculating the $J(t)$ [1]. In Fig. 5-5, we compare the two approaches. It can be seen that there is good correspondence between the two methods especially in the high-$T$ limit. In this limit, $J(t)$ reaches *flow* without any sign of rubbery plateau. The terminal slope corresponds to the shear viscosity $\eta = 130$ calculated from the EH relation for $T = 0.55$ verifies the validity of both methods. The steady-state creep compliance $J_e^0 \approx 4$ for $T = 0.45$ is observed yet again by taking the limiting value of $J(t) - t/\eta$ [1] with $\eta = 986$ (open triangles). This is in agreement with the result from panel (b) of Fig. 5-3. The more direct HH method is able to calculate the $J(t)$ for low-$T$ as well. In addition, it also captures the short-time dynamics corresponding to the crossover from microscopic
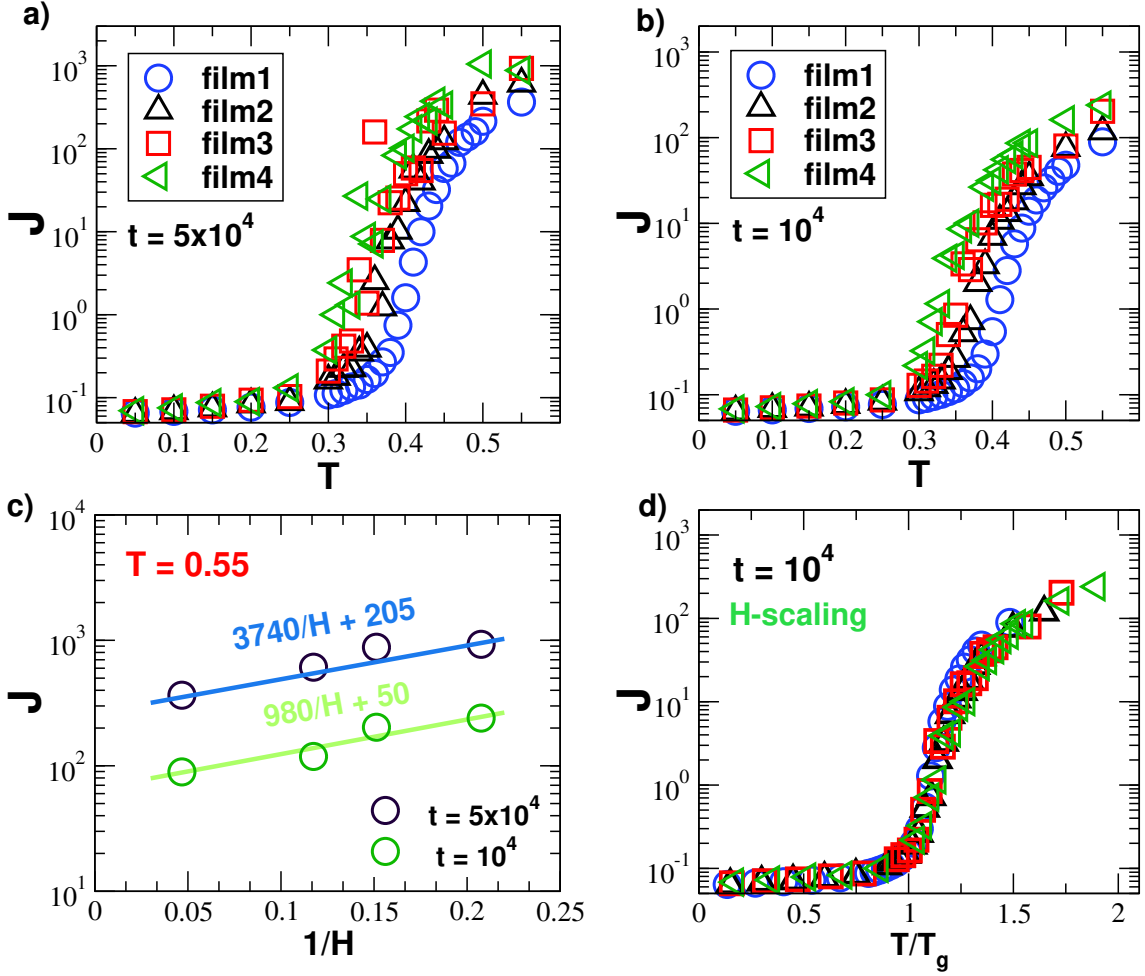
Figure 5-6: The creep compliance $J(t)$ sampled at different times **(a)** $t = 5 \times 10^4$ and **(b)** $t = 10^4$ **(c)** Thickness dependence of $J(t)$ also given for two different $t$ as indicated in the figure. **(d)** Scaling plot for all films obtained by setting the horizontal axis $x = T/T_{\mathrm{g}}$.

dynamics to glassy plateau.

From the time series of $J(t)$, we can extract for two arbitrarily chosen times, $t = 5 \times 10^4$ and $t = 10^5$, the creep compliance as a function of temperature and film thickness (Fig. 5-6(a-b)). The resulting plots can be interpreted by assuming a simple Maxwell model, $J(t) = J_{\mathrm{g}} + t/\eta$. Here, it is readily seen that the elastic and viscous parts are additive. We also verified in Fig. 5-5 for high-$T$ that our data corresponds to the long time behavior $J(t) \to t/\eta$ predicted by the Maxwell model. In Fig. 5-6(a-b), for low-$T$, the creep compliance is very small, and of the order $J_{\mathrm{g}} \approx 1/\mu_{\mathrm{p}}(H)$. Due to high viscosity, $1/\eta(H)$ term is negligible relative to $1/\mu_{\mathrm{p}}(H)$ in this limit. In the (liquid) high-$T$ limit, the reverse scenario occurs $1/\eta(H) \gg 1/\mu_{\mathrm{p}}(H)$. It is also clear from Fig. 5-6(c) that there
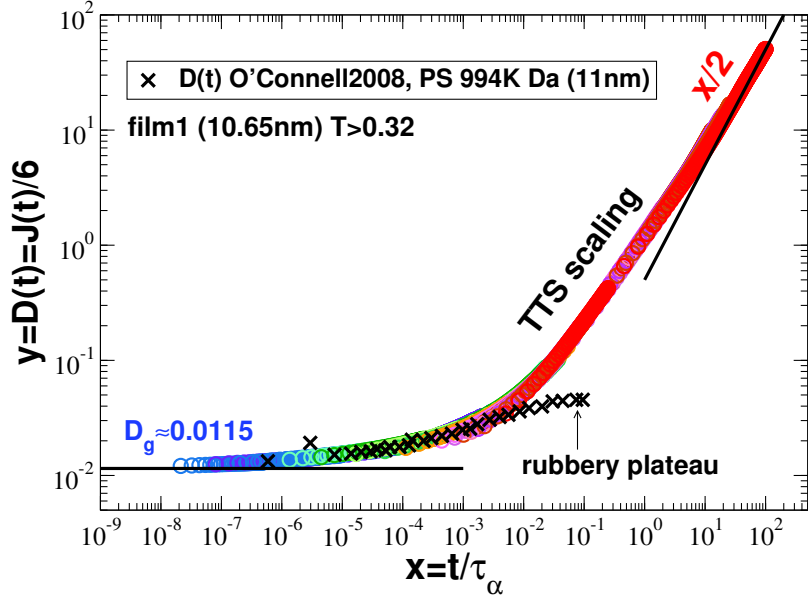
63

Figure 5-7: TTS of the the bi-axial compliance $D(t) = J(t)/6$ obtained from our simulations for $T > 0.32$, superimposed with the results from the nanobubble inflation method (crosses) [19]. Data points below $t < 1$ were removed. In the short-time limit $D_g \approx 1/6\mu_p \approx 0.0115$ is observed.

is a $H$-dependency for our $J(t)$ seen to increase with the inverse thickness $1/H$. This is consistent with the $H$-dependence of our viscosities, Sec. 5.2, and experimental studies [17–19, 53, 56, 91]. The creep compliances for all our films can also be brought to scale by setting $x = T/T_g$ as shown in Fig. 5-6(d).

We will be focusing solely on the $J(t)$ calculated from the HH method for our experimental comparisons. As a reminder, the experiment mentioned in Sec. 5.4 measures the bi-axial compliance, $D(t)$, of a freestanding PS film. For comparison with the experiment, we have to convert our $J(t)$ to $D(t)$ by applying the constitutive equations of linear elasticity. By assuming a Poisson ratio $\nu = 0.5$ for isotropic systems, we have $D(t) = J(t)/6$ [134]. By setting $x = t/\tau_\alpha$, we obtain the scaling of $D(t)$ for all $T > 0.32$ as shown in Fig. 5-7. We also see that a good approximation of the glass-like compliance $D_g \approx J_g/6 \approx 1/6\mu_p \approx 0.0115$ is obtained for very short times. We then shift the $D(t)$ reported in Ref. [19] on top our curves using shift factors $(x, y) = (6.184 \cdot 10^{-8}, 2.256 \cdot 10^8)$. We are able to demonstrate that in the glassy regime (short times), the simulation and experiments superimpose perfectly. As for the viscoelastic regime (intermediate-long time limit), it is seen that they diverge as our films do not exhibit any *rubbery plateau*. Instead, our films reach the flow regime

(for high-$T$). The missing plateau can be attributed to the absence of chain entanglements, which can greatly affect the polymer dynamics [62, 121, 122]. Unfortunately for us the chain length of $N = 16$ is too short to observe this phenomenon $N \ll N_e \approx 100$.

## 5.7 Major results

We compared in Sec. 5.2 the shear viscosities $\eta$ calculated using different methods and demonstrated that these data are consistent with the Vogel-Fulcher-Tammann (VFT) law. We presented in Sec. 5.3 the storage and loss moduli $G'(\omega)$ and $G''(\omega)$ from which we obtained $\eta$ and $J_e^0$ and thus $\tau_{\alpha,1} = J_e^0 \eta$ in the high temperature limit. This allowed us to determine an absolute scale for the terminal relaxation time $\tau_\alpha$, Eq. 5.3. We suggested that the crossing time $\tau_\times (\lambda \approx 3)$ may be a numerically interesting alternative for the determination of $\tau_\alpha$. Rheological properties of freestanding films have been widely studied through experiments and it was of significance for us to compare the experimental results with our *computational experiments*. As shown in Fig. 5-4 the experimental and the computational data for the glass transition temperatures $T_g(H)$ can be collapsed on one mastercurve consistent with the linear superposition, Eq. 1.3. We transformed in Sec. 5.6 $G(t)$ to $J(t)$ and compared these $J(t)$-data with the shifted experimental data obtained from Ref. [19]. As expected for our too short chains ($N \ll N_e$) no rubbery plateau is observed for our data.

This page intentionally left blank.

# Chapter 6

# Layer resolved film properties

## 6.1 Introduction

We have seen in the previous chapters that our films follow an experimentally validated trend of decrease in the apparent glass transition temperature $T_g$ with decreasing $H$ [11, 16, 56, 76, 133]. Although this behavior is not universal [15, 17, 18, 135], it has been proposed that the $H$-dependence may arise from the presence of a liquid-like (soft) surface [15, 19, 22, 56, 76]. Layer models assuming the coexistence of interfacial layers and an inner layer with distinct mobilities are an often invoked interpretation for the relaxation of general confined glass-forming liquids [9, 13, 14, 24, 26]. Experimental techniques focusing on the characterization of $T_g$ at different depths within freestanding PS films using florescence have provided enough evidence on the reduction of $T_g$ at the free interface (and as a function of $H$) [22, 76, 136]. Moreover, many other intensive properties, such as $\mu_A$, $\mu_F$ and thus $\mu$, have been seen in Ch. 4 to depend nontrivially on $H$. To understand these findings we have to take a closer look at the (linear-additive) local contributions of $\mu_A(z)$, $\mu_F(z)$ and $\mu(z)$. This will allow us to verify the presence of bulk values $\mu_{A0} = \mu_A(z \approx 0)$, $\mu_{F0} = \mu_F(z \approx 0)$ and $\mu_0 = \mu(z \approx 0)$ in the middle of the film which are to leading order *independent* of $H$ as implied by the linear superposition relation, Eq. 1.3. In this chapter, we will first describe simple layer resolved properties (density in Sec. 6.2, energies in Sec. 6.3, stresses in Sec. 6.4). We will then discuss the distributions $\mu_A(z)$ and $\mu_F(z)$ in Sec. 6.5 and Sec. 6.6 that contribute to the (linear-additive) local shear-stress modulus $\mu(z)$ (Sec. 6.7). We summarize our results in Sec. 6.8.
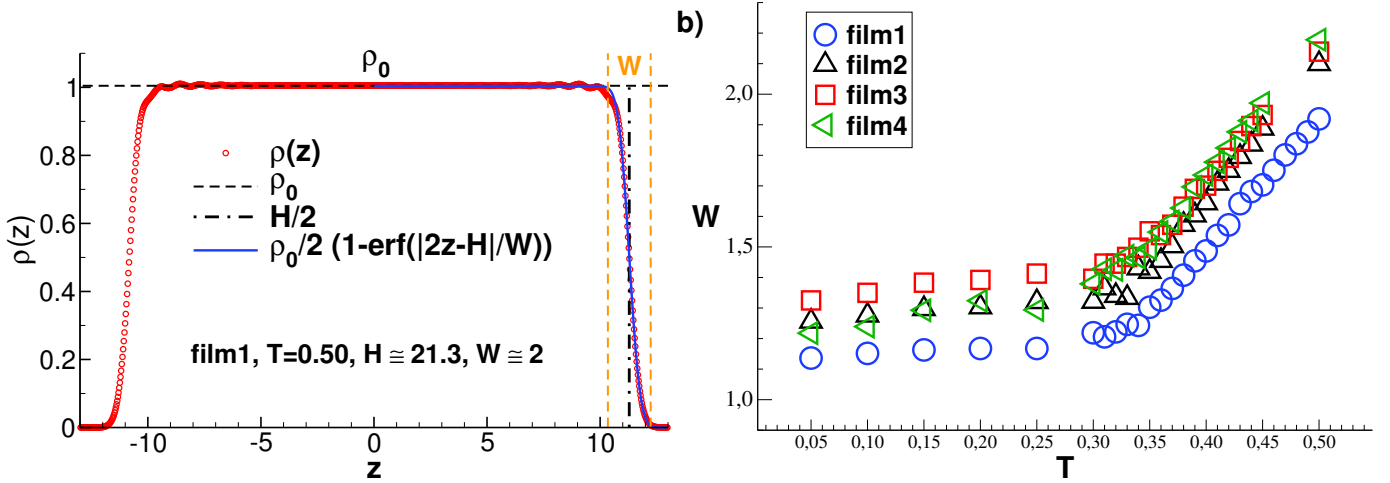
Figure 6-1: **(a)** Density profile $\rho(z)$ for *film1* at $T = 0.50$. The film thickness $H \equiv NM/\rho_0 L^2$ may be obtained from the midplane density $\rho_0$ (horizontal dashed line). Similar values are obtained by fitting the mean-field prediction given by the solid line [124]. **(b)** Interface width $W(T)$ for different $L$.

## 6.2 Density profile $\rho(z)$

We have already touched upon the density profile $\rho(z)$ for the characterization of $H$ in Sec. 4.2. The ensemble and time averaged number density distribution is given by $\rho(z) = \left\langle \overline{\hat{\rho}(z)} \right\rangle$ with $\hat{\rho}(z) = \sum_{i=1}^{N} w_{\text{id}}(z; z_i)$ being the instantaneous distribution using the weighting function $w_{\text{id}}(z; z_i)$ defined in Sec. 3.7, Eq. 3.4. The density profile for *film1* at $T = 0.50$ in the liquid limit is shown in Fig. 6-1(a). $z = 0$ corresponds to the center of mass of our films. As emphasized by the dashed horizontal line the midplane number density $\rho_0 \equiv \rho(z \approx 0)$ can be fitted to high precision and we can, thus, determine the film thickness $H$ using Eq. 4.1 [68]. The interface width $W$ shown in Fig. 6-1(b) is obtained by fitting the $\rho(z)$-data at the two surfaces with the mean-field prediction [124]

$$\rho(z) = \frac{\rho_0}{2} \left( 1 - \text{erf}\left( \frac{|2z - H|}{W} \right) \right) \tag{6.1}$$

which is indicated by the solid line in Fig. 6-1(a). $W$ decreases weakly upon cooling becoming roughly constant in the low-$T$ limit. The small value of $W$ is a consequence of the large surface tension $\Gamma$ of order unity (Sec. 6.4).

The midplane number density $\rho_0$ is shown in Fig. 6-2 for all our films. Albeit $\rho_0$ increases slightly upon cooling, still being $\approx 1$ which implies $H \sim 1/L^2$ to leading order. While this
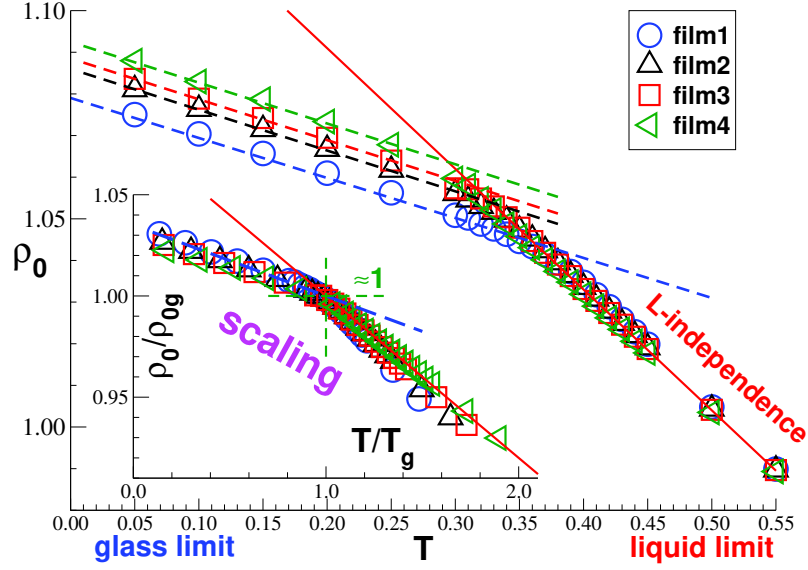
Figure 6-2: Midplane density $\rho_0(T)$ for all our films. While $\rho_0$ does not depend on $H$ in the liquid limit, it decreases with increasing $H$ in the glassy limit. This allows to determine the glass transition temperature $T_g$ and the midplane density $\rho_{0g} \sim 1/H_g$ at the glass transition. Inset: Scaling of $\rho_0/\rho_{0g}$ vs $T/T_g$ using $\rho_{0g}$ and $T_g$ as indicated in Table 3.1.

also holds to higher order in the liquid regime, i.e. $\rho_0$ is strictly $H$-independent, $\rho_0$ is seen to decrease with increasing $H$ in the glass limit. Apparently, the thicker films do not manage to get as compact as the thinner films for $T \ll T_g$. As discussed in Ch. 4, this may be used to define the quasi-thermodynamic glass transition temperature $T_g$, the midplane number density $\rho_{0g}$ and film thickness $H_g$ at the transition from the intercept of the linear glass and liquid asymptotes. The values for $T_g$, $H_g$ and $\rho_{0g}$ are given in Table 3.1. This allows to collapse the midplane densities $\rho_0(T)$ of all films as shown in the inset of Fig. 6-2.

## 6.3 Energy profile $e(z)$

We compute the energy contribution $\hat{e}(z)$ to the total instantaneous energy $\hat{e}$ using the weighting functions $w_{id}(z; z_i)$ and $w_{ex}(z; z_i, z_j)$ defined in Sec. 3.7. The time and ensemble averaged energy distribution $e(z)$ is presented in Fig. 6-3(a) comparing films of two lateral box sizes (*film1* and *film2*) for two temperatures ($T = 0.55$ and $T = 0.20$). The midplane energy density $e_0 \equiv e(z \approx 0)$ is seen to be $H$-independent above $T_g$. A better representation of the midplane energy density $e_0$ (open symbols) is shown in Fig. 6-3(b), plotted as a function of $T$ for all our films. The global energy density $e$ (filled symbols) is also given
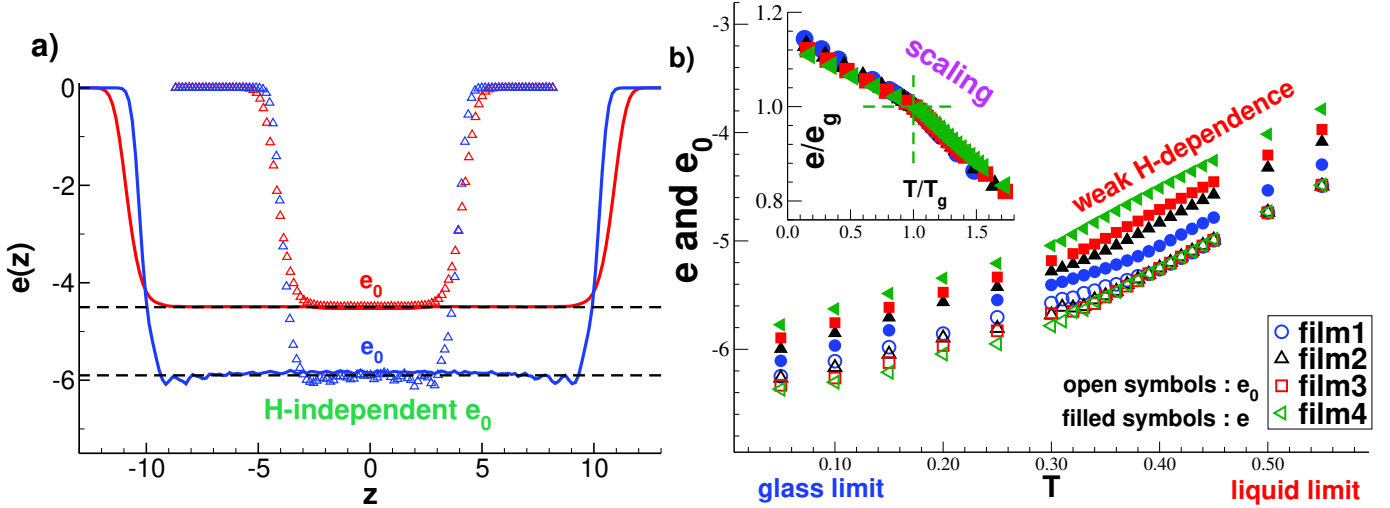
Figure 6-3: **(a)** In-plane energy profiles $e(z)$ for *film1* (lines) and *film2* (symbols) for two selected temperatures $T = 0.55$ and $T = 0.20$. The midplane energy $e_0$ is seen to be $H$-independent for $T \gg T_{\mathrm{g}}$. **(b)** Midplane energy density $e_0$ and global energy density $e$ vs $T$ for our films as indicated. Inset: $e$ brought to scale by setting $x = T/T_{\mathrm{g}}$ and $y = e/e_{\mathrm{g}}$.

in the same plot. Note that $e_0 < e$ and that both $e_0$ and $e$ decrease upon cooling. It is also seen that $e_0$ is $H$-independent above $T_{\mathrm{g}}$ and only weakly $H$-dependent in the glassy limit. This higher order effect is expected in the glassy regime where $\rho_0$ weakly depends on $H$. The average energy density $e$ decreases more strongly with increasing $H$. This can be attributed to the broad bulk regime (more negative) for thicker films. For thinner films, the interface contribution (less negative) dominates the bulk contribution. By focusing on the filled symbols in Fig. 6-3(b), it becomes clear that as the film shrinks, the spread of the values of $e$ is reduced. This is also readily seen from Fig. 6-3(a).

## 6.4   Normal tangential stresses

Following the Irving-Kirkwood convention, Sec. 3.7, we also computed the layer-resolved distribution $\hat{\sigma}_{\alpha\beta}(z)$ of the total instantaneous stress tensor $\hat{\sigma}_{\alpha\beta}$ taking into account both the ideal and the excess stress contributions. We remind that the Irving-Kirkwood convention implies the linear sum rule (Eq. 3.8)

$$\hat{\sigma}_{\alpha\beta} = \frac{\delta z_{\mathrm{b}}}{H} \sum_{b=1}^{n_{\mathrm{b}}} \hat{\sigma}_{\alpha\beta}(z_b) \tag{6.2}$$
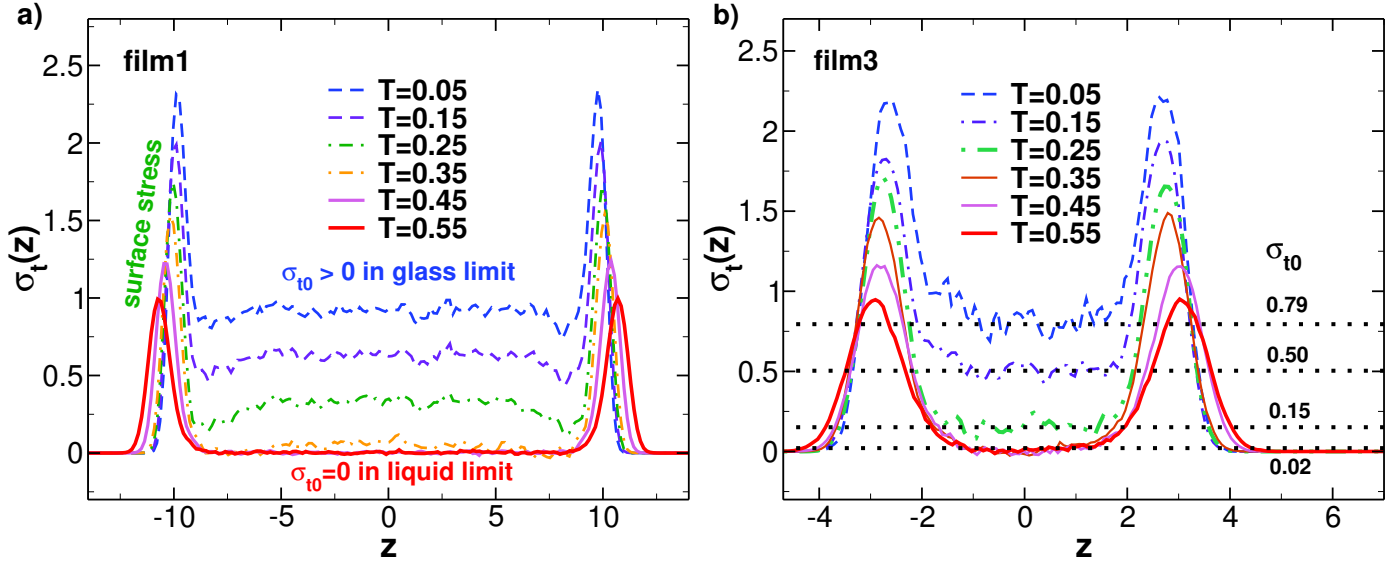
70

Figure 6-4: The total tangential stress $\sigma_t(z) \equiv (\sigma_{xx}(z) + \sigma_{yy}(z))/2$ for various temperatures for **(a)** *film1* and **(b)** *film3*. $\sigma_t(z)$ is always bimodal with maxima at the free interfaces of the film. While the midplane tangential stress $\sigma_{t0} \equiv \sigma_t(z \approx 0)$ vanishes above the glass transition, it becomes finite for temperatures below $T_g$. This must be taken into account for the determination of the surface tension.

for all instantaneous stress tensor components. The average off-diagonal elements of the stress tensor, such as the shear stress $\sigma_{xy}(z)$, all vanish by symmetry. Since the vertical box size $L_z$ is sufficiently large that all components of the stress tensor $\sigma_{\alpha\beta}(z)$ [57] strictly vanish outside the films, the average vertical normal stress $\sigma_{zz}(z)$ must also vanish for all $z$-planes [34]. At variance to this, the average tangential normal stresses $\sigma_{xx}(z)$ and $\sigma_{yy}(z)$ may be finite.[31] Since the $x$- and the $y$-directions are equivalent we consider here the average tangential stress $\sigma_t \equiv (\sigma_{xx} + \sigma_{yy})/2$ and its distribution $\sigma_t(z) \equiv (\sigma_{xx}(z) + \sigma_{yy}(z))/2$.

$\sigma_t(z)$ is presented in Fig. 6-4 for *film1* and *film3* for several temperatures. (Unfortunately, only $N_c = 10$ configurations are available for *film3*.) As for all our films studied, $\sigma_t(z)$ is seen to be bimodal with strong and sharp maxima at the film surfaces. Since for liquids all average normal stress components must be equal [6, 137] and since $\sigma_{zz}(z) = 0$ everywhere, $\sigma_t(z \approx 0)$ vanishes rigorously for *film1*, *film2* and *film3* for high temperatures. Interestingly, upon further decreasing the temperature below the glass transition $\sigma_t(z)$ is observed to become finite around $z = 0$. This makes manifest that the film center is no longer a liquid. The bulk tangential stress $\sigma_{t0}$ for all our films are taken as the mean value

---

[31]This is possible due to the rigid constraint imposed by the periodic boundary conditions, i.e. the simulation box balances the tensile tangential stresses along the films.
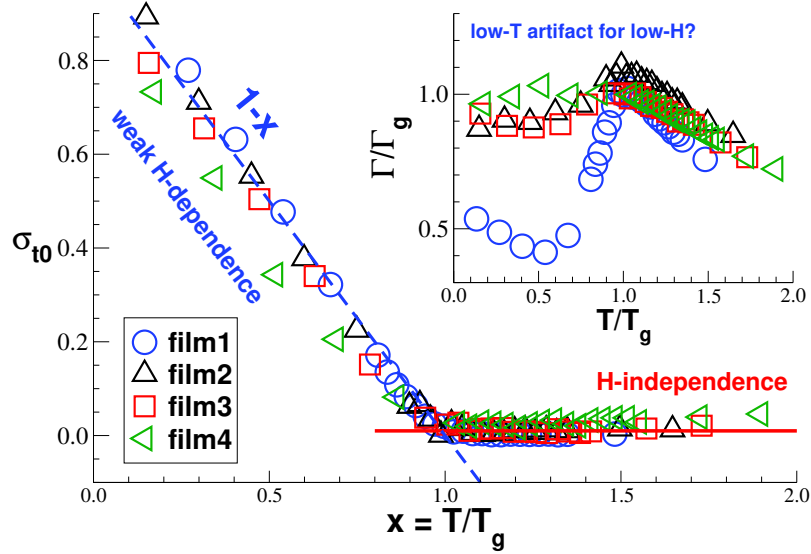
71

Figure 6-5: Tangential stress $\sigma_{t0}$ at the film midplane (main panel) and surface tension $\Gamma \equiv (\sigma_t - \sigma_{t0})H/2$ (inset) as functions of $x = T/T_g$ for all our films. The vertical axis of the inset is made dimensionless using $\Gamma_g \equiv \Gamma(T = T_g)$.

across a certain number of bins around the film midplane at $z = 0$. $\sigma_{t0}$ is presented in the main panel of Fig. 6-5 as a function of the reduced temperature $x = T/T_g$. The finite $\sigma_{t0}$-value is not a computational artifact but caused by the tendency of the film to reduce its thickness $H$ at a fixed lateral box length $L$. While at high temperature an initial finite tension $\sigma_{t0} > 0$ can relax by the vertical flow of the particles reducing $H$, this gets increasingly difficult and ultimately impossible around and below $T_g$. The observed $\sigma_{t0} > 0$ is hence a direct consequence of the broken permutation symmetry, i.e. the neighborhood of each particle becomes frozen [137].[32] Please note also that $\sigma_{t0}$ does not rigorously vanish for our thinnest films even for $T \gg T_g$. As can be seen from the two examples given in Fig. 6-4, this is due to the fact that as the films becomes thinner the surface peaks of $\sigma_t(z)$ increasingly overlap. The clear separation of surface and bulk behavior becomes spurious.

To make this point clear let us give an additional characterization of the surface width. As shown in the inset of Fig. 6-6 we first determine the maximum $\sigma_{max}$ of the peak and define then peak width $W_t = z_+ - z_-$ with $\sigma_t(z_\pm) - \sigma_{t0} = (\sigma_{max} - \sigma_{t0})/2$, i.e. we take the bulk normal stress $\sigma_{t0}$ as the reference and determine then the peak width at half the (shifted) peak height. As presented in the main panel of Fig. 6-6, the peak width $W_t$ becomes narrower upon cooling and upon increasing the film thickness. It is roughly similar

---

[32]We have currently no explanation for the observed linear decay in the glass regime (dashed line).
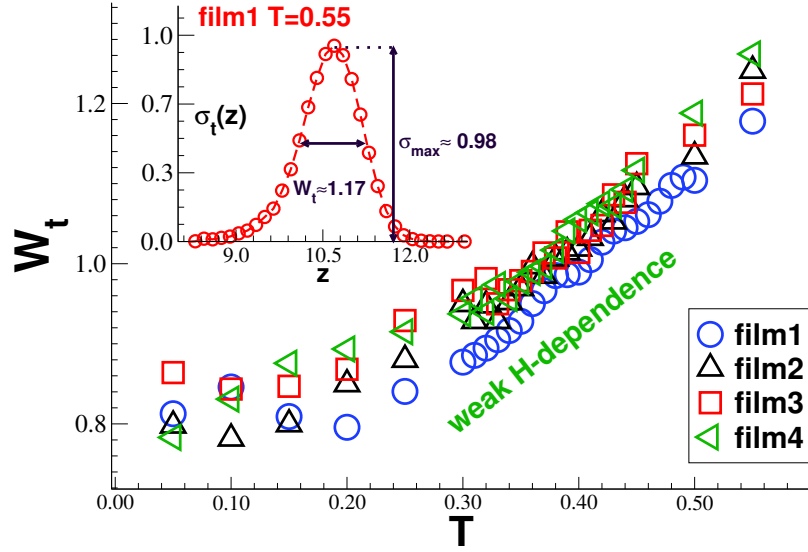
Figure 6-6: In the main panel $W_t(T)$ is presented for various $L$ while the inset illustrates the determination of $W_t$ for *film1* and $T = 0.55$. $\sigma_{max} \approx 1$ and $\sigma_{t0} \approx 0$ in this case.

to the width $W$ from the density profile, Fig. 6-1(b). Since the ratio $H/2W_t$ is about 3 for *film4*, the two-layer model should be used with care for these ultrathin films.

The normal tangential stress $\sigma_t$ and its distribution $\sigma_t(z)$ are, obviously, related to the surface tension $\Gamma$. We remind that for a liquid film with $\sigma_{t0} = 0$ [57, 78]:

$$2\Gamma = \delta z_b \sum_i \sigma_t(z_i) = H\ \sigma_t. \tag{6.3}$$

However, as noted above, $\sigma_{t0} \approx 0$ does not hold below the glass transition. Since there is thus no true liquid phase in the film center, Eq. 6.3 cannot be used. Using a Gibbs dividing plane construction, the total tangential stress $\sigma_t H$ has now the two contributions $\sigma_{t0} H$ and $\Gamma$. The finite tangential midplane stress $\sigma_{t0}$ has to be subtracted [138] and we *define*[33]

$$2\Gamma \equiv (\sigma_t - \sigma_{t0})\ H \tag{6.4}$$

if the surface tension is computed through and below $T_g$. The surface tension $\Gamma$ is presented in the inset of Fig. 6-5. Interestingly, $\Gamma(T)$ is non-monotonic: it increases first upon cooling in the liquid regime and decreases then in the glass regime. The vertical axis is made dimensionless using $\Gamma_g \equiv \Gamma(T = T_g)$ (cf. Table 3.1). The scaling attempt is not successful.

---

[33]See the general comment at the end of this section.

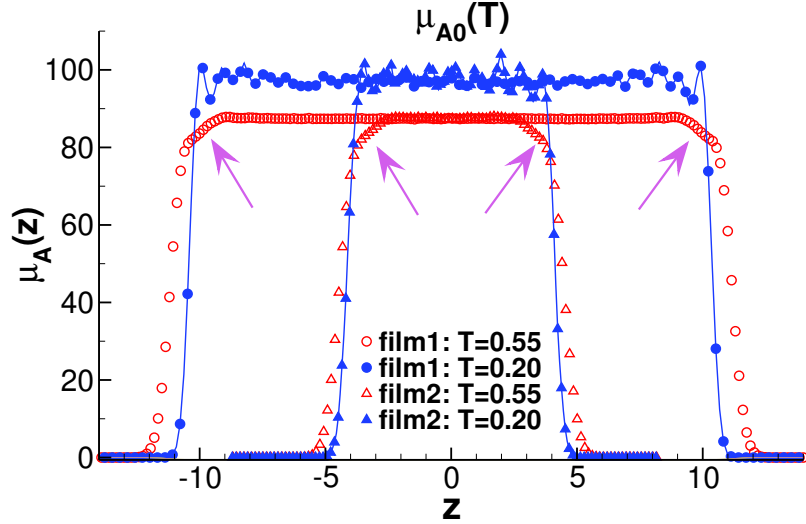Figure 6-7: Distribution $\mu_A(z)$ of the affine shear modulus $\mu_A$ for *film1* and *film2* for one temperature in the liquid limit ($T = 0.55$) and one in the glass limit ($T = 0.20$). The midplane plateau $\mu_{A0}(T)$ is $H$-independent. As indicated by arrows, surface effects are only strong in the liquid limit.

We finally note that since below $T_g$ the particle positions are essentially frozen, the free energy per area to reversibly create a surface and the tangential normal surface stress, Eq. 6.4, becomes strain-dependent and may differ. Due to this well-known "Shuttleworth effect" [57, 138–141] the notion "surface tension" used for the property $\Gamma$ defined above by Eq. 6.4, characterizing rather the "surface stress", may be misleading for our amorphous films below $T_g$ [138, 141], as in general for solids [139, 140].

## 6.5   Local affine shear modulus $\mu_A(z)$

As noted above, the average shear stress $\tau(z) \equiv \sigma_{xy}(z)$ vanishes by symmetry. According to Eq. 3.8 and Appendix B.1 $\tau(z)$ is the linear-additive $z$-contribution to the first shear-strain derivative $\tau$ of the system Hamiltonian. The corresponding second shear-strain derivative $\mu_A$ and its distribution $\mu_A(z)$ do, however, not vanish. This is shown in Fig. 6-7 for *film1* (circles) and *film2* (triangles) focusing on one temperature in the liquid limit ($T = 0.55$) and one deep in the glass ($T = 0.20$). Similar as for the midplane energy density $e_0$, the plateau value $\mu_{A0} \equiv \mu_A(z \approx 0)$ is in leading order $H$-independent. The decay of $\mu_A(z)$ at the surface is qualitatively different in both $T$-limits. It decreases smoothly in the liquid limit as marked by the arrows. Since for thinner films the midplane plateau has a decreasing

weight $\propto (H - W)$, this implies that the average $\mu_A$ must *decrease* as

$$\mu_A = \frac{\delta z_b}{H} \sum_b \mu_A(z_b) \approx \mu_{A0} \left( 1 + \frac{\mu_{As}/\mu_{A0}}{H} \right) \tag{6.5}$$

where the fit parameter $\mu_{As}$ characterizes the contributions from the film surfaces. This is consistent with data presented in Fig. 4-3. Interestingly, $\mu_A(z)$ is seen in Fig. 6-7 to drop suddenly in the glass regime. The surface contribution $\mu_{As}$ is thus negligible. This explains why $\mu_A(\approx \mu_{A0})$ was found to barely depend on $H$ at low temperatures (Fig. 4-3).

## 6.6 Local shear-stress fluctuations $\mu_F(z)$

We turn now to the characterization of the shear-stress fluctuations. As already noted above, the average shear stress $\tau(z)$ vanishes for all $z$. As may be seen from Fig. 6-8, this is not the case for the higher moment

$$\mu_F(z) \equiv \beta V \left\langle \overline{(\hat{\tau}(z) - \overline{\hat{\tau}(z)})\,(\hat{\tau} - \overline{\hat{\tau}})} \right\rangle \tag{6.6}$$

characterizing the correlation of the local shear stress $\hat{\tau}(z)$ and the total shear stress $\hat{\tau}$. Importantly, the total film volume $V = HL^2$ is used as prefactor and not the slab volume $V_b = \delta z_b L^2$. The above definition is thus consistent with the linear sum rule, Eq. 3.8, i.e.

$$\mu_F \equiv \beta V \left\langle \overline{(\hat{\tau} - \overline{\hat{\tau}})^2} \right\rangle = \frac{\delta z_b}{H} \sum_b \mu_F(z_b). \tag{6.7}$$

This is also consistent with the general stress-fluctuation formalism for the local contributions to the elastic moduli used in the literature [42, 97, 142, 143]. We emphasize that $\mu_F(z)$ depends not only on $\hat{\tau}(z)$, but also on the total shear stress $\hat{\tau}$. It is thus *not* a completely local observable as it would have been the case using instead:

$$\mu_F^{loc}(z) \equiv \beta V_b \left\langle \overline{\hat{\tau}(z)^2} - \overline{\hat{\tau}(z)}^2 \right\rangle. \tag{6.8}$$

Importantly, the linear sum Eq. 6.7 does not hold for $\mu_F^{loc}(z)$ in general. However, it is expected that $\mu_F(z)$ and $\mu_F^{loc}(z)$ become equivalent assuming that the stresses of different $z$-planes decorrelate, i.e., $\left\langle \overline{\hat{\tau}(z)\hat{\tau}(z')} \right\rangle \sim \delta_{z,z'}$.
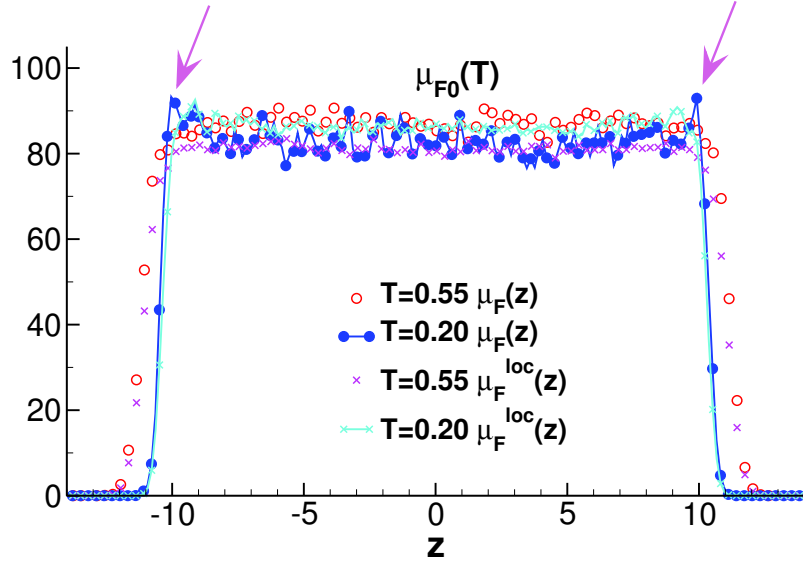
Figure 6-8: Distributions $\mu_F(z)$ and $\mu_F^{\text{loc}}(z)$ of the stress fluctuations. The midplane plateau $\mu_{F0} \equiv \mu_F(z \approx 0)$ is again to leading order $H$-independent. It decreases upon cooling. While $\mu_F(z)$ is similar to $\mu_A(z)$ for all $z$ in the high-$T$ limit, it becomes bimodal for $T \ll T_g$ with maxima at the free surfaces (arrows). The characterization of $\mu_F^{\text{loc}}(z)$ remains similar to $\mu_F(z)$ and $\mu_A(z)$ around the interfaces, but in the bulk they differ (see footnote 35).

The linear-additive distribution $\mu_F(z)$ is presented in Fig. 6-8.[34] Let us first consider the high-$T$ limit shown for $T = 0.55$. As one expects from the equality $\mu_A = \mu_F$ of the overall film averages, it is seen from the comparison of Fig. 6-7 and Fig. 6-8 that $\mu_A(z) = \mu_F(z)$ holds for $T \gg T_g$. This also explains why the same $1/H$-correction has been obtained for $\mu_A$ and $\mu_F$.[35] In the low-$T$ limit, qualitatively different distributions are observed. Upon cooling $\mu_F(z)$ decreases in the inner parts of the film while is remains similar to $\mu_A(z)$ around the surfaces. The arrows in Fig. 6-8 point to the peaks at $T = 0.20$ near the interface that were already seen for $\mu_A(z)$. In addition, the distribution is somewhat bimodal as seen in Fig. 6-8. The contribution from the surfaces is more important for thin films, this explains why the overall $\mu_F$ increases for thinner films below $T_g$ as shown in Fig. 4-4.

---

[34]The presented data for *film1* is shown for $N_c = 10$ with $\delta t_{\text{trj}} = 2.5$. Whereas the data for *film2* is shown for $N_c = 10$ but with a *lower* sampling rate $\delta t_{\text{trj}} = 500$. As a result noise grows into the data for *film2*. For clarity the data for *film2* was smoothed.

[35] As a remark on $\mu_F^{\text{loc}}(z)$, please note that $\mu_F^{\text{loc}}(z)$ remains similar to $\mu_A(z) \approx \mu_F(z)$ around the interfaces ($|z| \approx H/2$) while we observed $\mu_F^{\text{loc}}(z) \ll \mu_F(z)$ in the bulk of the film for all $T$ (Fig. 6-8). In addition, the local definition $\mu_F^{\text{loc}}(z)$ fails for our thinner films as the local stress-fluctuations of different $z$-slabs are still correlated. Apparently, the shear stresses are correlated over a correlation length $\xi$ with $\xi \gg \delta z_b$. This questions the validity of a true "local" $\mu_F^{\text{loc}}(z)$ as in Eq. 6.8. Overall, $\mu_F^{\text{loc}}(z)$ will not predict a reasonable $\mu(z)$ due to its peculiar nature. For this reason we focus on the linear-additive distribution $\mu_F(z)$, Eq. 6.6.
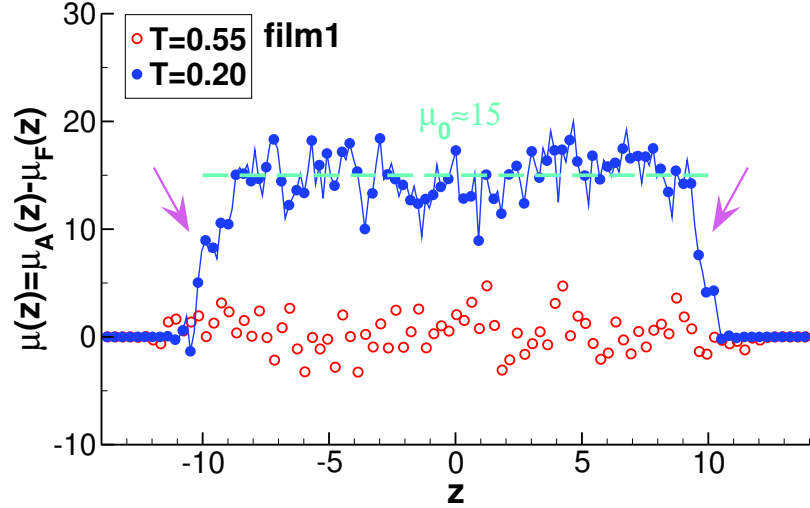
Figure 6-9: Distribution $\mu(z) \equiv \mu_\mathrm{A}(z) - \mu_\mathrm{F}(z)$ of the shear modulus for *film1* and two temperatures. While $\mu(z)$ vanishes in the liquid limit (open circles), it becomes finite below $T_\mathrm{g}$ with a plateau in the bulk phase in the middle of the films (dashed horizontal line) sandwiched by the softer surface layers marked by the arrows.

## 6.7  Local shear modulus $\mu(z)$

The shear modulus $\mu(z) \equiv \mu_\mathrm{A}(z) - \mu_\mathrm{F}(z)$ computed according the linear-additive local stress-fluctuation formula is presented for two temperatures in Fig. 6-9 for *film1*. As one expects, $\mu(z) \approx 0$ for all $z$ in the liquid limit $T = 0.55$ (red dots). $\mu(z)$ becomes finite below for $T = 0.20$ (blue dots in Fig. 6-9) with a broad maximum at the midplane. For $T = 0.20$, the interface peaks seen in Fig. 6-7 and Fig. 6-8 cancel each other, leading to the finite surface regime of several bead diameters emphasized by the arrows. $\mu(z)$ is presented for additional temperatures in Fig. 6-10 for *film1*. Of prominence is the behavior at $T \approx T_\mathrm{g} = 0.37$ (green dots), where, although noisy, the contribution to the global $\mu$ is seen to come from the bulk of the film. Our results reveal that there is a transition from a high modulus in the bulk to a low modulus at the surface. The reduction in the shear modulus $\mu(z)$ in the surface region implies the existence of a *soft, liquid-like* interface, which has been proposed in many experimental and theoretical studies [9, 19, 22, 43, 55, 76, 87, 144, 145]. From the layer analysis of *film1*, we confirm this effect for the first time using the *local* stress-fluctuation formalism.
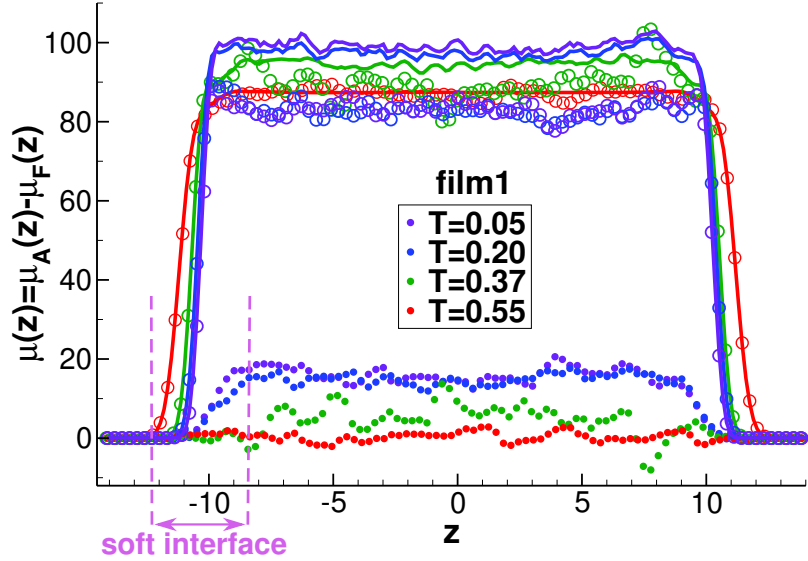
Figure 6-10: The shear modulus $\mu(z)$ (dots), the affine term $\mu_A(z)$ (lines) and the fluctuation term $\mu_F(z)$ (circles) computed for *film1* according the $z$-linear stress-fluctuation formula is presented for selected temperatures. Presented results are smoothed over a window = 5. The reduction in shear modulus $\mu(z)$ near the surface implies the existence of a *soft* interface, which has been proposed in the literature. From our layer analysis, we confirm this effect for *film1* using the stress fluctuation formalism for the first time.

## 6.8 Major results

In this chapter we have investigated the $z$-distributions of various mechanical and rheological properties such as the density $\rho(z)$, the energy $e(z)$ and the different components of the stress tensor $\sigma_{\alpha\beta}(z)$. We determined the surface tension $\Gamma$ from the normal tangential stress components (Sec. 6.4). We then focused on the affine shear-modulus $\mu_A(z)$ (Fig. 6-7), the shear-stress fluctuations $\mu_F(z)$ (Fig. 6-8), and the shear modulus $\mu(z) = \mu_A(z) - \mu_F(z)$ (Fig. 6-9). While in the high-$T$ limit $\mu_F(z) \approx \mu_A(z)$ and $\mu(z)$ thus vanishes for all $z$, $\mu(z)$ becomes finite around and below the glass transition. Most importantly, in agreement with Eq. 1.3 and confirming the proposed two-layer model [9, 19, 22, 43, 55, 76, 87, 144, 145] $\mu(z)$ is monomodal with a broad, essentially $H$-independent maximum in the bulk phase of the films and surface layers of finite width $W_t \approx 1$ where $\mu(z)$ continuously vanishes.

# Chapter 7

# Ensemble fluctuations of shear stress fluctuations

## 7.1   Introduction

In the previous chapters 4-6 we have numerically characterized important, experimentally measurable properties of polymer thin films focusing on the *average* viscoelastic linear response. In agreement with the related recent numerical findings on self-assembled transient networks [101] and three-dimensional polymer melts [65–67] it was observed that the shear-stress relaxation function $G(t)$ and the (generalized) shear modulus $\mu$ strongly fluctuate and this especially at temperatures around the glass transition temperature $T_\mathrm{g}$. This prompted the theoretical work outlined in Ch. 2 and in Appendix A. This work suggests that it may be possible to describe the observed fluctuations assuming that the time series $\mathbf{x}$ of (rescaled) shear stresses $\hat{\tau}$ used for calculating $G(t)$ and $\mu$ are stationary Gaussian processes [69, 77]. As we have emphasized in Sec. 2.6, it is important to distinguish stochastic processes which are ergodic from those which are effectively non-ergodic. The latter case should matter for films at low temperatures $T \ll T_\mathrm{g}$. Taking advantage from the abundance of independently prepared configurations $N_\mathrm{c}$ for *film1*, we test here some of the predictions presented in Ch. 2. The presented chapter is adapted from our recent publications [69, 70] where, in addition to polymer films, systems of self-assembled transient networks and polydisperse LJ particles were studied.
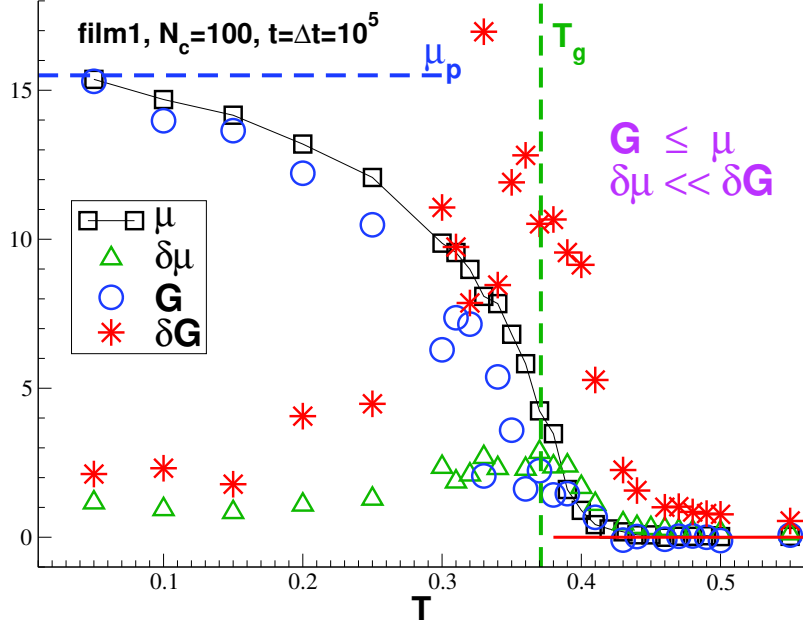
Figure 7-1: Shear modulus $\mu$, shear relaxation modulus $G$ and the corresponding standard deviations $\delta\mu$ and $\delta G$ taken at $t = \Delta t = \Delta t_{\max} = 10^5$ as functions of $T$. The observed two inequalities $G \leq \mu$ and $\delta G \gg \delta\mu$ are both consequences of the stationarity relation Eq. 1.2. The corresponding error bars $\delta\mu/\sqrt{N_c - 1}$ and $\delta G/\sqrt{N_c - 1}$ are not shown.

## 7.2  Standard deviations $\delta G$ and $\delta\mu$

As already pointed out in Ch. 4, the data for $G(t)$ is quite noisy, especially around $T_g$, and we had to use gliding averages and a strong logarithmic binning for the clarity of the presentation. We now describe this qualitative observation in quantitative terms. In Fig. 7-1 we compare $\mu$ and $G$ and their respective standard deviations $\delta\mu$ and $\delta G$, Eq. A.24, taken at the same constant time $t = \Delta t = \Delta t_{\max} = 10^5$ and plotted as a function of the temperature $T$. While we still average over the $N_c$ independent configurations, we do not use any gliding averaging or logarithmic binning. As we saw in Fig. 1-2, $\mu(T)$ decreases both continuously and smoothly with $T$. Albeit $G(T)$ decreases also continuously, it reveals an erratic behavior for temperatures slightly below $T_g$ (vertical dashed line). The inequality $G(T) \leq \mu(T)$ for all temperatures is expected from Eq. 1.2. More importantly, being the second integral over $G(t)$, the shear modulus $\mu$ automatically filters off the high-frequency noise. This explains the observed strong inequality $\delta\mu \ll \delta G$ of the standard deviations. At variance to $\mu$ and $G$, a striking *non-monotonic* behavior[36] is observed for $\delta\mu$ and $\delta G$ with

---

[36]This non-monotonic behavior and the similar findings for self-assembled networks [101] and 3D polymer bulk systems [65, 66] prompted the interest in stationary Gaussian stochastic processes, Ch. 2.
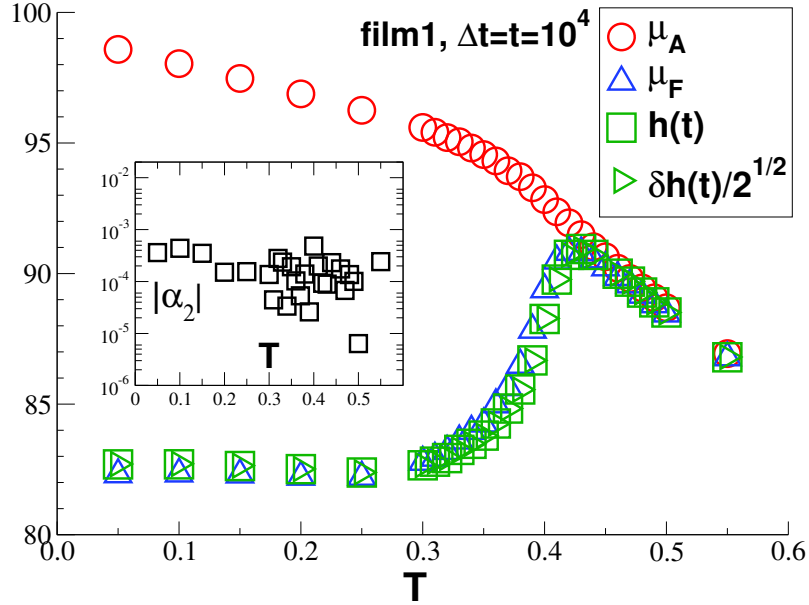
Figure 7-2: Direct test of the Gaussianity of the stochastic process, Eq. 2.34, for *film1* and $\Delta t = t = 10^4$. Main panel: Comparison of $\mu_{\mathrm{A}}$, $\mu_{\mathrm{F}}$, $h$ and $\delta h/\sqrt{2}$ as a function of $T$. $h \approx \mu_{\mathrm{F}}$ is non-monotonic with a maximum slightly below $T_{\mathrm{g}}$. Since Eq. 2.34 holds, $\delta h$ is also non-monotonic. Inset: Absolute value of the non-Gaussianity parameter $\alpha_2$ as a function of $T$ demonstrating, $|\alpha_2| \ll 0.0007$, the high accuracy of the Gaussian assumption.

maxima slightly below the glass transition temperature $T_{\mathrm{g}}$. While $\delta\mu \ll \mu$ and $\delta G \ll G$ in the solid limit, $\delta\mu > \mu$ and $\delta G > G$ at high and intermediate temperatures. Importantly, the presented data is characterized by strong ensemble fluctuations with $\delta\mu/\mu$ and $\delta G/G$ of order of unity, similar to what has been observed for 3D bulk systems [65, 66]. The inequalities $\delta\mu \ll \delta G$ and $\delta\mu/\mu \ll \delta G/G$ are the strongest slightly below $T_{\mathrm{g}}$. Therefore, the prediction of $G(T)$ or $\mu(T)$ for $T \approx T_{\mathrm{g}}$ becomes thus meaningless for a single configuration. This suggests that numerical studies of the elastic shear strain response around the glass transition should focus on $\mu$ rather than of $G$ as $\delta\mu \ll \delta G$. As already noted at the end of Sec. 2.5, we have verified that $\delta G \approx \delta h(t)$ and $\delta\mu \approx \delta\mu_{\mathrm{F}}$ holds. This is expected since the simple average $\mu_{\mathrm{A}}$ barely fluctuates.

## 7.3 Standard deviation $\delta h(t)$

In order to explain the non-monotonic behavior of $\delta G$, Fig. 7-1, we address now the standard deviation $\delta h$ of the autocorrelation function $h$. As explained in Sec. 2.5 we expect $\delta h^2 = 2h^2$, Eq. 2.34, for a Gaussian stochastic process. We compare in the main panel of Fig. 7-2
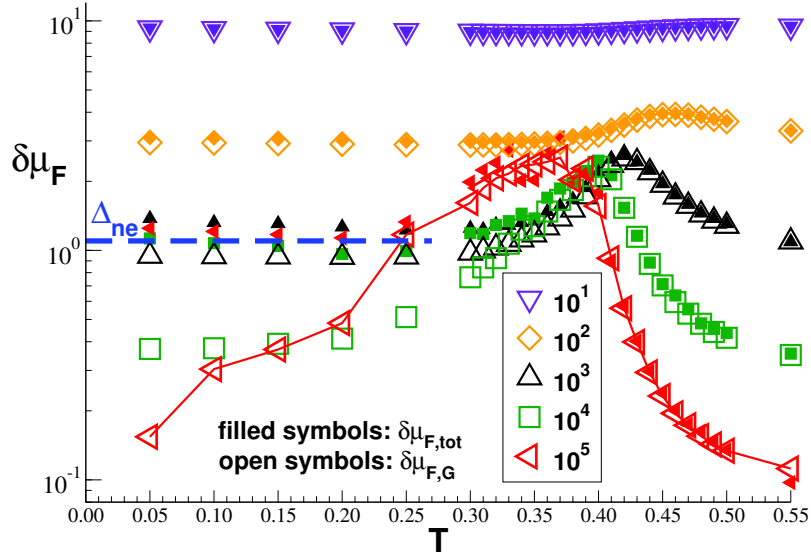
Figure 7-3: Temperature dependence of $\delta\mu_F$ for free-standing films with open symbols indicating $\delta\mu_{F,G}$ and filled symbols $\delta\mu_{F,tot}$. While $\delta\mu_{F,G} \approx \delta\mu_{F,tot}$ for small $\Delta t$ and all $T$, both differ below $T_g$ and the more the larger $\Delta t$. The bold dashed line marks the limit $\Delta_{ne} \approx 1$ for large sampling times $\Delta t$ and low temperatures $T$.

$\mu_A$, $\mu_F$, $h$ and $\delta h/\sqrt{2}$ as a function of temperature focusing on *film1* ($L = 23.5$) and on $\Delta t = t = 10^4$. As can be seen the data for $\mu_F$, $h$ and $\delta h/\sqrt{2}$ collapse on one mastercurve with strong maximum slightly below $T_g$. That $\mu_F \approx h$ is a consequence of the *stationarity* of the stochastic process, as summarized by Eq. 1.2 or Eq. 2.2, and the large time $t = \Delta t$ considered. That $h \approx \delta h/\sqrt{2}$ is a consequence of its *Gaussianity*. This latter point may be better seen from the usual non-Gaussianity parameter $\alpha_2 \equiv \delta h^2/h^2 - 1$ presented in the inset. Apparently, the deviations from the assumed Gaussianity are always negligible. This shows that Gaussian processes are dominant for all T, even below the glass transition. Obviously, this does not rule out very small sub-dominant non-Gaussian contributions.[37]

## 7.4 Standard deviation $\delta\mu_F$

We characterize now the standard deviation $\delta\mu_F$ of $\mu_F$. We begin by comparing in Fig. 7-3 the temperature dependence of $\delta\mu_{F,tot}$, operationally defined by Eq. A.24, and the prediction $\delta\mu_{F,G}[G(t)]$ for Gaussian ergodic processes, Eq. 2.3, computed using the measured relaxation function $G(t)$. The most important feature is here that within numerical precision $\delta\mu_{F,tot} \approx \delta\mu_{F,G}$ for all $\Delta t$ and $T \gg T_g$, while both differ below $T_g$ for large $\Delta t$. It

---

[37]This could be investigated by considering higher order correlation functions and their variances.

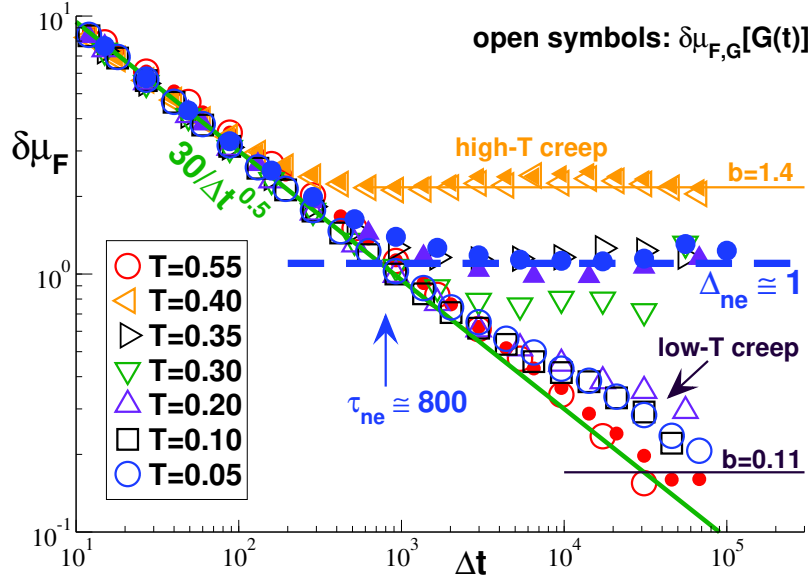Figure 7-4: $\Delta t$-dependence of $\delta\mu_{F,G}[G]$ (open symbols) for all indicated $T$ and of $\delta\mu_{F,tot}$ (filled symbols) for $T = 0.55, 0.4, 0.2$ and $0.05$. The $1/\sqrt{\Delta t}$-decay for small $\Delta t$ is shown by the bold solid line, the plateau value $\Delta_{ne} \approx 1$ of $\delta\mu_{F,tot}$ for small $T$ and $\Delta t \gg \tau_{ne} \approx 800$ by the bold dashed line and $\delta\mu_{F,G} \approx 1.55|b|$ ($b = 1.4$ for $T = 0.4$ and $b = 0.11$ for $T = 0.05$) expected for logarithmic creep by thin horizontal lines.

can also be seen that the maximum of $\delta\mu_{F,G}(T)$ becomes sharper and shifts to lower $T$ with increasing $\Delta t$. While $\delta\mu_{F,G}$ decreases strongly on cooling for larger $\Delta t$ – this is not observed for $\delta\mu_{F,tot}$, being only weakly $T$-dependent. As marked by the bold dashed line, $\delta\mu_{F,tot} \to \Delta_{ne} \approx 1$ in this limit. Apparently, Eq. 2.3 for ergodic Gaussian processes breaks down as expected from the more general relations Eq. 2.43 or Eq. 2.45.

An alternative representation of the same data is given in Fig. 7-4 focusing on the $\Delta t$-dependence of $\delta\mu_{F,G}$ and $\delta\mu_{F,tot}$. $\delta\mu_{F,tot} \approx \delta\mu_{F,G}$ holds again for $T$ above and around $T_g$. Note also that $\delta\mu_{F,tot} \approx \delta\mu_{F,G} \propto 1/\sqrt{\Delta t}$ (bold solid line) for all $\Delta t \leq \Delta t_{max}$ for the largest temperature $T = 0.55$. Interestingly, $T$-dependent shoulders appear for $T \approx 0.4$. This is a consequence of the creep-like decay of $G(t)$ in this regime which is approximately fitted by $G(t) \approx a - b\ln(t)$ as indicated in Fig. 4-9. According to Appendix A.3 (cf. Fig. A-3), one expects a shoulder with $\delta\mu_{F,G} \approx 1.55|b|$. That this holds is seen by the upper thin horizontal line using $b = 1.4$ for $T = 0.4$. In the low-$T$ limit we see again that $\delta\mu_{F,tot}$ becomes constant, $\delta\mu_{F,tot} \approx \Delta_{ne}$ for $\Delta t \gg \tau_{ne} \approx 800$, while $\delta\mu_{F,G}$ continues to decrease with $\Delta t$. The small deviations of $\delta\mu_{F,G}$ from the $1/\sqrt{\Delta t}$-asymptote are caused by the fact that $G(t)$ does *not* become rigorously constant, $G(t) \to \mu_p > 0$, even for our lowest
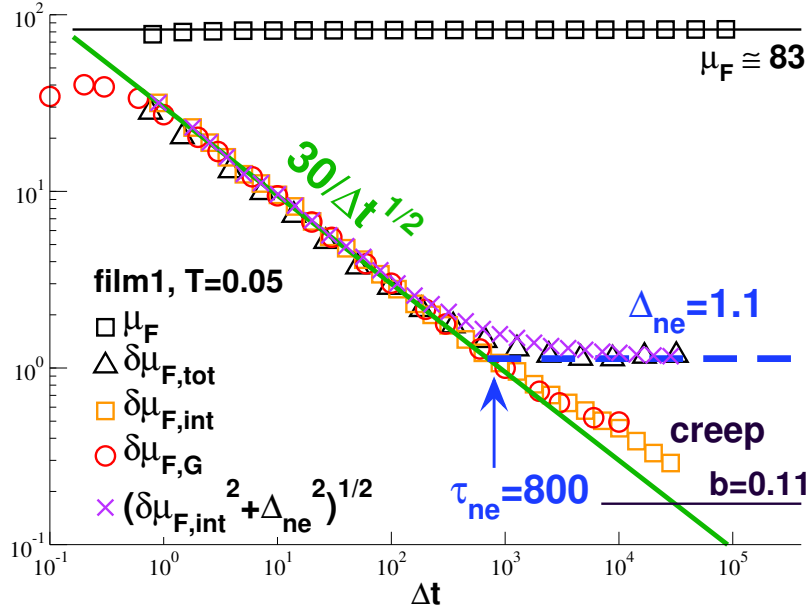
Figure 7-5: $\Delta t$-dependence for $\mu_F$, $\delta\mu_{F,tot}$, $\delta\mu_{F,int}$ and $\delta\mu_{F,G}$ for *film1* and the low temperature $T = 0.05$. The bold solid line indicates the expected $1/\sqrt{\Delta t}$-decay $\delta\mu_{F,int} \approx \delta\mu_{F,G}$, the dashed solid line the non-ergodicity parameter $\Delta_{ne} \approx 1.1$ and the vertical arrow the corresponding crossover time $\tau_{ne} \approx 800$. The thin horizontal line marks the shoulder expected to matter for $\delta\mu_{F,int} \approx \delta\mu_{F,G}$ for much larger $\Delta t$ due the logarithmic creep of $G(t)$.

temperatures. As shown by the upper thin line in Fig. 4-9, $G(t)$ is fitted by a logarithmic creep. The amplitude $b$ of the low-$T$ creep is, however, too small to lead to a clear shoulder. As seen by the lower thin solid line in Fig. 7-4 using $b = 0.11$ for $T = 0.05$ at least one decade longer production runs are required to demonstrate the low-$T$ creep for $\delta\mu_{F,G}$.

Focusing on *film1* and the lowest temperature $T = 0.05$ we compare $\mu_F$, $\delta\mu_{F,tot}$ and $\delta\mu_{F,G}$ and, in addition to this, also the internal standard deviation $\delta\mu_{F,int}$ characterizing the average fluctuation within each meta-basin. In agreement with Eq. A.25 we compute $\delta\mu_{F,int}$ by first computing the variance of $\mu_F[\mathbf{x}_{ck}]$ over $N_k$ time series of length $\Delta t$ of a given configuration $c$ and by taking in a second step the ensemble average over the $N_c$ configurations. As explained at the end of Sec. 3.6 $N_k$ and $\Delta t$ are related by $N_k = \Delta t_{max}/\Delta t$, i.e. the precision of $\delta\mu_{F,int}(\Delta t)$ decreases with $\Delta t$. Only data for $N_k > 2$ are shown. Importantly, it is seen that $\delta\mu_{F,int} \approx \delta\mu_{F,G}$ for all $\Delta t$ in agreement with Eq. A.32. This confirms that the stochastic process within each basin is stationary and Gaussian. As shown by the crosses, the shifting of $\delta\mu_{F,int}$ or $\delta\mu_{F,G}$ by the plateau value $\Delta_{ne}$ according to Eq. 2.53 leads to a reasonable approximation of $\delta\mu_{F,tot}$.

## 7.5   Major results

The relaxation function $G(t)$ and the generalized shear modulus $\mu(\Delta t)$ are characterized by strong fluctuations, especially around the $T_{\mathrm{g}}$. We showed that these fluctuation can be understood assuming stationary Gaussian stochastic processes [69, 70, 77]. Specifically,

- $\delta h(t)^2 \approx 2h(t)^2$ holds to high precision as expected for Gaussian processes (Eq. 2.34);

- $\delta \mu_{\mathrm{F,int}} \approx \delta \mu_{\mathrm{F,G}}$ for all $\Delta t$ and $T$ confirming Eq. A.32;

- $\delta \mu_{\mathrm{F,tot}} \approx \delta \mu_{\mathrm{F,G}}$ for low $\Delta t$ and not too small $T$ showing that the non-monotonic behavior of $\delta \mu_{\mathrm{F,tot}}(T)$ can be traced back to the behavior of $h(T)$.

- $\delta \mu_{\mathrm{F,tot}}$ and $\delta \mu_{\mathrm{F,G}}$ differ in the non-ergodic limit for low temperatures. For large $\Delta t$, $\delta \mu_{\mathrm{F,tot}}$ becomes a constant $\Delta_{\mathrm{ne}} > 0$ and $\delta \mu_{\mathrm{F,G}} \sim 1/\sqrt{\Delta t}$ (Eq. 2.44);

- deviations from the $1/\sqrt{\Delta t}$-decay for $\delta \mu_{\mathrm{F,G}} \approx \delta \mu_{\mathrm{F,int}}$ are observed which are traced back to the creep-like decay of $G(t)$ as discussed in Appendix A.3.

This page intentionally left blank.

# Chapter 8

# Conclusion

## 8.1 Summary

In this PhD work, we numerically characterized various mechanical and rheological properties of freestanding polymer films of varying thicknesses $H$. This was done within linear response without applying external perturbations using the internal (shear) stress fluctuations of our systems. Specifically, we have focused on the average shear-stress relaxation function $G(t)$ and the average generalized modulus $\mu(\Delta t)$ and their respective standard deviations $\delta G(t)$ and $\delta\mu(\Delta t)$. Interestingly, it was seen that $G(t)$ and $\mu(\Delta t)$ increase *continuously* with decreasing $T$ for all $H$, without any indication of the suggested jump-singularity [106, 125–129] but in perfect agreement with all published experimental [15, 19, 20] and computational [43, 44] studies. We presented four main aspects concerning our films in this thesis, highlighted previously in Fig. 1-3 and summarized in the following paragraphs.

**Calculation of the response function $G(t)$ and a generalized shear modulus $\mu(\Delta t)$:** Using the stress fluctuation formalism, we calculated the shear modulus for a wide range of temperatures and thicknesses. Importantly, we noticed a clear $1/H$-dependence for these properties and related observables, such as the shear viscosity $\eta$. We also obtained a successful TTS scaling and extracted from this, the $\tau_\alpha$ and $\eta$ for our films (Ch. 4). This work is part of the published journal article in Ref. [68].

**Numerical transformation of $G(t)$:** We used numerical methods to obtain from $G(t)$ the storage modulus $G'(\omega)$ and the loss modulus $G''(\omega)$. We got for the highest temper-

ature the shear viscosity $\eta$ and steady-state creep compliance $J_e^0$ from the low-frequency asymptotes, Eq. 2.22, of $G'(\omega)$ and $G''(\omega)$. This determines the relaxation time $\tau_{\alpha,1} = J_e^0\eta$ for $T = 0.55$ which is used as a reference (scale) for the terminal relaxation time $\tau_\alpha(T)$ obtained by means of the TTS scaling. Interestingly, the crossing time $\tau_\times(\lambda = 3)$ obtained from the first crossing of $\lambda G'(\omega)$ and $G''(\omega)$ gives a direct (without TTS scaling) and numerically reliable estimate of $\tau_\alpha$ above $T_g$ (Sec. 5.3). We also performed a direct transformation of $G(t)$ to obtain the creep compliance $J(t)$. This allowed for a comparison with the compliance measured in the nanobubble inflation experiment [19] (Ch. 5). We also saw here a limitation of our model parameter $N \ll N_e$ and the associated absence of a rubbery plateau.

**Calculation of the local shear modulus from the stress fluctuation formalism:** We calculated the layer-resolved shear modulus $\mu(z)$ and related properties in Ch. 6. Conforming with various other experimental and computational studies [24, 43, 56, 75, 76], we verified the presence of a *soft* film interface, manifested by the drop in shear modulus at the surface ($z \approx H/2$) relative to the center of the film. It was also seen that the width of the soft surface region at the interface grows with $T$. In the high-$T$ limit, $\mu(z)$ was seen to vanish ($\mu(z) \approx 0$) as expected. The key results emerging from this provides compelling evidence on the linear $1/H$-dependency of global film properties, arising from the local $z$-resolved contributions, and in support of the two-layer model [56].

**Calculation of ensemble fluctuations of the response function and the shear modulus:** After observing that the fluctuations of $G(t)$ were of the same order as that of its means (especially around $T_g$), we tried to explain the origins and various contributions of these fluctuations (Ch. 7). We found that $\delta G(t) \approx \delta h(t) \approx \sqrt{2}h(t)$ and $\delta\mu \approx \delta\mu_F(\Delta t)$, as the affine Born-Lamé contribution $\delta\mu_A \approx 0$. We also saw that a system in its *internal basin* is characterized by Gaussian fluctuations $\delta\mu_{F,G} \approx \delta\mu_{F,int}$. We also saw that the total ensemble fluctuation $\delta\mu_{F,tot}$ and $\delta\mu_{F,G}$ differ in the non-ergodic limit for low-$T$. It was seen that for large $\Delta t$ and low-$T$, $\delta\mu_{F,tot}$ becomes a constant $\Delta_{ne} > 0$ and $\delta\mu_{F,G} \sim 1/\sqrt{\Delta t}$. The theoretical concepts developed in this regard (Ch. 2) should be useful in general and applicable for a broad range of stationary Gaussian stochastic processes in many area of condensed matter physics. This work was part of a collaborative, group-wide study which
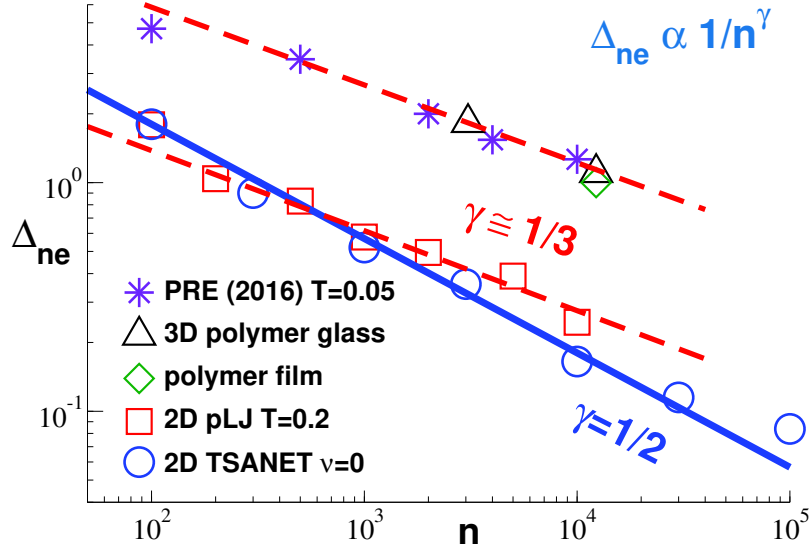
Figure 8-1: Logarithmic representation of $\Delta_{\mathrm{ne}}$ as a function of the number of particles $n \approx V$ for various systems. The TSANET model at $\nu$ (frequency of switching) $= 0$ (circles) [69], for the 2DpLJ model (squares) at $T = 0.20$ [118], for *film1* (diamonds) at $T = 0.05$, for 3D polymer glass (triangles) at $T \approx 0.10$ [77], and for a binary LJ mixture at $T = 0.05$ (stars) [118]. Here, $\gamma$ is the power law exponent for the $\Delta_{\mathrm{ne}}$ parameter.

was recently published [69]. A followup article [70] focusing on the low-temperature non-ergodic limit (as outlined in Sec. 2.6 and Sec. A.5-A.7) has also been published.

## 8.2 Perspectives

Our work on freestanding polymer films does not by any means provide a full picture. There are certainly areas that can be improved and there are different avenues that one can still pursue. A few of these can already be identified:

- Simulations with $N \gg N_e$ are necessary for multiple reasons. The dynamic processes discussed here are expected to behave closer to experimental results reported in Ref. [19] for a larger $N$, allowing for more comparisons. The entanglement assisted slowdown in relaxation will also confirm for us the presence of a rubbery plateau for the creep compliance $J(t)$.

- In this thesis, we imposed the lateral box width $L$ in an equilibrium simulation to indirectly measure the creep compliance (transformed from $G(t)$ calculated using the shear-stress fluctuation formalism). Another approach to do this would be to perform

an explicit out-of-equilibrium simulation where one applies a constant infinitesimal strain in the $xy$ plane to measure $G(t)$ or a constant infinitesimal stress in both $x$ and $y$ plane to measure the biaxial compliance $D(t)$ as in experiments.

- It would be interesting to explore other polymer architectures. An experimental study by the Drenckhan group (ICS, Strasbourg) showed that a commercially available comb copolymer, DBP732 – made of a long silicon backbone (PDMS) and multiple PEG-PPG branching sites, has the potential to form extremely stable free standing thin films ($10 - 150$nm) without the use of additional stabilizing agents [50]. The working hypothesis was that this effect originated due to a stiff interface (contrary to the *soft* interface formed by linear chains in this thesis). A preliminary attempt was made in this direction during the course of my PhD, based on a coarse-grained bead-spring model with $N = 32$ and varied branch-backbone interaction parameters, but we were not able to observe the anticipated interface stiffness. Further work is required to address the intricacies of this interesting phenomenon.

- In our simulations, we focused also on the variation of $\Delta t$ and $T$ while keeping other parameters such as the total number of particles in the system $n = N \times M \approx V$ fixed. Most properties discussed in this work $\mu_{\mathrm{A}}$, $\mu_{\mathrm{F}}$, $\mu$ or $h(t)$ are defined as intensive properties, and their mean values *should not* essentially depend on the system size $n$ or the volume $V$. This aspect has to be verified for our films. (Perhaps by taking $4 \times M$ and a corresponding increase in $L \to 2 \times L$ to maintain the film geometry.)

- In addition, a recent study conducted in our group on the standard deviations of the above mentioned properties for other model systems – Transient self assembled networks (TSANET) and 2D-polydispersed LJ beads (2DpLJ) – have emphasized that there is a non-trivial system size dependency for non-ergodic systems [69, 70]. As readily seen from Fig. 8-1, where we compare the system-size dependency for various model systems, there is only a single data point corresponding to our freestanding film system (*film1*). Therefore, it would be interesting to verify/understand how $\Delta_{\mathrm{ne}}(n)$ behaves for our films. Our working hypothesis is that it will behave similar to the 3D polymer glass system, shown in Fig. 8-1.

- As a final note, our claim that $\delta G/G$ or $\delta \mu/\mu$ must generally become large (of or-

der unity) for times where $G(t)$ strongly decays and that these ratios are, more-over, system-size independent may in fact be misleading for the out-of-equilibrium responses of real macroscopic materials. From the theoretical point of view it is an interesting question how to generalize the fluctuation-dissipation relations, connecting the *average* linear out-of-equilibrium response to the *average* equilibrium relaxation [3, 101, 105], to describe the sample-to-sample fluctuations.

# Appendices

This page intentionally left blank.

# Appendix A

# More on time series of stationary Gaussian stochastic processes

## A.1 Reformulations of $\delta v_G[c]$

Since for large $I$ the sums over two, three or even four indices stated in Sec. 2.5.3 by Eqs. 2.37-2.38 rapidly become numerically unfeasible, it is of importance that the three terms $T_2$, $T_4$ and $T_3$ of Eq. 2.35 can be simplified to single loops [77]. The first two terms simply become

$$T_2(\Delta t) = \frac{2}{I^2} \left( I c_0^2 + 2 \sum_{k=1}^{I-1} (I-k) c_k^2 \right) \tag{A.1}$$

$$T_4(\Delta t) = \frac{2}{I^4} \left( I c_0 + 2 \sum_{k=1}^{I-1} (I-k) c_k \right)^2 . \tag{A.2}$$

Let us define the sum $S(s,I) \equiv \sum_{i=1}^{I} c_{i-s}$. Note that $S(s,I)$ may be computed starting from $S(0,I)$ using the recursion relation $S(s+1,I) = S(s,I) + c_s - c_{I-s}$. Using this the calculation of

$$T_3(\Delta t) = \frac{4}{I^3} \sum_{s=1}^{I} S(s,I)^2 = \frac{8}{I^3} \sum_{s=1}^{I/2} S(s,I)^2 \tag{A.3}$$

becomes also of order $\mathcal{O}(I)$. Using the symmetry $S(s,I) = S(I-s+1,I)$ we have assumed in the last step that $I$ is even. In the continuum limit for large $I = \Delta t/\delta t$ the three terms

further simplify to

$$T_2(\Delta t) = \frac{4}{\Delta t^2} \int_0^{\Delta t} dt \ (\Delta t - t)c(t)^2 \tag{A.4}$$

$$T_4(\Delta t) = \frac{8}{\Delta t^4} \left( \int_0^{\Delta t} dt \ (\Delta t - t)c(t) \right)^2 \tag{A.5}$$

$$T_3(\Delta t) = \frac{8}{\Delta t^3} \int_0^{\Delta t/2} dt \ (\eta(t) + \eta(\Delta t - t))^2 \tag{A.6}$$

using $\eta(t) \equiv \int_0^t du \ c(u)$ for the last contribution.

## A.2   Some general properties of $\delta v_G[c]$

Assuming a constant ACF $c(t) = a$ one obtains from either Eqs. 2.37, 2.38, 2.39 or using the corresponding continuum relations that

$$2T_2 = 2T_4 = T_3 = 4a^2, \tag{A.7}$$

i.e. $\delta v_G^2 = T_2 + T_4 - T_3$ must vanish in agreement with Eq. 2.41. This is of relevance for very short sampling times $\Delta t$ where $c(t) \approx c(0) = c_0$ or if $c(t)$ shows an intermediate plateau extending over several order of magnitudes as is the case for our low-temperature films, Ch. 4. The summand $g_{ijkl}^2$ in Eq. 2.40 must remain small, if $c(t)$ is not rigorously, but only nearly constant. The typical summand $g^2$ can be estimated by the typical slope on logarithmic time scales [77]

$$g(\Delta t) \approx c(\Delta t) - c(\Delta t/2) \approx dc(t)/d\log(t))|_{t \approx \Delta t} . \tag{A.8}$$

One thus expects

$$\delta v_G^2[c] \approx \sum_{ijkl} g_{ijkl}^2 / I^4 \approx g(\Delta t)^2. \tag{A.9}$$

For instance, $c(t)$ may decrease for $t \ll \tau_\alpha$ as $c(t) \approx b \exp(-(t/\tau_\alpha)^\beta) + c_\infty$ with constants $\beta > 0$. Equations A.8 and A.9 then lead to

$$\delta v_G[c] \approx |b|(\Delta t/\tau_\alpha)^\beta \text{ for } \Delta t \ll \tau_\alpha. \tag{A.10}$$

In the opposite limit of very large $\Delta t \gg \tau_\alpha$, the leading scaling dependence is obtained by replacing in Eqs. A.4-A.6 the upper integration bounds by $\tau_\alpha$ and $c(t)$ by $a \approx c(\tau_\alpha) - c_\infty$ using Eq. 2.41. This implies

$$T_2 \approx a^2 \ \tau_\alpha/\Delta t, T_4 \approx T_3 \approx a^2 \ (\tau_\alpha/\Delta t)^2. \tag{A.11}$$

In other words, $\delta v_G^2$ is dominated for $\Delta t/\tau_\alpha \gg 1$ by $T_2 = \delta m_{21}^2$, i.e. $\delta v_G \propto 1/\sqrt{\Delta t}$ as expected for $\Delta t/\tau_\alpha$ uncorrelated sub-intervals. Adding heuristically the short and the long time behavior, Eq. A.9 and Eq. A.11, yields the phenomenological approximation,

$$\delta v_G^2[c] \approx g(\Delta t)^2 + (c(\tau_\alpha) - c_\infty)^2 \ (\tau_\alpha/\Delta t) \tag{A.12}$$

which is useful for processes with one main dominant relaxation process.

## A.3 $\delta v_G[f]$ for some simple test functions $f(t)$

### Introduction

To illustrate some useful properties of the non-linear functional $\delta v_G[f]$ we discuss now several test functions $f(t)$. Not all presented $f$ belong to the space of legitimate ACFs $c$ or $h$ of stationary stochastic processes. We remind [105, 106] that a legitimate ACF may not change too strongly (especially not discontinuously) and must not violate the Wiener-Khinchin theorem on the power spectrum of the signal stating that the Fourier transform (FT) of $c(t)$ is given by the squared FT of $x(t)$. A general (necessary and sufficient) criterion for a function $f(t)$ to be a legitimate ACF[38] is thus [105, 106]

$$\hat{f}(\omega) \equiv \int_0^\infty f(t) \cos(\omega t) \mathrm{d}t \geq 0 \text{ for any real } \omega. \tag{A.13}$$

This ensures that $f(0) \geq |f(t)| \geq 0$ and $\hat{f}(\omega = 0) = \int_0^\infty \mathrm{d}t f(t) \geq 0$. Taking advantage of the affine transform Eq. 2.41 we often set without loss of generality $f(0) = 1$ and $f(t) \to 0$ for $t \to \infty$. If there is only one characteristic time it is also set to unity.

---

[38]According to Bochner's theorem $\hat{f}(\omega) \geq 0$ if and only if $f(t)$ is a positive-definite function, i.e. all eigenvalues of the matrix $g_{i,j} = f(t_i - t_j)$ are non-negative [106].
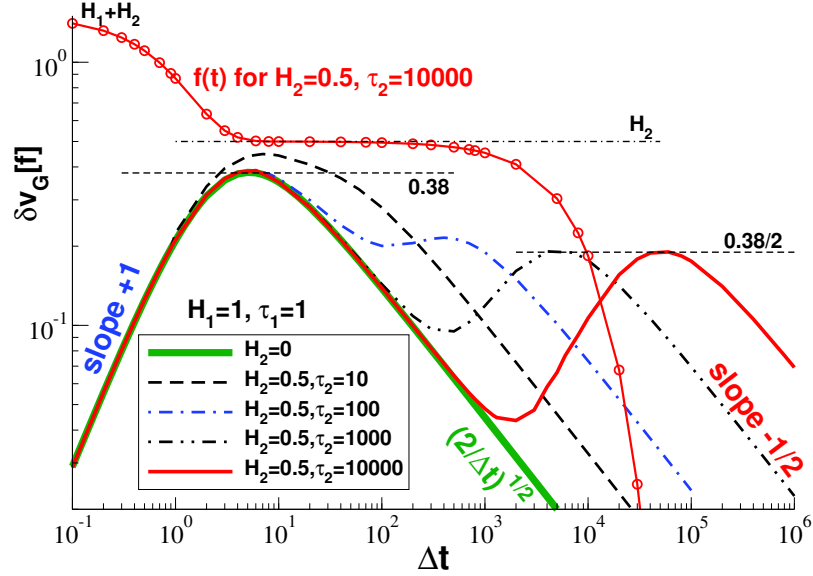
Figure A-1: $\delta v_{\mathrm{G}}[f]$ *vs.* $\Delta t$ for the one-mode Maxwell model with $H_1 = \tau_1 = 1$ (bold solid line) revealing a maximum at $\Delta t \approx 5$ and a final decay $\delta v_{\mathrm{G}} \approx \sqrt{2/\Delta t}$. The other data refer to the two-step relaxation model Eq. A.15 with $H_2 = 0.5$. Also given is $f(t)$ for $\tau_2 = 10000$ (solid line with circles). $\delta v_{\mathrm{G}}[f]$ becomes bimodal with increasing $\tau_2/\tau_1$ with a minimum slightly below $\tau_2$ and a second separate maximum at $\approx 5\tau_2$.

## Maxwell model

One of the few cases where $\delta v_{\mathrm{G}}[f]$ can be calculated analytically is the Maxwell model (Debye decay) $f(t) = \exp(-t)$. This model is especially of relevance for the self-assembled network systems (TSANET) [101] investigated in Refs. [69, 70]. Since $\hat{f}(\omega) = 1/(1+\omega^2) > 0$ for all $\omega$, $f(t)$ is a legitimate ACF as expected. Note first that $v(\Delta t) = 1 - g_{\mathrm{Debye}}(\Delta t)$ with $g_{\mathrm{Debye}}(\Delta t)$ being the Debye function introduced in Sec. 2.4.6. The three contributions $T_2$, $T_4$ and $T_3$ to $\delta v_{\mathrm{G}}^2[f] = T_2 + T_4 - T_3$ are:

$$T_2 = 2g_{\mathrm{Debye}}(2\Delta t), \ T_4 = 2g_{\mathrm{Debye}}(\Delta t)^2, \tag{A.14}$$
$$T_3 = \frac{4}{\Delta t^3} \times \left[ -e^{-2\Delta t} + (2\Delta t + 8)e^{-\Delta t} + 4\Delta t - 7 \right]$$

Since $g_{\mathrm{Debye}}(x) \approx 2/x$ for large $x$ we have $\delta v_{\mathrm{G}} \approx \sqrt{2/\Delta t}$ for large $\Delta t$. The analytical solution for the Maxwell model is indicated by a bold solid line in Fig. A-1. This exact result may be used for testing the numerical determination of $\delta v_{\mathrm{G}}[f]$ by means of Eqs. A.4, A.5 and A.6.

## Generalized Maxwell model

We now discuss an example for systems with *two* relaxation processes similar to Fig. 2-1. Of interest is the limit where $f(t)$ develops an intermediate plateau $f(t) \approx f_p$ for $\tau_1 \ll t \ll \tau_2$ with $\tau_1$ corresponding to a fast, local process and $\tau_2$ to a slow, collective relaxation. One expects $\delta v_G(\Delta t)$ to become bimodal with a first maximum around $\tau_1$ followed by a $1/\sqrt{\Delta t}$-decay and a second maximum around $\tau_2$ followed by a second $1/\sqrt{\Delta t}$-decay. The minimum between both maxima should systematically become deeper with increasing plateau width. We present in Fig. A-1 numerically obtained $\delta v_G[f]$-data assuming

$$f(t) = H_1 \exp(-t/\tau_1) + H_2 \exp(-t/\tau_2) \qquad (A.15)$$

with $H_1 = \tau_1 = 1$ and $H_2 = 0.5$ for the amplitude of the second mode. As for all generalized Maxwell models we have $\hat{f}(\omega) = \sum_p H_p \tau_p / (1 + (\omega \tau_p)^2) > 0$, i.e. Eq. A.15 is a legitimate ACF. We scan $\tau_2$ over several orders of magnitude as indicated in the figure. We indicate $f(t)$ for the longest second relaxation time, $\tau_2 = 10000$, at the top of the figure (solid line with circles). For large $\tau_2/\tau_1$ one observes for $\delta v_G(\Delta t)$ two well separated maxima of same shape but different amplitudes $\propto H_p$. Note that the ratio of the two dashed horizontal lines is $H_1/H_2 = 2$. The decay from both maxima is given by $\delta v_G \approx H_p \sqrt{2\tau_p/\Delta t}$.

## Stretched and compressed exponentials

Another natural generalization of the one-mode Maxwell model ($\beta = 1$) is seen in Fig. A-2 where we present $\delta v_G[f]$ for $f(t) = f_\beta(t) \equiv \exp(-t^\beta)$. $f_\beta(t)$ is a "stretched" exponential for $\beta < 1$ and a "compressed" exponential for $\beta > 1$. It can be readily checked numerically that Eq. A.13 only holds for $\beta \leq 2$ but not for larger exponents $\beta$ which do <u>not</u> correspond to ACF of stationary stochastic processes. To see this let us just mention two cases. Since $\hat{f}(\omega) \propto \exp(-\omega^2/4)$ for $\beta = 2$, Eq. A.13 holds for the Gaussian model and it thus also does for even more gently decreasing (less compressed) functions with $\beta < 2$. On the other side $f_\beta(t)$ becomes for $\beta \to \infty$ equivalent to the cusp singularity $f_{\text{cusp}}(t) \equiv H(t) - H(t-1)$. ($\delta v_G[f_{\text{cusp}}]$ can be readily calculated analytically and this exact formula is used in Fig. A-2.) The cusp singularity is not a legitimate ACF since $\hat{f} = \sin(\omega)/\omega$, i.e. Eq. A.13 does not hold. As may be seen from the main panel, all $\delta v_G[f_\beta]$ have a maximum between $\Delta t \approx 4$
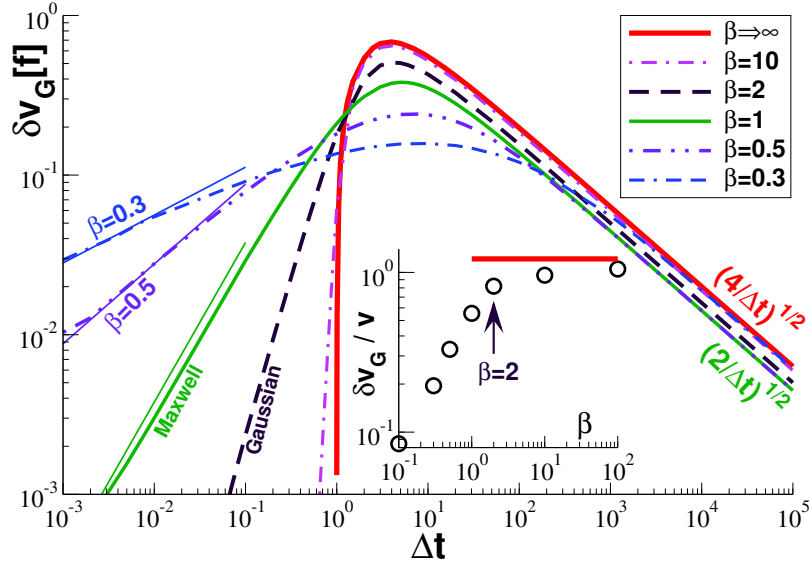
Figure A-2: $\delta v_{\mathrm{G}}[f]$ *vs.* $\Delta t$ for $f(t) = f_\beta(t) \equiv \exp(-t^\beta)$ with $\beta = 1$ corresponding to the one-mode Maxwell model, $\beta = 2$ to a Gaussian and $\beta \to \infty$ to the cusp model $f_{\mathrm{cusp}}(t) \equiv H(t) - H(t-1)$. Only exponents $\beta \leq 2$ correspond to legitimate ACFs. Note that $\delta v_{\mathrm{G}} \propto \Delta t^\beta$ for $\Delta t \ll 1$ (thin solid lines for $\beta = 0.3$, $0.5$ and $1$) and $\delta v_{\mathrm{G}} \propto 1/\sqrt{\Delta t}$ for $\Delta t \gg 1$. Inset: $\delta v_{\mathrm{G}}/v|_{\mathrm{max}}$ *vs.* $\beta$. The vertical arrow marks the ratio $\approx 0.82$ for $\beta = 2$, the horizontal line the ratio $\approx 1.21$ for $\beta \to \infty$.

(large $\beta$) and $\Delta t \approx 10$ (small $\beta$). As expected from $f_\beta(t) \to f_{\mathrm{cusp}}(t)$ for $\beta \to \infty$, it is seen that $\delta v_{\mathrm{G}}(\beta)$ becomes increasingly similar to the standard deviation of the cusp model (bold solid line), i.e. the peaks become systematically higher, sharper and more lopsided with increasing $\beta$. The power-law slopes $\beta$ (thin solid lines) observed for $\Delta t \ll 1$ are expected from Eq. A.10. All models decrease as $\delta v_{\mathrm{G}} \approx \sqrt{a/\Delta t}$ for large $\Delta t$ in agreement with Eq. A.11. The amplitude $a$ of this ultimate decay is the *largest* for the cusp model ($a = 4$) and the *smallest* for the Maxwell model ($a = 2$). The inset of Fig. A-2 shows the ratio $\delta v_{\mathrm{G}}/v|_{\mathrm{max}}$ taken at the maximum of $\delta v_{\mathrm{G}}(\Delta t)$ for a broad range of the exponent $\beta$. This shows a monotonic increase with $\beta$ approaching from below the ratio $\approx 1.21$ of the cusp model (bold horizontal line). The ratio is $\approx 0.55$ for the Maxwell model and $\approx 0.82$ for the Gaussian (vertical arrow). Importantly, the standard deviations thus become of the same order as the average behavior for the most rapidly decaying legitimate ACFs with $\beta \leq 2$.

## Logarithmic creep

Logarithmically slow varying ACFs are expected for hopping processes in systems with a broad distribution of barriers and are generally observed in glass-forming fluids [1, 105, 106].
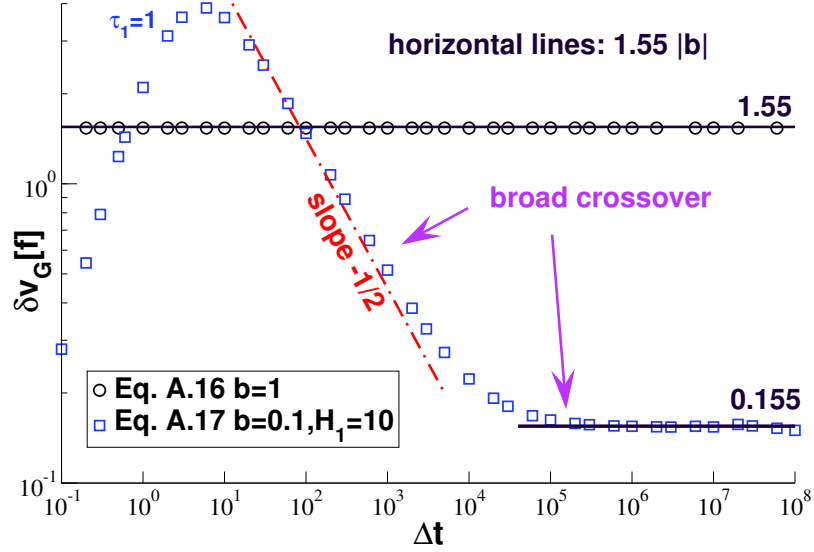
Figure A-3: $\delta v_{\mathrm{G}}[f]$ *vs.* $\Delta t$ for logarithmic creep. The circles indicate Eq. A.16 for $b = 1$, the squares Eq. A.17 for $H_1 = 10$, $\tau_1 = \tau_2 = 1$, $b = 0.1$ and $\tau_3 = 10^{10}$ and the dash-dotted line the $1/\sqrt{\Delta t}$-decay of the short-time Maxwell model. The arrows emphasize the broad crossover between the Maxwell model and the plateau expected for $b = 0.1$.

The general scaling relation Eq. A.9 suggests

$$\delta v_{\mathrm{G}}[f] \approx 1.55|b| \text{ if } f(t) \approx a - b\ln(t) \tag{A.16}$$

holds over a sufficiently broad intermediate time window. The indicated prefactor 1.55 is needed for the discussion of $\delta v_{\mathrm{G}}(\Delta t)$ in Ch. 7. Obviously, this value is not given by the scaling relation but by numerically computing $\delta v_{\mathrm{G}}[\ln(t)]$ as shown by circles in Fig. A-3. Due to the affinity relation Eq. 2.41, this result corresponds to an amplitude $b = 1$ and does not depend on the shift constant $a$. Obviously, a legitimate ACF cannot diverge for $t \to 0$ and $t \to \infty$ and $f(t) = a - b\ln(t)$ cannot hold in these limits for both mathematical and physical grounds. To demonstrate that Eq. A.16 may hold for an intermediate time window of a legitimate ACF we are thus free to use, e.g., a generalized Maxwell model, Eq. 2.25, fitted (by inverse Laplace transformation [146]) to an intermediate logarithmic creep. (As noted above, this yields directly a legitimate ACF.) More simply we may improve $f(t) = a - b\ln(t)$ by adding suitable continuous cutoffs. As shown by the squares in Fig. A-3 we use

$$f(t) = H_1 e^{-t/\tau_1} + a - b\ln(t)\,(1 - e^{-t/\tau_2})\,e^{-t/\tau_3} \tag{A.17}$$

101

with $H_1 = 10$ and $\tau_1 = 1$ for the Maxwell model added to mimic the typical microscopic relaxation and $\tau_2 = 1$ and $\tau_3 = 10^{10}$ setting, respectively, the lower and the upper cutoff of the logarithmic creep. ($\tau_3$ is irrelevant for the presented $\Delta t$-range and the constant $a$ is arbitrary.) The strong Maxwell mode dominates $\delta v_{\rm G}(\Delta t)$ below $\Delta t \approx 10^3$. Interestingly, as marked by the left arrow deviations from the $1/\sqrt{\Delta t}$-decay (dash-dotted line) expected for the Maxwell mode are already seen at $\Delta t \approx 10^2$. After a broad crossover regime (about three decades) a plateau (solid horizontal line) is observed confirming Eq. A.16. Importantly, the latter model demonstrates how a rather small additional logarithmic creep may lead to strong deviations from an expected $1/\sqrt{\Delta t}$-decay.

## A.4 Additional notations for non-ergodic systems

We give now additional details on non-ergodic stochastic processes which are relevant for our films at low temperatures $T \ll T_{\rm g}$. This requires additional notations. The $l$-average operator

$$\mathbf{E}^l \mathcal{O}_{lmn\ldots} \equiv \frac{1}{N_l} \sum_{l=1}^{N_l} \mathcal{O}_{lmn\ldots} \equiv \mathcal{O}_{mn\ldots}(N_l) \tag{A.18}$$

takes a property $\mathcal{O}_{lmn\ldots}$ depending possibly on several indices $l, m, \ldots$ and projects out the specified index $l$, i.e. the generated property $\mathcal{O}_{mn\ldots}(N_l)$ does not depend any more on $l$, but it may depend on the upper bound $N_l$ as marked by the argument. The latter dependence drops out for large $N_l$ (formally $N_l \to \infty$) if the sum converges. The $l$-variance operator $\mathbf{V}^l$ is defined by

$$\mathbf{V}^l \mathcal{O}_{lmn\ldots} \equiv \frac{1}{N_l} \sum_{l=1}^{N_l} \left( \mathcal{O}_{lmn\ldots} - \mathbf{E}^l \mathcal{O}_{lmn\ldots} \right)^2. \tag{A.19}$$

Introducing the power-law operator $\mathbf{P}^\alpha \mathcal{O} \equiv \mathcal{O}^\alpha$, with the exponent $\alpha = 2$ being here the only relevant case, and using the standard commutator $[\mathbf{A}, \mathbf{B}] \equiv \mathbf{AB} - \mathbf{BA}$ for two operators $\mathbf{A}$ and $\mathbf{B}$, the $l$-variance operator may also be written $\mathbf{V}^l = [\mathbf{E}^l, \mathbf{P}^2]$.

## A.5 Extended ensembles of time series $\mathbf{x}_{ck}$

We remind that for ergodic systems [105, 106] one may either compute the averages $\mathbf{E}^c \mathcal{O}[\mathbf{x}_c]$ and $\mathbf{V}^c \mathcal{O}[\mathbf{x}_c]$ over independent configurations $c$ or the averages $\mathbf{E}^k \mathcal{O}[\mathbf{x}_k]$ and $\mathbf{V}^k \mathcal{O}[\mathbf{x}_k]$ over
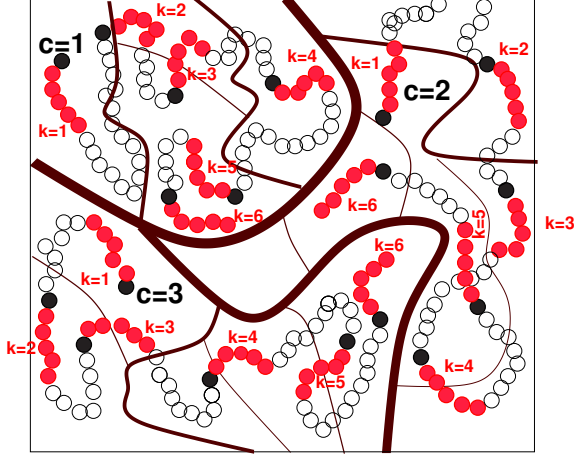
Figure A-4: Time series $\mathbf{x}$ with $N_t = 6$ data entries $x_i$ are marked by filled circles. The first entry $x_{i=1}$ is indicated by a dark filled circle. The open circles mark tempering steps between different time series $k$ of each *independently* prepared configuration $c$. Each of the $N_c = 3$ configurations corresponds to $N_k = 6$ time series. The solid lines mark barriers of different height in some phase space. We assume that the system is non-ergodic, i.e. the stochastic processes of different configurations $c$ are permanently trapped in the meta-basins marked by the thickest lines.

different time series $k$ of one long trajectory and that

$$\mathbf{E}^c \mathcal{O}[\mathbf{x}_c] \approx \mathbf{E}^k \mathcal{O}[\mathbf{x}_k] \text{ and } \mathbf{V}^c \mathcal{O}[\mathbf{x}_c] \approx \mathbf{V}^k \mathcal{O}[\mathbf{x}_k] \tag{A.20}$$

holds for sufficiently large $N_c$ and $N_k$. Let us focus now on strictly non-ergodic systems. We characterize a time series $\mathbf{x}_{ck}$ by *two* discrete indices with $1 \leq c \leq N_c$ and $1 \leq k \leq N_k$. As shown in Fig. A-4, the index $c$ stands for the *configurations* generated by completely independent preparation histories for the system probed, the index $k$ for subsets of length $N_t$ of a much larger trajectory generated for a fixed configuration $c$. Crucially,

$$\mathcal{O}_c(\Delta t, N_k) \equiv \mathbf{E}^k \mathcal{O}[\mathbf{x}_{ck}] \text{ and} \tag{A.21}$$

$$\delta \mathcal{O}_c^2(\Delta t, N_k) \equiv \mathbf{V}^k \mathcal{O}[\mathbf{x}_{ck}] \tag{A.22}$$

do depend in general not only on the sampling time $\Delta t$ of the time series and the number $N_k$ of time series probed but also on $c$ — even for arbitrarily large $N_t$ and $N_k$ — since each $c$-trajectory is confined in a basin. For sampling times $\Delta t \gg \tau_b$ larger than the typical relaxation time $\tau_b$ of the basins the $\Delta t$-dependence of $\mathcal{O}_c(\Delta t, N_k)$ must drop out and

$\delta\mathcal{O}_c(\Delta t, N_k) \propto 1/\sqrt{\Delta t/\tau_b}$ since we average over $\Delta t/\tau_b$ independent subintervals. Moreover, the $N_k$-dependence must disappear if the $c$-trajectory has completely explored the basin. Assuming that after each measurement interval of length $\Delta t$ a spacer (tempering) step of length $\Delta t_{\text{spac}}$ follows, this will happen for trajectories of total length $\Delta t_{\text{max}} \equiv N_k \times (\Delta t + \Delta t_{\text{spac}}) \gg \tau_b$. Since $[\mathbf{E}^c, \mathbf{E}^k] = 0$ we may write quite generally,

$$\mathbf{E}^c\mathbf{E}^k \ \mathcal{O}[\mathbf{x}_{ck}] = \mathbf{E}^k\mathbf{E}^c \ \mathcal{O}[\mathbf{x}_{ck}] = \mathbf{E}^l \ \mathcal{O}[\mathbf{x}_l] = \mathcal{O}, \tag{A.23}$$

i.e. the two indices $c$ and $k$ can be lumped together to one index $l$. Averages of this type also called *simple averages*, similar to the ones introduced in Sec. 2.2. We define now in general terms the three variances already mentioned Sec. 2.6

$$\delta\mathcal{O}^2_{\text{tot}} \equiv \mathbf{V}^l\mathcal{O}[\mathbf{x}_l] \equiv [\mathbf{E}^c\mathbf{E}^k, \mathbf{P}^2]\mathcal{O}[\mathbf{x}_{ck}] \tag{A.24}$$

$$\delta\mathcal{O}^2_{\text{int}} \equiv \mathbf{E}^c\delta\mathcal{O}^2_c = \mathbf{E}^c\mathbf{V}^k\mathcal{O}[\mathbf{x}_{ck}] \tag{A.25}$$

$$\delta\mathcal{O}^2_{\text{ext}} \equiv \mathbf{V}^c\mathcal{O}_c = \mathbf{V}^c\mathbf{E}^k\mathcal{O}[\mathbf{x}_{ck}]. \tag{A.26}$$

Note that the total variance $\delta\mathcal{O}^2_{\text{tot}}$ is a simple average, i.e. all time series $\mathbf{x}_{ck}$ can be lumped together. Importantly, its expectation value for $N_c \to \infty$ is strictly $N_k$-independent and may be also computed by using only *one* time series for each configuration ($N_k = 1$). $\delta\mathcal{O}^2_{\text{tot}}$ is thus the standard commonly computed variance [65, 67–69, 77, 101, 118]. That $\delta\mathcal{O}_{\text{int}}$ and $\delta\mathcal{O}_{\text{ext}}$ are a quite different observables can be seen from the fact that $\mathbf{E}^c$ and $\mathbf{E}^k$ cannot be interchanged (commuted) if $N_k > 1$. $\delta\mathcal{O}_{\text{ext}}$ only vanishes if all $\mathcal{O}_c$ are identical. Using

$$\mathbf{V}^l = [\mathbf{E}^c\mathbf{E}^k, \mathbf{P}^2] = \mathbf{E}^c\mathbf{E}^k\mathbf{P}^2 - \mathbf{E}^c\mathbf{P}^2\mathbf{E}^k + \mathbf{E}^c\mathbf{P}^2\mathbf{E}^k - \mathbf{P}^2\mathbf{E}^c\mathbf{E}^k = \mathbf{E}^c\mathbf{V}^k + \mathbf{V}^c\mathbf{E}^k \tag{A.27}$$

the total variance $\delta\mathcal{O}^2_{\text{tot}}$ can be decomposed as the sum of two *independent* variances

$$\delta\mathcal{O}^2_{\text{tot}}(\Delta t) = \delta\mathcal{O}^2_{\text{int}}(\Delta t, N_k) + \delta\mathcal{O}^2_{\text{ext}}(\Delta t, N_k) \tag{A.28}$$

with $\delta\mathcal{O}^2_{\text{int}}$ being the typical internal variance of the meta-basins and $\delta\mathcal{O}^2_{\text{ext}}$ the dispersion between the basins. Details of both contributions $\delta\mathcal{O}_{\text{int}}$ and $\delta\mathcal{O}_{\text{ext}}$ depend on the properties of the considered stochastic process $x(t)$ and the preaverage $\mathcal{O}[\mathbf{x}]$ considered. However, the following fairly general statements can be made. While $\delta\mathcal{O}_{\text{int}}$ and $\delta\mathcal{O}_{\text{ext}}$ depend in principle

on $N_k$, this dependence must drop out for large $N_k$ if $\Delta t_{\max} \gg \tau_b$ as already noted above. Note also that $\delta\mathcal{O}_{\mathrm{int}} \to 0$ and $\delta\mathcal{O}_{\mathrm{ext}} \to \delta\mathcal{O}_{\mathrm{tot}}$ in the opposite limit for $N_k \to 1$. Without additional assumptions it is also clear that for $\Delta t \gg \tau_b$ one expects

$$\delta\mathcal{O}_{\mathrm{int}} \propto 1/\sqrt{\Delta t/\tau_b}, \ \delta\mathcal{O}_{\mathrm{ext}}(\Delta t) \to \Delta_{\mathrm{ne}} = const \tag{A.29}$$

with the *non-ergodicity parameter* $\Delta_{\mathrm{ne}}$ being defined by the finite large-$\Delta t$ limit of $\delta\mathcal{O}_{\mathrm{ext}}$. As already noted, the first limit is a consequence of the $\Delta t/\tau_b$ uncorrelated subintervals for each $c$-trajectory while the second limit is merely a consequence of the $\mathcal{O}_c(\Delta t)$ becoming constant. Equation A.29 implies that $\delta\mathcal{O}_{\mathrm{tot}}$ must become

$$\delta\mathcal{O}_{\mathrm{tot}} \to \delta\mathcal{O}_{\mathrm{ext}} \approx \Delta_{\mathrm{ne}} \text{ for } \Delta t \gg \tau_{\mathrm{ne}} \gg \tau_b. \tag{A.30}$$

Note that the crossover to the $\Delta_{\mathrm{ne}}$-dominated regime occurs at an additional time scale $\tau_{\mathrm{ne}}$. Operationally, this *non-ergodicity time* $\tau_{\mathrm{ne}}$ may be defined as

$$\delta\mathcal{O}_{\mathrm{int}}(\Delta t \overset{!}{=} \tau_{\mathrm{ne}}) = \Delta_{\mathrm{ne}}. \tag{A.31}$$

We note finally that the non-ergodicity parameter $\Delta_{\mathrm{ne}}$ does not dependent on $N_k$, being equivalently the large-$\Delta t$ limit of either $\delta\mathcal{O}_{\mathrm{ext}}(\Delta t, N_k)$ or $\delta\mathcal{O}_{\mathrm{tot}}(\Delta t)$, the latter simple average being strictly $N_k$-independent ($N_c \to \infty$). We show now that the definition Eq. A.31 of the non-ergodicity time $\tau_{\mathrm{ne}}$ is consistent with the definition given in the main text Eq. 2.44.

## A.6   Properties related to $\mathcal{O}[\mathbf{x}] = v[\mathbf{x}]$

We shall focus from now on $\mathcal{O}[\mathbf{x}] = v[\mathbf{x}]$, Eq. 2.1. Eq. 2.45 follows directly from the more general relation Eq. A.28. Assuming an *ergodic* Gaussian process we have expressed $\delta v(\Delta t)$ by the functional $\delta v_G[h]$ in terms of the ACF $h$, Eq. 2.40. We make now the additional assumption that

> *after sufficient tempering the stochastic process of each configuration c in its meta-basin is both stationary and Gaussian.*

This implies that Eq. 2.40 may hold for each basin separately, i.e. $\delta v_c$ is given by $\delta v_G[h_c]$ expressed in terms of the corresponding ACF $h_c$ of the basin instead of its $c$-average $h =$

$\mathbf{E}^c h_c$. Unfortunately, $h_c$ is not known in general (at least not to sufficient accuracy), but rather $h$. Since Eq. 2.40 corresponds to products of $h_c$, it is a *mean-field type* approximation to replace $h_c$ by its $c$-average $h$. Within the above physical assumption and the additional technical approximation one thus expects after a final $c$-averaging

$$\delta v_{\text{int}}(\Delta t) \approx \delta v_{\text{G}}[h] \text{ with } h = \mathbf{E}^c h_c \tag{A.32}$$

to hold for all $\Delta t$. Whether this approximation is good enough must be checked for each case. Note that $\delta v_{\text{G}}$ does not depend on $N_{\text{k}}$ while $\delta v_{\text{int}}$ may, i.e. Eq. A.32 only holds for sufficiently large $N_{\text{k}}$. The asymptotic relations Eq. A.30 and Eq. A.32 suggest the simple interpolation

$$\delta v_{\text{tot}}(\Delta t) \approx \sqrt{\delta v_{\text{G}}^2[h] + \Delta_{\text{ne}}^2} \tag{A.33}$$

already stated in the main text, Eq. 2.53, expressing that $\delta v_{\text{tot}}$ is essentially given by $h(t)$ plus an additional constant $\Delta_{\text{ne}}$.

## A.7 System-size exponent $\gamma_{\text{ext}}$ for uncorrelated microstates

Let us focus on moments of time series $\mathbf{x}$ obtained for $\Delta t \gg \tau_{\text{b}}$, i.e. the time dependence for $v$ and $\delta v_{\text{ext}}$ becomes irrelevant and $\delta v_{\text{int}} = 0$. Due to the non-ergodicity the $c$-dependence remains relevant, however, and we compute ensemble averages $\langle\ldots\rangle_c$ over all stochastic variables

$$x = \mathbf{E}^m x_m = \frac{1}{N_{\text{m}}} \sum_{m=1}^{N_{\text{m}}} x_m \tag{A.34}$$

compatible with the non-ergodicity constraint of the configuration $c$ considered. $x_m$ stands for the contribution of the microstate $m$. Our task is to compute

$$v = \mathbf{E}^c v_c \text{ and } \Delta_{\text{ne}}^2 = \mathbf{V}^c v_c \text{ for } v_c \equiv \left\langle x^2 \right\rangle_c - \langle x \rangle_c^2. \tag{A.35}$$

We assume that the microscopic states $m$ are completely decorrelated but are characterized by random properties specific and quenched for each given configuration $c$. We set $v_{cm} \equiv \left\langle x_m^2 \right\rangle_c - \langle x_m \rangle_c^2$ for the (in general different) variances of the microscopic variables $x_m$. Using

the independence of the microstates yields

$$v_c = \frac{1}{N_{\rm m}} \times \left( \frac{1}{N_{\rm m}} \sum_m v_{cm} \right) \tag{A.36}$$

$$\mathbf{V}^c v_c = \frac{1}{N_{\rm m}^3} \times \left( \frac{1}{N_{\rm m}} \sum_m \mathbf{V}^m v_{cm} \right) \tag{A.37}$$

where we have used that also the variances $v_{cm}$ are independent stochastic variables. Note that the $m-$averages (brackets) do not depend on $N_{\rm m}$ for large $N_{\rm m}$. Hence,

$$v = \mathbf{E}^c v_c \propto 1/N_{\rm m} \text{ and } \Delta_{\rm ne} \propto 1/N_{\rm m}^{3/2}. \tag{A.38}$$

Using in addition the rescaling $x_m \Rightarrow \sqrt{N_{\rm m}} x_m$ of the stochastic variables mentioned in Sec. 2.7 this confirms the stated exponent $\gamma_{\rm ext} = 1/2$ for uncorrelated microscopic variables with quenched random properties.

This page intentionally left blank.

# Appendix B

# Shear strains, stresses and moduli

## B.1 Shear stress and affine shear modulus

Let us consider a small simple shear strain [108] increment $\gamma$ in the $xy$-plane as it would be used to measure the shear-stress relaxation function $G(t)$ by means of a direct out-of-equilibrium simulation [57, 99, 104, 113]. Assuming that all particle positions $\underline{r}$ follow an imposed "macroscopic" shear in an *affine* manner according to $r_x \to r_x + \gamma\, r_y$ the Hamiltonian $\hat{H}$ of a given configuration changes as [65, 67, 101, 104, 113]:

$$(\hat{H}(\gamma) - \hat{H}(\gamma = 0))/V \approx \hat{\tau}\gamma + \frac{1}{2}\hat{\mu}_A\gamma^2 \text{ for } |\gamma| \ll 1. \tag{B.1}$$

The instantaneous shear stress $\hat{\tau}$ and the instantaneous Born-Lamé coefficient $\hat{\mu}_A$ are thus defined as

$$\hat{\tau} \equiv \hat{H}'(\gamma)/V|_{\gamma=0} \text{ and} \tag{B.2}$$

$$\hat{\mu}_A \equiv \hat{H}''(\gamma)/V|_{\gamma=0} = \hat{\tau}'(\gamma)|_{\gamma=0} \tag{B.3}$$

where a prime denotes a functional derivative with respect to the affine small strain transform. All properties considered here refer to the *excess* contributions due to the potential part of the Hamiltonian, i.e. the ideal contributions are assumed to be integrated out. Assuming a pairwise central conservative potential $\sum_l u(r_l)$ with $r_l$ being the distance between

109

a pair of monomers $l = (i, j)$ and $j > i$, one obtains the excess contributions [68, 104]:

$$\hat{\tau} = \frac{1}{V} \sum_l r_l u'(r_l) \; n_{lx} n_{ly} \quad \text{and} \tag{B.4}$$

$$\hat{\mu}_A = \frac{1}{V} \sum_l \left( r_l^2 u''(r_l) - r_l u'(r_l) \right) n_{lx}^2 n_{ly}^2 + \frac{1}{V} \sum_l r_l u'(r_l) \; (n_{lx}^2 + n_{ly}^2)/2 \tag{B.5}$$

with $\underline{n}_l = \underline{r}_l / r_l$ being the normalized distance vector. Note that Eq. B.4 is strictly identical to the corresponding off-diagonal term of the Kirkwood stress tensor [57, 78, 147]. We remind that the instantaneous general Kirkwood excess stress tensor reads

$$\hat{\sigma}_{\alpha\beta} = \frac{1}{V} \sum_l r_l u'(r_l) \; n_{l\alpha} n_{l\beta} \tag{B.6}$$

with $\alpha$ and $\beta$ denoting the spatial dimensions $x, y, z$. Note also that we have used a symmetric representation for the last term of Eq. B.5 exchanging $x$ and $y$ for the affine transform and averaging over the equivalent $x$ and $y$ directions. This last term automatically takes into account the finite normal pressure of the system. Due to the finite surface tension $\Gamma$ of our free-standing films this term must be included. Similar relations are obtained for the $xz$- and the $yz$-plane. For an isotropic three-dimensional system the averages of all three affine shear moduli are finite and equal. See Refs. [77, 98] for the corresponding expression of the ensemble average of $\hat{\mu}_A$ in terms of the pair correlation functions of the bonded and the non-bonded interactions of the particles needed for our polymer chains (cf. Ch. 3). We generally use $\mu_A = \langle \hat{\mu}_A \rangle$ for the ensemble average as in previous publications [63, 65–68, 77, 95, 98–102, 104, 113]. $\mu_A$ corresponds to $R_A$ in Ch. 2.

## B.2 Stress-fluctuation formula for the shear modulus $\mu$

The affine shear modulus $\mu_A$, being the second strain derivative of the Hamiltonian, is obviously not the shear modulus $\mu$ which is the second derivative of the free energy $A$ [63, 95, 97, 117, 148]. We briefly remind here the demonstration of the stress fluctuation formula

$$\mu = \mu_A - \mu_F \quad \text{with} \quad \mu_F \equiv \beta V \left\langle \delta \tau^2 \right\rangle = \beta V \left( \left\langle \tau^2 \right\rangle - \left\langle \tau \right\rangle^2 \right) \tag{B.7}$$

which is used throughout the thesis.[39] Since for a plain shear strain at constant volume the ideal free energy contribution does not change, i.e. is irrelevant for $\mu$, we may focus on the excess free energy contribution $F_{\text{ex}}(T, \gamma) = -k_B T \ln(Z_{\text{ex}}(\gamma))$ due to the conservative inter-action energy of the particles. The (excess) partition function $Z_{\text{ex}}(0)$ of the unperturbed system at $\gamma = 0$ is the Boltzmann-weighted sum over all states $s$ of the system which are *accessible* within the measurement time $t$. The partition function $Z_{\text{ex}}(\gamma) = \sum_s \exp(-\beta \hat{H}(\gamma))$ of the sheared system is supposed to be the sum over the *same* states $s$, but with a different *metric* corresponding to the macroscopic strain which changes the total interaction energy $\hat{H}(\gamma)$ of state $s$ and, hence, the weight of the sheared configuration for the averages computed. This is the central hypothesis made. Interestingly, it is not necessary to specify explicitly the states of the unperturbed or perturbed system, e.g., it is irrelevant whether the particles are distinguishable or not or whether they have a well-defined reference position for defining a displacement field. We note that

$$\frac{\partial \ln(Z_{\text{ex}}(\gamma))}{\partial \gamma} = \frac{Z'_{\text{ex}}(\gamma)}{Z_{\text{ex}}(\gamma)} \tag{B.8}$$

$$\frac{\partial^2 \ln(Z_{\text{ex}}(\gamma))}{\partial \gamma^2} = \frac{Z''_{\text{ex}}(\gamma)}{Z_{\text{ex}}(\gamma)} - \left(\frac{Z'_{\text{ex}}(\gamma)}{Z_{\text{ex}}(\gamma)}\right)^2 \tag{B.9}$$

for the derivatives of the free energy and

$$\frac{\partial Z_{\text{ex}}(\gamma)}{\partial \gamma} = -\sum_s \beta \hat{H}'(\gamma) \, e^{-\beta \hat{H}(\gamma)} \tag{B.10}$$

$$\frac{\partial^2 Z_{\text{ex}}(\gamma)}{\partial \gamma^2} = \sum_s \left(\beta \hat{H}'(\gamma)\right)^2 e^{-\beta \hat{H}(\gamma)} - \sum_s \left(\beta \hat{H}''(\gamma)\right) e^{-\beta \hat{H}(\gamma)} \tag{B.11}$$

for the derivatives of the excess partition function where a prime denotes the derivative of a function $f(x)$ with respect to its argument $x$. Using Eq. B.10 and taking the limit $\gamma \to 0$ one verifies that the average shear stress is indeed $\tau = \langle \hat{\tau} \rangle$ with $\hat{\tau}$ as defined in Eq. B.2. Note that the average taken is defined as

$$\langle \ldots \rangle = \frac{1}{Z_{\text{ex}}(0)} \sum_s \ldots e^{-\beta \hat{H}(0)} \tag{B.12}$$

---

[39]This is a special case of the more general stress-fluctuation formalism for elastic moduli presented elsewhere [78, 95, 109, 117, 148].

using the weights of the unperturbed system. The shear stress thus measures the average change of the total interaction energy $\hat{H}(\gamma)$ taken at $\gamma = 0$. The shear modulus $\mu$ is obtained using in addition Eq. B.9 and Eq. B.11 and taking finally the $\gamma \to 0$ limit. This thus yields the stress fluctuation formula Eq. B.7 with $\mu_A$ being the excess contribution to the affine shear modulus defined in Eq. B.5.

## B.3   Discussion

We emphasize that the affine shear modulus $\mu_A$ corresponds to the change (second derivative) of the total energy which would be obtained if one actually strains *affinely* in a computer simulation a given state $s$ without allowing the particles to relax their position. As shown for athermal ($T \to 0$) amorphous bodies [115–117], the positions of the particles of such a strained configuration will in general change slightly to minimize the interaction energy relaxing thus the elastic moduli. This is also of relevance for thermalized solids where the non-affine displacements of the particles are driven by the minimization of the free energy. It is for this reason that the shear-stress fluctuation term $\mu_F \geq 0$ must occur in Eq. B.7 correcting the *overprediction*. This point has been overlooked in the early literature [149] and only appreciated much later [97, 115, 116, 148, 150] as discussed in Barrat's review [117]. Interestingly, as has been shown by Lutsko [150], $\mu_F$ and other similarly defined stress fluctuations become temperature independent and may remain finite in the harmonic ground state for $T \to 0$. Probing the stress fluctuations in a low-temperature simulation allows thus to determine the elastic moduli of athermal solids.

112

# Appendix C

# Reminder of viscoelastic properties of the Rouse model

## C.1  Introduction

We summarize here some useful properties of the Rouse model for the dynamics of un-entangled and non-interacting polymer chains in the melt [1, 3, 5, 6]. It is assumed in this model that the static properties of a polymer chain can be represented by a Gaussian chain of featureless beads connected by ideal springs [3]. The typical mean-squared end-to-end distance $R_{\mathrm{e}}^2 = \left\langle (\underline{r}_N - \underline{r}_1)^2 \right\rangle$ between the chain ends at $\underline{r}_1$ and $\underline{r}_N$ is thus given by $R_{\mathrm{e}} = b(N-1)^{1/2}$ with $b$ being the typical spring (bond) length and $N$ the number of monomers of the chains (assumed to be monodisperse). In the Rouse model, the excluded volume interaction and the hydrodynamic interaction are disregarded and the Brownian motion (overdamped dynamics) of the beads with a constant monomer friction constant $\zeta$ is assumed. The motion is described by a linear Langevin equation balancing the frictional forces on each bead with the forces due the chain connectivity and the random Langevin body forces acting independently on each bead [3]. Due to these $N$ uncorrelated forces the chain center of mass freely diffuses with a diffusion constant

$$D = \frac{k_{\mathrm{B}}T}{\zeta N} \tag{C.1}$$

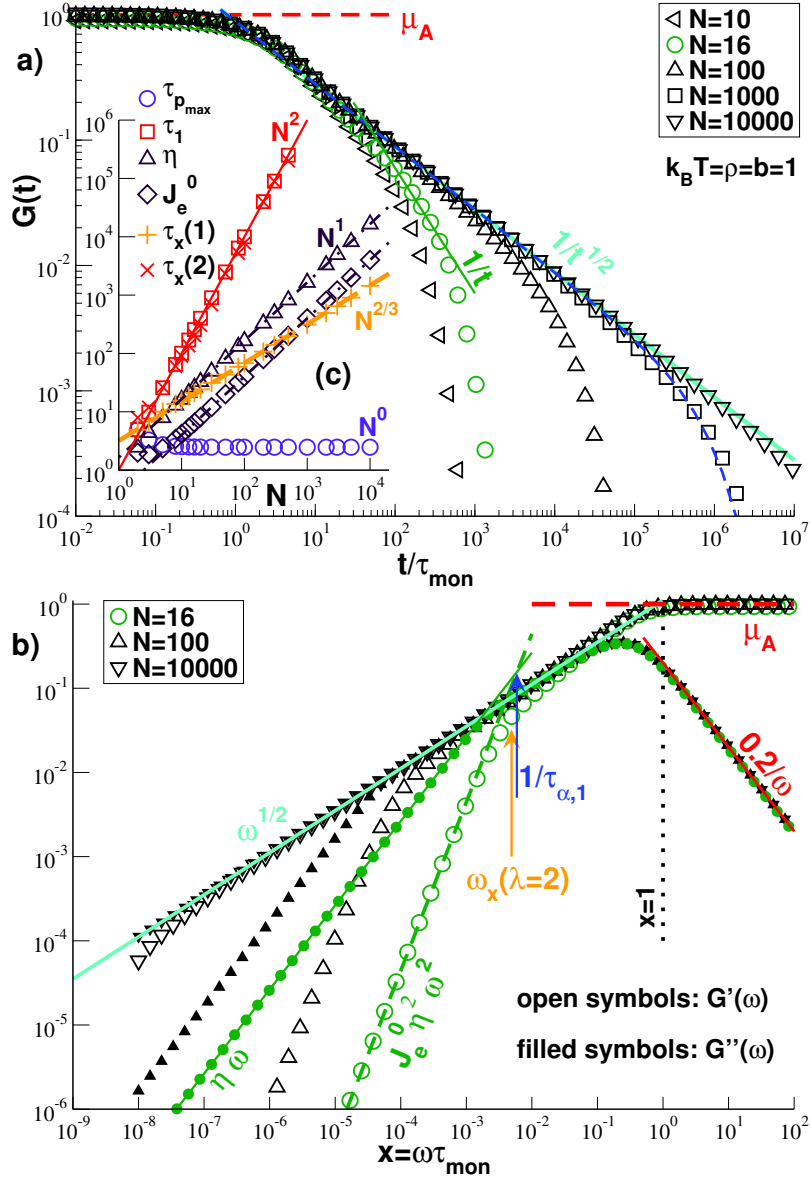with $k_{\mathrm{B}}$ being Boltzmann's constant and $T$ the temperature.

Figure C-1: Various properties of the (discrete) Rouse model for $k_B T = \rho = b = \tau_{mon} = 1$: **(a)** Shear-stress relaxation function $G(t)$ for a broad range of chain lengths $N$. Also indicated are the affine shear modulus $\mu_A$ (dashed horizontal line), Eq. C.3, the power law Eq. C.14 for intermediate times (bold solid line), the Redner-des Cloizeaux formula $\exp(-t/\tau_1)/\sqrt{t}$ for $N = 1000$ (thin solid line) and an effective power low $1/t$ for $N = 16$ (left thin solid line). **(b)** Storage modulus $G'(\omega)$ and loss modulus $G''(\omega)$ for $N = 16$, 100 and 10000. The intermediate power law Eq. C.15 is indicated by a bold solid line, the large-$\omega$ limits of $G'(\omega)$ and $G''(\omega)$ by, respectively, a horizontal dashed line and a thin solid line and the small-$\omega$ limits $G'(\omega) \rightarrow J_e^0 \eta^2 \omega^2$ and $G''(\omega) \rightarrow \eta\omega$ for $N = 16$ by, respectively, thin dashed and thin solid lines. The vertical arrows mark $1/\tau_{\alpha,1}$ and $\omega_\times(\lambda = 2)$ for $N = 16$. **(c)** $\tau_{p_{max}}$, $\tau_1$, $\eta$, $J_e^0$, $\tau_\times(\lambda = 1)$ and $\tau_\times(\lambda = 2)$ $vs$ $N$. $\eta$ and $J_e^0$ increase linearly with $N$ (dash-dotted lines). Note that $\tau_1 \approx \tau_\times(\lambda = 2) \propto N^2$ (solid line) while $\tau_1 \gg \tau_\times(\lambda = 1) \propto N^{2/3}$ (dashed line).

## C.2 Viscoelasticity of discrete Rouse model

Importantly, the Rouse model is a generalized Maxwell model, Eq. 2.25, with constant amplitudes $H_p = k_{\mathrm{B}}T\rho/N$ for $p > 0$ and $R_\infty = 0$. As in the main text, $\rho$ denotes the monomer number density and $\rho/N$ the number density of the chains. The shear-stress relaxation function thus reads [3]

$$G(t) = \frac{k_{\mathrm{B}}T\rho}{N} \sum_{p=1}^{p_{\max}} \exp(-t/\tau_p) \tag{C.2}$$

with $p_{\max} = N - 1$ being set by the chain length $N$.[40] Note that the affine shear modulus

$$\mu_{\mathrm{A}} \equiv G(t=0) = k_{\mathrm{B}}T\rho\, \frac{p_{\max}}{N} \approx k_{\mathrm{B}}T\rho \tag{C.3}$$

becomes rapidly an $N$-independent constant. $\mu_{\mathrm{A}}$ is indicated by the horizontal dashed lines in panel (a) and panel (b) of Fig. C-1 assuming $k_{\mathrm{B}}T = \rho = 1$ and $N \gg 1$. We have yet to specify the relaxation times $\tau_p$ of each mode $p$. It is convenient to define by

$$\tau_{\mathrm{mon}} = \frac{b^2/d}{2\pi^2} \times \frac{\zeta}{k_{\mathrm{B}}T} = \frac{b^2/d}{2\pi^2} \times \frac{1}{DN} \tag{C.4}$$

the "monomer relaxation time" with $d = 3$ being the spatial dimension and using Eq. C.1 in the second step. All time scales are given in Fig. C-1 in units of $\tau_{\mathrm{mon}}$. We also define a function $c_p = (x/\sin(x))^2$ with $x = \pi p/2N$ which encapsulates the deviations of the discrete Rouse model from the continuum Rouse model. As discussed in the standard textbooks [4, 5] it can be demonstrated that

$$\tau_p = \tau_{\mathrm{mon}}\,(N/p)^2 \times c_p = \frac{\tau_1}{p^2} \times \frac{c_p}{c_{p=1}} \tag{C.5}$$

with $\tau_1 = \tau_{\mathrm{mon}}N^2 c_{p=1}$ for $p = 1$ being the largest (terminal) relaxation time of the discrete Rouse model. Note also that

$$\tau_p \to \tau_{p_{\max}} = \frac{b^2}{24} \times \frac{\zeta}{k_{\mathrm{B}}T} \times \frac{1}{\sin^2(\pi/2N)} \text{ for } p \to p_{\max} = N - 1 \text{ and } d = 3. \tag{C.6}$$

---

[40] As the pressure $P$ or the shear stress $\tau$ the shear-stress relaxation function thus has the dimension $[G(t)] = [k_{\mathrm{B}}T][\rho] = \text{energy/volume}$ while the creep compliance $J(t)$ has the dimension $[J(t)] = 1/[G(t)]$.

The stated Eqs. C.2, C.4 and C.5 completely determine (at least numerically) all viscoelastic shear properties of the discrete Rouse model. We have indicated in panel (a) of Fig. C-1 the shear-relaxation function $G(t)$ for several chain lengths $N$ as a function of the reduced time $t/\tau_{\mathrm{mon}}$. Panel (b) presents the storage modulus $G'(\omega)$ (open symbols) and the loss modulus $G''(\omega)$ (filled symbols) obtained using Eq. 2.20 and Eq. 2.21. It is then possible to get the creep compliance $J(t)$ from $G'(\omega)$ and $G''(\omega)$ using [1]

$$J'(\omega) = \frac{G'(\omega)}{G'(\omega)^2 + G''(\omega)^2} \text{ and } J''(\omega) = \frac{G''(\omega)}{G'(\omega)^2 + G''(\omega)^2} \tag{C.7}$$

and by inverse Fourier transform back to $J(t)$. See Appendix D.4 for the Hopkins Hamming method allowing the direct transformation between $G(t)$ and $J(t)$. According to Eq. 2.22 the shear viscosity $\eta$ and steady-state creep compliance $J_e^0$ are given by

$$\eta = (k_B T \rho / N) \sum_{p=1}^{p_{\max}} \tau_p \text{ and } J_e^0 = (k_B T \rho / N) \sum_{p=1}^{p_{\max}} \tau_p^2 \, / \, \eta^2. \tag{C.8}$$

$\tau_{p_{\max}}$, $\tau_1$, $\eta$ and $J_e^0$ are shown in panel (c) of Fig. C-1 as functions of $N$.


## C.3   Continuum limit for large $N$

We have stated the above relations for a discrete Rouse model of finite chain length $N$ since we are concerned in the main part of the thesis and in Appendix D with the description of rather short chains (oligomers) of length $N = 16$. (For this reason $N = 16$ is indicated in Fig. C-1.) It is useful, however, to summarize here also the corresponding relations for the large-$N$ limit which can be computed analytically. Since $c_p \to 1$ for $x = \pi p/2N \to 0$ this leads in leading order to

$$\tau_p \approx \tau_{\mathrm{mon}}(N/p)^2 = \tau_R/p^2 \text{ with } \tau_1 \approx \tau_R \equiv \tau_{\mathrm{mon}}N^2 = \frac{b^2/d}{2\pi^2} \frac{\zeta}{k_B T} N^2 \tag{C.9}$$

being the more familiar Rouse time increasing as $N^2$ with the chain length [3, 6].[41]   As may be seen from panel (c) of Fig. C-1 $\tau_1 \approx \tau_{\mathrm{mon}}N^2$ (solid line) and $\tau_{p_{\max}} \approx \tau_{\mathrm{mon}}N^0$ above $N \approx 10$, i.e. the effects of the correction factor $c_p$ are rapidly negligible. Also indicated is the

---

[41]Note the additional factor 1/2 of the Rouse modes of the generalized Maxwell model compared to the corresponding rotational (diffusional) relaxation times [3].

crossing time $\tau_\times(\lambda)$ determined numerically from Eq. 2.24 for $\lambda \equiv \tan(\delta) \equiv G''(\omega)/G'(\omega)$ with $\lambda = 1$ (pluses) and $\lambda = 2$ (crosses). We emphasize the strong $\lambda$-dependence changing even the asymptotic $N$-dependence with $\tau_1 \gg \tau_\times(\lambda = 1) \propto N^{2/3}$ (dashed line) while $\tau_1 \approx \tau_\times(\lambda = 2) \propto N^2$ (solid line). This suggests that $\lambda$ must be slightly larger than unity to let $\tau_\times(\lambda)$ be a useful measure of the terminal relaxation time. Equation C.8 leads to [1]

$$\eta = S_1 k_B T \rho \tau_{\text{mon}} \times N \text{ and } J_e^0 = \frac{S_2}{S_1^2} \times N/k_B T \rho \qquad (\text{C.10})$$

showing that the shear viscosity $\eta$ and the steady-state creep compliance $J_e^0$ of the Rouse model increase linearly with $N$. This is indicated in panel (c) of Fig. C-1 by the dash-dotted lines. It is used here that the numerical coefficients $S_1$ and $S_2$ are given by

$$S_1 \equiv \sum_{p=1}^{p_{\text{max}}} 1/p^2 \to \pi^2/6 \approx 1.65 \text{ and } S_2 \equiv \sum_{p=1}^{p_{\text{max}}} 1/p^4 \to \pi^4/90 \approx 1.08 \qquad (\text{C.11})$$

for $p_{\text{max}} \to \infty$. Note also that $S_2/S_1^2 \to 0.4$. According to Eq. 2.23 $\tau_{\alpha,1}$ is one often used characterization of the terminal time. We thus have

$$\tau_{\alpha,1} = J_e^0 \eta = \frac{S_2}{S_1} \tau_R = \frac{\pi^2}{15} \tau_R. \qquad (\text{C.12})$$

As can be seen from panel (b) this time corresponds to the frequency where the low-$\omega$ asymptotes of $G'(\omega)$ and $G''(\omega)$ cross. We note *en passant* that in agreement with the general Stokes-Einstein relation [3] the product of viscosity and diffusion constant of the Rouse model

$$\eta D = \frac{1}{36} \frac{k_B T}{b} (\rho b^3) \qquad (\text{C.13})$$

is proportional to the temperature and inversely proportional to a length, the local monomeric scale $b$. As shown elsewhere [1, 3] we have

$$G(t) = \frac{\sqrt{\pi}}{2} k_B T \rho (\tau_{\text{mon}}/t)^{1/2} \text{ for } \tau_R \ll t \ll \tau_{\text{mon}} \qquad (\text{C.14})$$

as indicated by the bold solid line in panel (a). As may be see by Fourier transformation[42] this corresponds to [1, 3]

$$G'(\omega) = G''(\omega) = \frac{\pi}{2\sqrt{2}} k_B T \rho \left( \tau_{mon} \omega \right)^{1/2} \text{ for } 1/\tau_R \ll \omega \ll 1/\tau_{mon}. \qquad \text{(C.15)}$$

As can be seen from panel (b) this does indeed describe the behavior for large Rouse chains, $N \gg 50$, in the intermediate wave-vector regime.

## C.4 Specific Rouse model for tests

We have summarized above some important viscoelastic features of the discrete Rouse model of polymer dynamics. This is used in Appendix D to test and compare various methods for the numerical transformation between the different viscoelastic functions. Arbitrarily, we set $b = k_B T = \rho = 1$ and $\tau_R = 10^4$. We use the same chain length $N = 16$, i.e. $p_{max} = N - 1 = 15$, as in our numerical simulations of polymer films. This implies $\tau_{mon} \approx 39.07$ for the monomer relaxation time. $\eta \approx 988$ for the shear viscosity, $J_e^0 \approx 6.9$ for the steady-state creep compliance and $G(t) \approx 5.5/\sqrt{t}$ for the intermediate time regime $(\tau_{mon} \ll t \ll \tau_R)$ and $G'(\omega) = G''(\omega) \approx 6.9\sqrt{\omega}$ for the intermediate frequency regime $(2\pi/\tau_R \ll \omega \ll 2\pi/\tau_{mon})$.

---

[42] We use here that $\int_0^\infty dt \ \cos(\omega t) \ t^{-1/2} = \int_0^\infty dt \ \sin(\omega t) \ t^{-1/2} = \sqrt{\pi/2\omega}$.

# Appendix D

# Numerical transformations between linear response functions

## D.1  Introduction

We describe here the methods employed for the numerical transformation of the directly computed response function $G(t) = \mu_A - h(t)$ to other experimentally relevant rheological linear response functions. Specifically, we compute the storage and loss moduli $G'(\omega)$ and $G''(\omega)$, as defined in Eq. 2.20 and Eq. 2.21 for general response functions, and the creep compliance $J(t) \equiv \delta\gamma(t)/\delta\tau$ characterizing the shear-strain increment $\delta\gamma(t)$ generated by a shear stress $\delta\tau$ applied at $t = 0$ [1, 6]. These three response functions are discussed in Ch. 5 where we compare our results with real experiments. Many numerical methods have been proposed to perform the conversions [1, 5]. As reminded in Sec. D.2 and Sec. D.3, $G'(\omega)$ and $G''(\omega)$ can be either obtained by direct Fast Fourier Transformation (FFT) [57, 111] or by fitting $G(t)$ to the Generalized Maxwell model, Eq. 2.25, and using then the transformation Eq. 2.26. While it is possible to obtain $J(t)$ from $G'(\omega)$ and $G''(\omega)$ via Eq. C.7 [1], a direct method (skipping the Fourier space) is given by the Hopkins-Hamming (HH) method [5, 73]. This is discussed in Sec. D.4 and Sec. D.5.

## D.2 Technical notes on FFT and SMD

The *computationally* straightforward method to obtain $G'(\omega)$ and $G''(\omega)$ is to Fourier transform $G(t)$ using either a simple Discrete Fourier Transform, Filon's method (being particularly important for high $\omega$) [99, 111] or a Fast Fourier Transform for large $G(t)$-data sets [72]. We made use of the Python's SciPy library function `scipy.fftpack.fft()` which is based on the Cooley-Tukey algorithm [57, 72, 111]. The Cooley-Tukey algorithm works by exploiting the symmetries of the Discrete Fourier Transform. The obtained complex components, with an exception to low-$T$ cases, can be back-transformed to the original time series by using either the CONTIN package [146] or the Python's SciPy library function `scipy.fftpack.ifft()` performing the inverse Laplace transform. The SMD method extracts information from a uniformly sampled time series of $G(t)$ by fitting multiple exponentially decaying modes to the data set, Eq. 2.25. To avoid spurious oscillations at low frequencies one should not use too many modes $p$. Compared to the (completely unbiased) FFT method the SMD method has the advantage that by choosing the distribution of modes, e.g. by insisting on $\tau_p$ as given by Eq. C.5 for the discrete Rouse model (Appendix C.2), or by logarithmically distributing the relaxation times [1], one effectively filters the data. In our case this allows to smooth the data especially in the low-$\omega$ limit where the statistical noise becomes large.

## D.3 Comparison of FFT and SMD for the Rouse model

We have summarized in Appendix C.4 several useful predictions for an ideal Rouse model with $p_{\max} = N - 1$ and $N = 16$. These predictions are indicated in Fig. D-1 by open circles. The dashed lines show the asymptotic low-frequency behavior $G'(\omega) \approx J_{\mathrm{e}}^0 \eta^2 \omega^2$ and $G''(\omega) \approx \eta\omega$ with the known values of the shear viscosity $\eta$ and steady-state creep compliance $J_{\mathrm{e}}^0$. The expected intermediate frequency regime (see Appendix C.4 and Eq. C.15) for $2\pi/\tau_{\mathrm{R}} \ll \omega \ll 2\pi/\tau_{\mathrm{mon}}$ is emphasized by a solid line. Interestingly, deviations are already visible about a decade below the characteristic monomer frequency $2\pi/\tau_{\mathrm{mon}}$. Note that in the high-frequency limit the storage modulus $G'(\omega)$ must level off, $G'(\omega) \to \mu_{\mathrm{A}} \approx 1$, to the "high-frequency elastic modulus" $\mu_{\mathrm{A}}$, Eq. C.3, the loss modulus $G''(\omega)$ is expected to strongly decay as $G''(\omega) \propto 1/\omega$ [104]. These predictions are compared with the numerical results
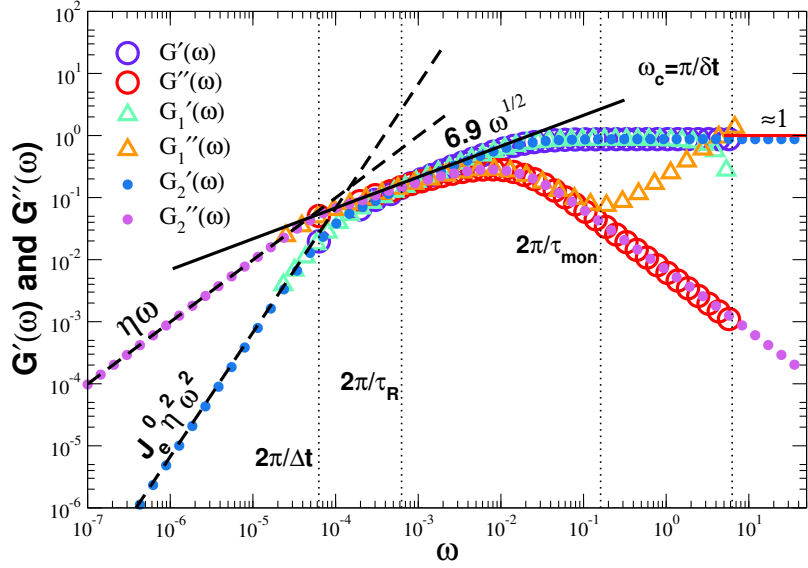
Figure D-1: Comparison of storage and loss moduli $G'(\omega)$ and $G''(\omega)$ of the ideal Rouse model (Sec. 2.4.6) obtained either exactly (open circles) or by means of the FFT method (triangles, labeled $G_1'(\omega)$ and $G_1''(\omega)$) and the SMD method (filled circles, labeled $G_2'(\omega)$ and $G_2''(\omega)$). The vertical dotted lines mark the characteristic frequencies associated to the total sampling time $\Delta t$, the Rouse relaxation time $\tau_R$, the local monomer relaxation time $\tau_{mon}$ and the time increment $\delta t$. The dashed lines indicate the Rouse model prediction for $\omega \ll 2\pi/\tau_R$, Eq. C.10, the solid line the prediction for the intermediate $\omega$-regime, Eq. C.15.

obtained by means of the FFT method and the SMD method. Both methods use $G(t)$-data computed according to Eq. 2.25 (and parameters in Appendix C.4) with a time increment $\delta t = 0.5$ and a total sampling time $\Delta t = 10^5$. The numerical data obtained from the SMD method (filled circles) are excellent in all frequency regimes. At variance to this the FFT method is limited to a more restricted intermediate frequency range. Naturally, only data above $2\pi/\Delta t$ can be obtained with this method and the Nyquist critical frequency $\omega_c = \pi/\delta t \approx 6.2$ [111] sets an upper frequency limit. Note that $G'(\omega)$ deviates for $\omega \approx \omega_c$ due to the well-known "aliasing" of the power spectrum outside of the frequency range $-\omega_c \ll \omega \ll \omega_c$ [146]. Moreover, it is seen that the FFT method shows marked deviations for $G''(\omega)$ already around $2\pi/\tau_{mon}$ from the expected $1/\omega$-decay. In summary, it is an advantage of the SMD method that it allows the extrapolation to much lower and higher frequencies.

## D.4 Hopkins-Hamming (HH) method

Using the Laplace transform $\mathcal{L}[f] = \int_0^\infty f(t) \cdot \exp^{-st} \, dt$ we can state that quite generally for a viscoelastic fluid $\mathcal{L}[\tau(t)] = s \, \mathcal{L}[G(t)] \, \mathcal{L}[\gamma(t)]$ and $\mathcal{L}[\gamma(t)] = s \, \mathcal{L}[J(t)] \, \mathcal{L}[\tau(t)]$ [1]. The shear relation function $G(t)$ and the creep compliance $J(t)$ are thus related by $\mathcal{L}[G(t)] \, \mathcal{L}[J(t)] = 1/s^2$ [1]. As demonstrated elsewhere [5, 131], the latter relation may be represented by the convolution integral

$$\int_0^t G(t - t') \, J(t') \, dt' = t. \tag{D.1}$$

A method for the numerical evaluation of this relation has been proposed by Hopkins and Hamming [5, 73, 131] for linearly or log-spaced input relaxation function. Dividing $J(t)$ to many small, discrete $n$ subintervals, the integral in Eq. D.1 is replaced by the sum

$$t_n = \sum_{i=1}^n J(t_{i-1/2}) \int_{i-1}^i G(t_n - t') \, dt'. \tag{D.2}$$

Here $J(t_{i-1/2})$ is the mean value of $J(t)$ between $t$ and $t_{i-1}$. Therefore we set $t_{i-1/2} = (t_i + t_{i-1})/2$. From the definition $d\eta(t_n - t') = G(t_n - t') \, dt'$, we can substitute for $G(t_n - t')$ in Eq. D.2 to get

$$t_n = -\sum_{i=1}^n J(t_{i-1/2})[\eta(t_n - t_i) - \eta(t_n - t_{i-1})]. \tag{D.3}$$

Separating $i = n$ terms from Eq. D.3, using the assumption $\eta(0) = 0$, and upon rearranging, we obtain the recursive form for the discrete $J(t)$ for $n > 1$ [5]

$$J(t_{n-1/2}) = \frac{t_n + \sum_{i=1}^{n-1} J(t_{i-1/2})[\eta(t_n - t_i) - \eta(t_n - t_{i-1})]}{\eta(t_n - t_{n-1})}. \tag{D.4}$$

The initial condition $n = 1$ is given by

$$J(t_{1/2}) = \frac{2}{G(0) + G(t_1)} = \frac{t_1}{\eta(t_1)}. \tag{D.5}$$

Here the dynamic viscosity $\eta(t)$ for an arbitrary time in the range $(t_0, t_n)$ can be calculated by first integrating[43] $G(t)$ and using linear interpolation. Python's SciPy library function `scipy.interpolate.interp1d()` is a convenient tool for this purpose. A known drawback

---

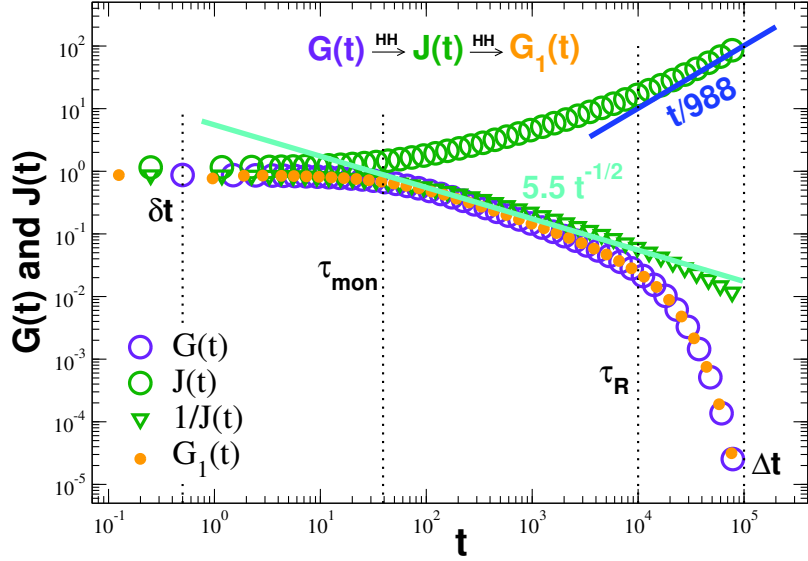[43]Trapezoidal rule was applied to numerically calculate the integral.

Figure D-2: HH transformation of $G(t)$ for the ideal Rouse model, Sec. 2.4.6 using the values given in Sec. C.4. The backward transformation $G_1(t)$ obtained from $J(t)$ and $1/J(t)$ are also shown for comparison. Note that $G_1(t) \approx G(t)$. The asymptotic large-$t$ limit $J(t) \to t/\eta$ is indicated by the thin solids line with $\eta = 988$.

of this method is that the calculated values of $J(t)$ do not correspond to a specific time, but are mean values within a chosen time interval. For this reason, this method is sensitive to fluctuations in the data *corresponding to those times*. On the bright side, these fluctuations does not grow in the subsequent stages of the recursion procedure [73].

## D.5 Creep compliance for Rouse model

Traditionally a creep test is carried out by applying a constant infinitesimally small stress at $t \geq 0$ and observing then the strain response. With the advent of precision motors and actuators, it is experimentally convenient to measure the creep compliance $J(t)$ [15, 16, 19]. Without the need to perform additional simulations, we transform $G(t)$ into $J(t)$ using the HH method described above. One important feature of HH is its backwards compatibility, i.e. it is possible to convert a transformed $J(t)$ back into $G(t)$. We use again as input signal the relaxation function $G(t)$ of the Rouse model described in Appendix C with parameters given in Sec. C.4 and using an equidistant data set with $\delta t = 0.5$ and $\Delta t = 10^5$. The results are shown in Fig. D-2. This confirms the successful transformation of $G(t)$ to $J(t)$ and back from $J(t)$ to $G_1(t) \approx G(t)$. The backward transformation of $J(t)$ to $G_1(t)$ is delicate

for times $t$ below $\delta t$ (corresponding to the above-mentioned Nyquist frequency $\omega_{\mathrm{c}}$) due to the interpolator function of $\eta(t)$ used in the definition. In this limit the function tries to (linearly) interpolate $\eta(t)$ between $\eta(t = 0) = 0$ and the next point from the transformed data. This roughly interpolated data point is then used in the back transformation which propagates the error if multiple forward and backward transformations are performed. This error can be avoided if the provided input data has an appropriate $\eta(t = 0)$ condition defined. (This is the case for our freestanding films.) On the other hand, this small-$t$ error does not propagate further into the recursion. This can be verified by looking at the large-$t$ asymptote $J(t) \to t/\eta$ [1] using the known viscosity $\eta = 988$.

# Bibliography

[1] J. D. Ferry. *Viscoelastic properties of polymers*. John Wiley & Sons, New York, 1980.

[2] P.-G. de Gennes. *Introduction to Polymer Dynamics*. Cambridge University Press, sep 1990. ISBN 9780521381727. doi: 10.1017/CBO9780511569463.

[3] M. Doi and S. F. Edwards. *The Theory of Polymer Dynamics*. Clarendon Press, Oxford, 1986.

[4] W. W. Graessley. *Polymeric Liquids & Networks: Dynamics and Rheology*. Garland Science, London and New York, 2008.

[5] Yn-Hwang. Polymer Viscoelasticity – Basics, Molecular Theories, Experiments and Simulations, 2nd edn, by Yn-Hwang Lin. *Contemporary Physics*, 53(6):524–524, nov 2012. ISSN 0010-7514. doi: 10.1080/00107514.2012.737846.

[6] Michael Rubinstein and Ralph H. Colby. Polymer physics. Edited by Michael Rubinstein and Ralph H Colby Oxford University Press, Oxford, 2003. ISBN 019852059X. pp 440. *Oxford University Press, Oxford*, 2004.

[7] Keiji Tanaka, Jeong Sik Yoon, Atsushi Takahara, Tisato Kajiyama, and Jeong Sik Yoon. Ultrathinning-Induced Surface Phase Separation of Polystyrene/Poly(vinyl methyl ether) Blend Film. *Macromolecules*, 28(4):934–938, 1995. ISSN 15205835. doi: 10.1021/ma00108a021.

[8] J. A. Forrest, K. Dalnoki-Veress, J. R. Stevens, and J. R. Dutcher. Effect of free surfaces on the glass transition temperature of thin polymer films. *Physical Review Letters*, 77(10):2002–2005, 1996. ISSN 10797114. doi: 10.1103/PhysRevLett.77.2002.

[9] J. Mattson, J. A. Forrest, and L. Börjesson. Quantifying glass transition behavior in ultrathin free-standing polymer films. *Phys. Rev. E*, 62:5187, 2000.

[10] James A. Forrest and Kari Dalnoki-Veress. The glass transition in thin polymer films. *Advances in Colloid and Interface Science*, 94(1-3):167–195, 2001. ISSN 00018686. doi: 10.1016/S0001-8686(01)00060-4.

[11] K. Dalnoki-Veress, J. A. Forrest, C. Murray, C. Gigault, and J. R. Dutcher. Molecular weight dependence of reductions in the glass transition temperature of thin, freely standing polymer films. *Phys. Rev. E*, 63:031801, 2001.

[12] O. Bäumchen, J. D. McGraw, J. A. Forrest, and K. Dalnoki-Veress. Reduced glass transition temperatures in thin polymer films: Surface effect or artifact? *Physical*

*Review Letters*, 109(5):1–5, 2012. ISSN 00319007. doi: 10.1103/PhysRevLett.109.055701.

[13] J. A. Forrest and K. Dalnoki-Veress. When does a glass transition temperature not signify a glass transition? *ACS Macro Lett.*, 3:310, 2014.

[14] S. Napolitano, D. Prevosto, M. Lucchesi, P. Pingue, M. D'Acunto, and P. Rolla. Influence of a reduced mobility layer on the structural relaxation dynamics of aluminium capped ultrthin films of poly(ethylene terephthalate). *Langmuir*, 23:2103–2109, 2007.

[15] P. A. O'Connell and G. B. McKenna. Rheological measurements of the thermoviscoelastic response of ultrathin polymer films. *Science*, 307:1760–1763, 2005.

[16] Mataz Alcoutlabi and Gregory B. McKenna. Effects of confinement on material behaviour at the nanometre size scale. *Journal of Physics: Condensed Matter*, 17 (15):R461–R524, apr 2005. ISSN 0953-8984. doi: 10.1088/0953-8984/17/15/R01.

[17] P. A. O'Connell and G. B. McKenna. Novel nanobubble inflation method for determining the viscoelastic properties of ultrathin polymer films. *Review of Scientific Instruments*, 78(1):013901, jan 2007. ISSN 00346748. doi: 10.1063/1.2409777.

[18] P. A. O'Connell and G. B. McKenna. Dramatic stiffening of ultrathin polymer films in the rubbery regime. *European Physical Journal E*, 20(2):143–150, jun 2006. ISSN 12928941. doi: 10.1140/epje/i2005-10125-4.

[19] Paul A. O'Connell, Stephen A. Hutcheson, and Gregory B. McKenna. Creep behavior of ultra-thin polymer films. *Journal of Polymer Science, Part B: Polymer Physics*, 46(18):1952–1965, sep 2008. ISSN 08876266. doi: 10.1002/polb.21531.

[20] P. Chapuis, P. C. Montgomery, F. Anstotz, A. Leong-Hoi, C. Gauthier, J. Baschnagel, G. Reiter, G. B. McKenna, and A. Rubin. A novel interferometric method for the study of the viscoelastic properties of ultra-thin polymer films determined from nanobubble inflation. *Rev. Sci. Instrum.*, 88:093901, 2017.

[21] G. B. McKenna and S. L. Simon. 50th anniversary perspective: Challenges in the dynamics and kinetics of glass-forming polymers. *Macromolecules*, 50:6333, 2017.

[22] C. J. Ellison and J. M. Torkelson. The distribution of glass-transition temperatures in nanoscopically confined glass formers. *Nature Mat.*, 2:695, 2003.

[23] H. Bodiguel and C. Fretigny. Viscoelastic dewetting of a polymer film on a liquid substrate. *Eur. Phys. J. E*, 19:185, 2006.

[24] Z. Yang, Y. Fujii, F.K. Lee, C.-H. Lam, and O.K.C. Tsui. Glass transition dynamics and surface layer mobility in unentangled polystyrene films. *Science*, 328:1676, 2010.

[25] J. E. Pye and C. B. Roth. Two simultaneous mechanisms causing glass transition temperature reductions in high molecular weight freestanding polymer films as measured by transmission ellipsometry. *Phys. Rev. Lett.*, 107:235701, 2011.

[26] Chi Hang Lam and Ophelia K.C. Tsui. Crossover to surface flow in supercooled unentangled polymer films. *Physical Review E - Statistical, Nonlinear, and Soft Matter Physics*, 88(4):1–6, 2013. ISSN 15393755. doi: 10.1103/PhysRevE.88.042604.

[27] S. Herminghaus. Polymer thin films and surfaces: Possible effects of capillary waves. *Eur. Phys. J. E*, 8:237, 2002.

[28] P. Z. Hanakata, J. F. Douglas, and F. W. Starr. Interfacial mobility scale determines the scale of collective motion and relaxation rate in polymer films. *Nature Communications*, 5:4163, 2014.

[29] P.-G. de Gennes. Glass transitions in thin polymer films. *Eur. Phys. J. E*, 2:201, 2000.

[30] S. Mirigian and K. S. Schweizer. Influence of chemistry, interfacial width, and non-isothermal conditions on spatially heterogeneous activated relaxation and elasticity in glass-forming free standing films. *J. Chem. Phys.*, 146:203301, 2017.

[31] S. Merabia, P. Sotta, and D. Long. Heterogeneous nature of the dynamics and glass transition in thin polymer films. *Eur. Phys. J. E*, 15:189, 2004.

[32] A. Dequidt, D. R. Long, S. Merabia, and P. Sotta. Mechanical properties of polymers and nanocomposites close to the glass transition. In C. B. Roth, editor, *Polymer Glasses*, pages 301–354. CRC Press, Taylor & Francis Group, 2016.

[33] S. T. Milner and J. E. G. Lipson. Delayed glassification model for free-surface suppression of $t_g$ in polymer glasses. *Macromolecules*, 43:9865, 2010.

[34] F. Varnik, J. Baschnagel, and K. Binder. Molecular dynamics results on the pressure tensor of polymer films. *Journal of Chemical Physics*, 113(10):4444–4453, 2000. ISSN 00219606. doi: 10.1063/1.1288390.

[35] F. Varnik, J. Baschnagel, and K. Binder. Reduction of the glass transition temperature in polymer films: A molecular-dynamics study. *Phys. Rev. E*, 65:021507, 2002.

[36] Simone Peter, Hendrik Meyer, and J Baschnagel. Thickness-dependent reduction of the glass-transition temperature in thin polymer films with a free surface. *Journal of Polymer Science, Part B: Polymer Physics*, 44(20):2951–2967, oct 2006. ISSN 08876266. doi: 10.1002/polb.20924.

[37] S. Peter, H. Meyer, J. Baschnagel, and R. Seemann. Slow dynamics and glass transition in simulated free-standing polymer films: a possible relation between global and local glass transition temperatures. *Journal of Physics: Condensed Matter*, 19:205118, 2007.

[38] M. Solar, H. Meyer, C. Gauthier, C. Fond, O. Benzerara, R. Schirrer, and J. Baschnagel. Mechanical behavior of linear amorphous polymers: Comparison between molecular dynamics and finite-element simulations. *Phys. Rev. E*, 85:021808, 2012.

[39] J. A. Torres, P. F. Nealey, and J. J. de Pablo. Molecular simulation of ultrathin polymeric films near the glass transition. *Phys. Rev. Lett.*, 85:3221, 2000.

[40] T. S. Jain and J. J. de Pablo. Monte carlo simulation of free-standing polymer films near the glass transition temperature. *Macromolecules*, 35:2167, 2002.

[41] T. R. Böhme and J. J. de Pablo. Evidence for size-dependent mechanical properties from simulations of nanoscopic polymeric structures. *J. Chem. Phys.*, 116:9939, 2002.

[42] K. van Workum and J. J. de Pablo. Computer simulation of the mechanical properties of amorphous polymer nanostructures. *Nano Lett.*, 3:1405, 2003.

[43] K. Yoshimoto, T. S. Jain, P. F. Nealey, and J. J. de Pablo. Local dynamic mechnical properties in model free-standing polymer thin films. *J. Chem. Phys.*, 122:144712, 2005.

[44] A. Shavit and R. A. Riggleman. Influence of backbone rigidity on nanoscale confinement effects in model glass-forming polymers. *Macromolecules*, 46:5044, 2013.

[45] R. J. Lang and D. S. Simmons. Interfacial dynamic length scales in the glass transition of a model freestanding polymer film and their connection to cooperative motion. *Macromolecules*, 46:9818, 2013.

[46] R. J. Lang, W. L. Merling, and D. S. Simmons. Combined dependence of nanoconfined glass transition on interfacial energy and softness of confinement. *ACS Macro Lett.*, 3:758, 2014.

[47] J. H. Mangalara, M. E. Mackura, M. D. Marvin, and D. S. Simmons. The relationship between dynamic and pseudo-thermodynamic measures of the glass transition temperature in nanostructured materials. *J. Chem. Phys.*, 146:1229, 2017.

[48] J. Chowdhury, Y. Guo, Y. Wang, W. L. Merling, J. H. Mangalara, D. S. Simmons, and R. D. Pries. Spatially distributed rheological properties in confined polymers by noncontact shear. *J. Phys. Chem. Lett.*, 8:1229, 2017.

[49] B. D. Vogt. Mechanical and viscoelastic properties of confined amorphous polymers. *J. Polymer Sci., Part B: Poly. Phys.*, 56:9–30, 2018.

[50] T. Gaillard, C. Poulard, T. Voisin, C. Honorez, P. Davidson, W. Drenckhan, and M. Roché. Stable Freestanding Thin Films of Copolymer Melts Far from the Glass Transition. *ACS Macro Letters*, 2015. ISSN 21611653. doi: 10.1021/acsmacrolett. 5b00535.

[51] J. A. Forrest, K. Dalnoki-Veress, and J. R. Dutcher. Interface and chain confinement effects on the glass transition temperature of thin polymer films. *Physical Review E - Statistical Physics, Plasmas, Fluids, and Related Interdisciplinary Topics*, 56(5): 5705–5716, 1997. ISSN 1063651X. doi: 10.1103/PhysRevE.56.5705.

[52] Christopher L. Soles, Jack F. Douglas, and Wen-Li Wu. Dynamics of thin polymer films: Recent insights from incoherent neutron scattering. *Journal of Polymer Science Part B: Polymer Physics*, 42(17):3218–3234, 2004. ISSN 0887-6266. doi: 10.1002/ polb.20172.

[53] Connie B. Roth. *Polymer Glasses.* CRC Press, Boca Raton, FL : CRC Press, Taylor & Francis Group, dec 2016. ISBN 9781315305158. doi: 10.4324/9781315305158.

[54] Kenneth S. Schweizer and David S. Simmons. Progress towards a phenomenological picture and theoretical understanding of glassy dynamics and vitrification near interfaces and under nanoconfinement. *The Journal of Chemical Physics*, 151(24):1–26, dec 2019. ISSN 0021-9606. doi: 10.1063/1.5129405.

[55] James A. Forrest and Kari Dalnoki-Veress. The glass transition in thin polymer films. *Advances in Colloid and Interface Science*, 94(1-3):167–195, 2001. ISSN 00018686. doi: 10.1016/S0001-8686(01)00060-4.

[56] J. L. Keddie, R. A.L. Jones, and R. A. Cory. Size-dependent depression of the glass transition temperature in polymer films. *Epl*, 27(1):59–64, 1994. ISSN 12864854. doi: 10.1209/0295-5075/27/1/011.

[57] M.P. Allen and D.J. Tildesley. *Computer Simulation of Liquids*. Oxford Science, Oxford, 2017.

[58] Steve Plimpton. Fast Parallel Algorithms for Short-Range Molecular Dynamics. *Journal of Computational Physics*, 117(1):1–19, mar 1995. ISSN 00219991. doi: 10.1006/jcph.1995.1039.

[59] Wolfgang Paul. Molecular dynamics simulations of the glass transition in polymer melts. *Polymer (Guildf).*, 45(11):3901–3905, may 2004. ISSN 00323861. doi: 10.1016/j.polymer.2004.01.079.

[60] J Baschnagel and F Varnik. Computer simulations of supercooled polymer melts in the bulk and in confined geometry. *Journal of Physics: Condensed Matter*, 17(32): R851–R953, aug 2005. ISSN 0953-8984. doi: 10.1088/0953-8984/17/32/R02.

[61] J. Baschnagel, I. Kriuchevskyi, J. Helfferich, C. Ruscher, H. Meyer, O. Benzerara, J. Farago, and J. Wittmer. Glass transition and relaxation behavior of supercooled polymer melts: An introduction to modeling approaches by molecular dynamics simulations and to comparisons with mode-coupling theory. In C. Roth, editor, *Polymer glasses*, page 153. Taylor & Francis, 2016.

[62] Kurt Kremer and Gary S. Grest. Dynamics of entangled linear polymer melts: A molecular dynamics simulation. *J. Chem. Phys.*, 92(8):5057–5086, apr 1990. doi: 10.1063/1.458541.

[63] J. P. Wittmer, H. Xu, P. Poliska, F. Weysser, J. Baschnagel, P. Polińska, F. Weysser, J. Baschnagel, P. Poliska, F. Weysser, and J. Baschnagel. Shear modulus of simulated glass-forming model systems: Effects of boundary condition, temperature, and sampling time. *J. Chem. Phys.*, 138(12):12A533, mar 2013. ISSN 00219606. doi: 10.1063/1.4790137.

[64] J.-L. Barrat, J.-N. Roux, J.-P. Hansen, and M L Klein. Elastic Response of a Simple Amorphous Binary Alloy Near the Glass Transition. *EPL (Europhysics Letters)*, 7 (8):707, 1988.

[65] I. Kriuchevskyi, J. P. Wittmer, H. Meyer, O. Benzerara, and J. Baschnagel. Shear-stress fluctuations and relaxation in polymer glasses. *Physical Review E*, 97(1):1–19, 2018. ISSN 24700053. doi: 10.1103/PhysRevE.97.012502.

[66] I Kriuchevskyi, J P Wittmer, H Meyer, and J Baschnagel. Shear Modulus and Shear-Stress Fluctuations in Polymer Glasses. *Physical Review Letters*, 119(14), 2017. ISSN 10797114. doi: 10.1103/PhysRevLett.119.147802.

[67] I. Kriuchevskyi, J. P. Wittmer, O. Benzerara, H. Meyer, and J. Baschnagel. Numerical determination of shear stress relaxation modulus of polymer glasses. *The European Physical Journal E*, 40(4):43, 2017. ISSN 1292-8941. doi: 10.1140/epje/i2017-11535-3.

[68] G. George, I. Kriuchevskyi, H. Meyer, J. Baschnagel, and J. P. Wittmer. Shear-stress relaxation in free-standing polymer films. *Phys. Rev. E*, 98(6):062502, dec 2018. ISSN 2470-0045. doi: 10.1103/PhysRevE.98.062502.

[69] G. George, L. Klochko, A. N. Semenov, J. Baschnagel, and J. P. Wittmer. Ensemble fluctuations matter for variances of macroscopic variables. *European Physical Journal E*, 44(2):1–20, feb 2021. ISSN 1292895X. doi: 10.1140/epje/s10189-020-00004-7.

[70] G. George, L. Klochko, A. N. Semenov, J. Baschnagel, and J. P. Wittmer. Fluctuations of non-ergodic stochastic processes. *The European Physical Journal E*, 44(4): 54, apr 2021. ISSN 1292-8941. doi: 10.1140/epje/s10189-021-00070-5.

[71] S. Herminghaus, K. Jacobs, and R. Seemann. The glass transition of thin polymer films: Some questions, and a possible answer. *European Physical Journal E*, 5(5): 531–538, aug 2001. ISSN 12928941. doi: 10.1007/s101890170036.

[72] James W. Cooley and John W. Tukey. An algorithm for the machine calculation of complex Fourier series. *Mathematics of Computation*, 19(90):297–297, 1965. ISSN 0025-5718. doi: 10.1090/s0025-5718-1965-0178586-1.

[73] I. L. Hopkins and R. W. Hamming. On Creep and Relaxation. *Journal of Applied Physics*, 28(8):906–909, aug 1957. ISSN 0021-8979. doi: 10.1063/1.1722885.

[74] Stephan Herminghaus, Ralf Seemann, and Katharina Landfester. Polymer surface melting mediated by capillary waves. *Physical Review Letters*, 93(1):017801, jul 2004. ISSN 00319007. doi: 10.1103/PhysRevLett.93.017801.

[75] K. Fukao and Y. Miyamoto. Glass transitions and dynamics in thin polymer films: Dielectric relaxation of thin films of polystyrene. *Physical Review E - Statistical Physics, Plasmas, Fluids, and Related Interdisciplinary Topics*, 61(2):1743–1754, 2000. ISSN 1063651X. doi: 10.1103/PhysRevE.61.1743.

[76] Christopher J. Ellison and John M. Torkelson. Sensing the glass transition in thin and ultrathin polymer films via fluorescence probes and labels. *Journal of Polymer Science, Part B: Polymer Physics*, 40(24):2745–2758, 2002. ISSN 08876266. doi: 10.1002/polb.10343.

[77] L. Klochko, J. Baschnagel, J. P. Wittmer, and A. N. Semenov. Relaxation dynamics in supercooled oligomer liquids: From shear-stress fluctuations to shear modulus and structural correlations. *J. Chem. Phys.*, 151:054504, 2019.

[78] Daan Frenkel and Berend Smit. *Understanding Molecular Simulation*. Elsevier, 2002. ISBN 9780122673511. doi: 10.1016/b978-0-12-267351-1.x5000-7.

[79] Petra S. Dittrich and Andreas Manz. Lab-on-a-chip: Microfluidics in drug discovery, mar 2006. ISSN 14741776.

[80] H.A. Stone, A.D. Stroock, and A. Ajdari. Engineering flows in small devices. *Annual Review of Fluid Mechanics*, 36(1):381–411, jan 2004. ISSN 0066-4189. doi: 10.1146/annurev.fluid.36.050802.122124.

[81] Daniel Figeys and Devanand Pinto. Lab-on-a-chip: A revolution in biological and medical sciences. *Analytical Chemistry*, 72(9):330–335, 2000. ISSN 00032700. doi: 10.1021/ac002800y.

[82] Sima Rezvantalab and Mostafa Keshavarz Moraveji. Microfluidic assisted synthesis of PLGA drug delivery systems, jan 2019. ISSN 20462069.

[83] Rosalia Moreddu, Mohamed Elsherif, hadie Adams, Maria Francesca Cordeiro, James S Wolffsohn, Daniele Vigolo, Haider Butt, Jonathan M Cooper, and Ali Kemal Yetisen. Integration of Paper Microfluidic Sensors into Contact Lens for Tear Fluid Analysis. *Lab Chip*, pages –, 2020. doi: 10.1039/D0LC00438C.

[84] Da-Han Kuan and Nien-Tsu Huang. Recent advancements in microfluidics that integrate electrical sensors for whole blood analysis. *Analytical Methods*, 12(26):3318–3332, jul 2020. ISSN 1759-9660. doi: 10.1039/d0ay00413h.

[85] D. Long and F. Lequeux. Heterogeneous dynamics at the glass transition in van der Waals liquids , in the bulk and in thin films. *European Physical Journal E*, 387(3):371–387, mar 2001. ISSN 12928941. doi: 10.1007/s101890170120.

[86] K. L. Johnson, K. Kendall, and A. D. Roberts. Surface energy and the contact of elastic solids. *Proceedings of the Royal Society of London. A. Mathematical and Physical Sciences*, 324(1558):301–313, sep 1971. ISSN 2053-9169. doi: 10.1098/rspa.1971.0141.

[87] J. H. Teichroeb and J. A. Forrest. Direct Imaging of Nanoparticle Embedding to Probe Viscoelasticity of Polymer Surfaces. *Physical Review Letters*, 91(1):1–4, 2003. ISSN 10797114. doi: 10.1103/PhysRevLett.91.016104.

[88] Taskin B. Karim and Gregory B. McKenna. Evidence of surface softening in polymers and their nanocomposites as determined by spontaneous particle embedment. *Polymer*, 52(26):6134–6145, 2011. ISSN 00323861. doi: 10.1016/j.polymer.2011.10.045.

[89] Catherine A. Tweedie, Georgios Constantinides, Karl E. Lehman, Donald J. Brill, Gregory S. Blackman, and Krystyn J. Van Vliet. Enhanced stiffness of amorphous polymer surfaces under confinement of localized contact loads. *Advanced Materials*, 19(18):2540–2546, 2007. ISSN 09359648. doi: 10.1002/adma.200602846.

[90] Jooyoung Chang, Kamil B. Toga, Joseph D. Paulsen, Narayanan Menon, and Thomas P. Russell. Thickness Dependence of the Young's Modulus of Polymer Thin Films. *Macromolecules*, 51(17):6764–6770, 2018. ISSN 15205835. doi: 10.1021/acs.macromol.8b00602.

[91] J. A. Forrest, C. Svanberg, K. Révész, M. Rodahl, L. M. Torell, and B. Kasemo. Relaxation dynamics in ultrathin polymer films. *Physical Review E - Statistical Physics, Plasmas, Fluids, and Related Interdisciplinary Topics*, 58(2):R1226–R1229, 1998. ISSN 1063651X. doi: 10.1103/PhysRevE.58.R1226.

[92] Tisato Kajiyama, Keiji Tanaka, Noriaki Satomi, and Atsushi Takahara. Surface relaxation process of monodisperse polystyrene film based on lateral force microscopic measurements. *Macromolecules*, 31(15):5150–5151, 1998. ISSN 00249297. doi: 10.1021/ma971274i.

[93] Tushar S. Jain and Juan J. De Pablo. Investigation of transition states in bulk and freestanding film polymer glasses. *Physical Review Letters*, 92(15):1–4, 2004. ISSN 00319007. doi: 10.1103/PhysRevLett.92.155505.

[94] Gerold Adam and Julian H. Gibbs. On the temperature dependence of cooperative relaxation properties in glass-forming liquids. *The Journal of Chemical Physics*, 43 (1):139–146, 1965. ISSN 00219606. doi: 10.1063/1.1696442.

[95] B. Schnell, H. Meyer, C. Fond, J. P. Wittmer, and J. Baschnagel. Simulated glass-forming polymer melts: Glass transition temperature and elastic constants of the glassy state. *Eur. Phys. J. E*, 34(9):97, 2011. ISSN 1292895X. doi: 10.1140/epje/i2011-11097-4.

[96] D. R. Squire, A. C. Holt, and W. G. Hoover. Isothermal elastic constants for argon. theory and monte carlo calculations. *Physica*, 42:388, 1969.

[97] J. F. Lutsko. Stress and elastic constants in anisotropic solids: Molecular dynamics techniques. *J. Appl. Phys*, 64:1152, 1988.

[98] H. Xu, J. P. Wittmer, P. Polińska, and J. Baschnagel. Impulsive correction to the elastic moduli obtained using the stress-fluctuation formalism in systems with truncated pair potential. *Phys. Rev. E - Stat. Nonlinear, Soft Matter Phys.*, 86(4):1–9, 2012. ISSN 15393755. doi: 10.1103/PhysRevE.86.046705.

[99] J. P. Wittmer, H. Xu, and J. Baschnagel. Shear-stress relaxation and ensemble transformation of shear-stress autocorrelation functions. *Phys. Rev. E - Stat. Nonlinear, Soft Matter Phys.*, 91(2):1–8, 2015. ISSN 15502376. doi: 10.1103/PhysRevE.91.022107.

[100] J. P. Wittmer, H. Xu, and J. Baschnagel. Simple average expression for shear-stress relaxation modulus. *Phys. Rev. E*, 93(1), 2016. ISSN 24700053. doi: 10.1103/PhysRevE.93.012103.

[101] J P Wittmer, I Kriuchevskyi, A Cavallo, H Xu, and J Baschnagel. Shear-stress fluctuations in self-assembled transient elastic networks. *Phys. Rev. E*, 93(6), 2016. ISSN 24700053. doi: 10.1103/PhysRevE.93.062611.

[102] D. Li, H. Xu, and J. P. Wittmer. Glass transition of two-dimensional 80-20 Kob-Andersen model at constant pressure. *J. Phys. Condens. Matter*, 28(4), 2016. ISSN 1361648X. doi: 10.1088/0953-8984/28/4/045101.

[103] Ivan Kriuchevskyi. *Propriétés mécaniques et viscoélastiques des polymères vitrifiables en volume et en films minces : études par dynamique molèculaire de systèmes modèles.* PhD thesis, Strasbourg, 2017. URL http://www.theses.fr/2017STRAE044.

[104] J P Wittmer, H Xu, O Benzerara, and J Baschnagel. Fluctuation-dissipation relation between shear stress relaxation modulus and shear stress autocorrelation function revisited. *Molecular Physics*, 113(17-18):2881–2893, 2015. ISSN 13623028. doi: 10.1080/00268976.2015.1023225.

[105] J. P. Hansen and I. R. McDonald. *Theory of simple liquids.* Academic Press, New York, 2006. 3nd edition.

[106] W. Götze. *Complex Dynamics of Glass-Forming Liquids: A Mode-Coupling Theory.* Oxford University Press, Oxford, 2009.

[107] P. M. Chaikin and T. C. Lubensky. *Principles of condensed matter physics.* Cambridge University Press, 1995.

[108] E. B. Tadmor, R. E. Miller, and R. S. Elliot. *Continuum Mechanics and Thermodynamics.* Cambridge University Press, Cambridge, 2012.

[109] E. B. Tadmor and R. E. Miller. *Modeling Materials.* Cambridge University Press, Cambridge, 2011.

[110] D. P. Landau and K. Binder. *A Guide to Monte Carlo Simulations in Statistical Physics.* Cambridge University Press, Cambridge, 2000.

[111] William H Press, Saul A Teukolsky, William T Vetterling, and Brian P Flannery. *Numerical Recipes: The Art of Scientific Computing Second Edition.* Cambridge University Press, 2007. ISBN 0-521-43108-5. doi: 10.2307/1269484.

[112] N. G. van Kampen. *Stochastic processes in physics and chemistry.* North-Holland, Amsterdam, 1992.

[113] J. P. Wittmer, I. Kriuchevskyi, J. Baschnagel, and H. Xu. Shear-strain and shear-stress fluctuations in generalized gaussian ensemble simulations of isotropic elastic networks. *Eur. Phys. J. B*, 88:242, 2015.

[114] A. Einstein. On the present status of the radiation problem. *Phys. Zeitschrift*, 10:185, 1909.

[115] J. P. Wittmer, A. Tanguy, J.-L. Barrat, and L. Lewis. Vibrations of amorphous, nanometric structures: When does continuum theory apply? *Europhys. Lett.*, 57:423–429, 2002.

[116] A. Tanguy, J. P. Wittmer, F. Leonforte, and J.-L. Barrat. Continuum limit of amorphous elastic bodies: A finite-size study of low frequency harmonic vibrations. *Phys. Rev. B*, 66:174205, 2002.

[117] J.-L. Barrat. Microscopic elasticity of complex systems. In M. Ferrario, G. Ciccotti, and K. Binder, editors, *Computer Simulations in Condensed Matter Systems: From Materials to Chemical Biology - Vol. 2*, volume 704, pages 287—307. Springer, Berlin and Heidelberg, 2006.

[118] I. Procaccia, C. Rainone, C. A. B. Z. Shor, and M. Singh. Breakdown of nonlinear elasticity in amorphous solids at finite temperatures. *Phys. Rev. E*, 93:063003, 2016.

[119] Da Li, Olivier Greffier, and Hong Xu. Linear viscoelasticity of a two-dimensional glass-former by stress-fluctuation formalism. *Molecular Physics*, 118(2):1–10, 2020. ISSN 13623028. doi: 10.1080/00268976.2019.1597988.

[120] Timothy W. Sirk, Yelena R. Slizoberg, John K. Brennan, Martin Lisal, and Jan W. Andzelm. An enhanced entangled polymer model for dissipative particle dynamics. *The Journal of chemical physics*, 136(13):134903, 2012.

[121] H. Meyer, T. Kreer, A. Cavallo, J. P. Wittmer, and J. Baschnagel. On the dynamics and disentanglement in thin and two-dimensional polymer films. *European Physical Journal: Special Topics*, 141(1):167–172, 2007. ISSN 19516355. doi: 10.1140/epjst/e2007-00035-9.

[122] A. E. Likhtman. Viscoelasticity and Molecular Rheology. In *Polymer Science: A Comprehensive Reference, 10 Volume Set*, volume 1, pages 133–179. 2012. ISBN 9780080878621. doi: 10.1016/B978-0-444-53349-4.00008-X.

[123] W. Humphrey, A. Dalke, and K. Schulten. Vmd-visual molecular dynamics. *J. Molecular Graphics*, 14:33–88, 1996.

[124] M. Plischke and B. Bergersen. *Equilibrium Statistical Physics*. World Scientific, 1994.

[125] G. Szamel and E. Flenner. Emergence of long-range correlations and rigidity at the dynamic glass transition. *Phys. Rev. Lett.*, 107:105505, 2011.

[126] M. Ozawa, T. Kuroiwa, A. Ikeda, and K. Miyazaki. Jamming transition and inherent structures of hard spheres and disks. *Phys. Rev. Lett.*, 109:205701, 2012.

[127] Hajime Yoshino and Francesco Zamponi. Shear modulus of glasses: Results from the full replica-symmetry-breaking solution. *Physical Review E - Statistical, Nonlinear, and Soft Matter Physics*, 90(2), 2014. ISSN 15502376. doi: 10.1103/PhysRevE.90.022302.

[128] C. Klix, F. Ebert, F. Weysser, M. Fuchs, G. Maret, and P. Keim. Glass elasticity from particle trajectories. *Phys. Rev. Lett.*, 109:178301, 2012.

[129] C. L. Klix, G. Maret, and P. Keim. Discontinuous shear modulus determines the glass transition temperature. *Phys. Rev. X*, 5:041033, 2015.

[130] Bernhard Gross. *Mathematical Structure of the Theories of Viscoelasticity*. The Advances in Chemical Physics, Paris, 1953.

[131] Warren F. Knoff and Irving L. Hopkins. An improved numerical interconversion for creep compliance and relaxation modulus. *Journal of Applied Polymer Science*, 16 (11):2963–2972, 1972. ISSN 10974628. doi: 10.1002/app.1972.070161120.

[132] P Chapuis, P C Montgomery, F Anstotz, A. Leong-Hoï, C Gauthier, J Baschnagel, G Reiter, G. B. McKenna, and A Rubin. A novel interferometric method for the study of the viscoelastic properties of ultra-thin polymer films determined from nanobubble

inflation. *Review of Scientific Instruments*, 88(9), 2017. ISSN 10897623. doi: 10.1063/1.5000948.

[133] J. S. Sharp and J. A. Forrest. Thickness dependence of the dynamics in thin films of isotactic poly (methylmethacrylate). *European Physical Journal E*, 12(SUPPL. 1): 85–89, nov 2003. ISSN 12928941. doi: 10.1140/epjed/e2003-01-023-3.

[134] Nicholas W. Tschoegl. *The Phenomenological Theory of Linear Viscoelastic Behavior*. Springer, 1989. ISBN 9783642736049. doi: https://doi.org/10.1002/actp.1990.010410711.

[135] P. A. O'connell and G. B. McKenna. A novel nano-bubble inflation method for determining the viscoelastic properties of ultrathin polymer films. *Scanning*, 30(2): 184–196, mar 2008. ISSN 01610457. doi: 10.1002/sca.20088.

[136] S. Ge, Y. Pu, W. Zhang, M. Rafailovich, J. Sokolov, C. Buenviaje, R. Buckmaster, and R. M. Overney. Shear modulation force microscopy study of near surface glass transition temperatures. *Physical Review Letters*, 85(11):2340–2343, sep 2000. ISSN 00319007. doi: 10.1103/PhysRevLett.85.2340.

[137] S. Alexander. Amorphous solids: their structure, lattice dynamics and elasticity. *Physics Reports*, 296:65 –236, 1998.

[138] H. Liang, Z. Cao, Z. Wang, and A. .V. Dobrynin. Surface stress and surface tension in polymeric networks. *ACS Macro Lett.*, 7:116, 2018.

[139] R Shuttleworth. Surface tension of solids. *Proc. Phys. Soc. {\rm A}*, 63(February 1977):444–457, 1950. ISSN 0370-1298. doi: 10.1088/0370-1298/63/5/302.

[140] P. Müeller, A. Saùl, and F. Leroy. Simple views on surface stress and surface energy concepts. *Adv. Nat. Sci: Nanosci. Nanotechnol*, 5:013002, 2013.

[141] R. D. Schulman, M. Trejo, T. Salez, E. Raphael, and K. Dalnoki-Veress. Surface energy of strained amorphous solids. *Nature Comm.*, 9:982, 2017.

[142] K. Yoshimoto, T. S. Jain, K. van Workum, P. F. Nealey, and J. J. de Pablo. Mechanical heterogeneities in model polymer glasses at small length scales. *Phys. Rev. Lett.*, 93:175501, 2004.

[143] D. Lips and P. Maas. Stress-stress fluctuation formula for elastic constants in the npt ensemble. *Pys. Rev. E*, 97:053022, 2018.

[144] CB Roth and JR Dutcher. Mobility on Different Length Scales in Thin Polymer Films. *Marcel Dekker, N.Y.*, pages 1–38, 2005.

[145] Shin Kawana and Richard A.L. Jones. Character of the glass transition in thin supported polymer films. *Physical Review E - Statistical Physics, Plasmas, Fluids, and Related Interdisciplinary Topics*, 63(2):6, 2001. ISSN 1063651X. doi: 10.1103/PhysRevE.63.021501.

[146] Stephen W. Provencher. CONTIN: A general purpose constrained regularization program for inverting noisy linear algebraic and integral equations, 1982.

[147] J.P.R.B. Walton, D.J. Tildesley, J.S. Rowlinson, and J.R. Henderson. The pressure tensor at the planar surface of a liquid. *Molecular Physics*, 48(6):1357–1368, apr 1983. ISSN 0026-8976. doi: 10.1080/00268978300100971.

[148] D. R. Squire, A. C. Holt, and W. G. Hoover. Isothermal elastic constants for argon. theory and Monte Carlo calculations. *Physica*, 42(3):388–397, 1969. ISSN 0031-8914. doi: 10.1016/0031-8914(69)90031-7.

[149] Max Born and Kun Huang. *Dynamical Theory of Crystal Lattices*. Oxford University Press, 1954.

[150] J. F. Lutsko. Generalized expressions for the calculation of elastic constants by computer simulation. *J. Appl. Phys*, 65:2991, 1989.

**Geevarghese George**

# Propriétés rhéologiques des films polymères minces autoportants

## Résumé

Nous avons démontré que de nombreuses propriétés mécaniques et rhéologiques de films polymères minces autoportants peuvent être calculées à l'aide de simulations de dynamique moléculaire et en appliquant la formule de fluctuation du stress pour le module de cisaillement $\mu$ . Nous avons également transformé numériquement le module de relaxation du stress de cisaillement $G(t)$ pour obtenir plusieurs autres fonctions de réponse linéaires, qui ont ensuite été utilisées pour caractériser le temps de relaxation alpha et pour effectuer une comparaison quantitative avec les expériences. Conformément aux expériences, nous avons également trouvé que de nombreuses propriétés intensives dépendent linéairement de l'inverse de l'épaisseur $(1/H)$ de nos films. Nous avons essayé de comprendre cet effet en utilisant une analyse «résolue par couche» du module de cisaillement. Nous confirmons l'existence de «l'interface souple» de plusieurs diamètres de billes à la surface des films, ce qui confirme la $1/H$ dépendance. Enfin, nous avons caractérisé les fluctuations d'ensemble de nos stresse instantané de cisaillement et de ses moments supérieurs dans des termes généraux en assumant un processus gaussien stationnaire et stochastique. Nous avons observé que ces fonctions s'écartent de la prédiction gaussienne $\delta\mu_{F,G} \sim 1/\sqrt{\Delta t}$ dans la limite non-ergodique pour les faibles températures.

Mots-clés : films minces, films polymères autoportants, dynamique moléculaire, température de transition vitreuse, propriétés rhéologiques, module de cisaillement, fluctuations d'ensemble.

## Résumé en anglais

We demonstrated that many mechanical and rheological properties of thin freestanding polymer films can be calculated using molecular dynamics simulations and by applying the stress-fluctuation formula for the shear modulus $\mu$ . We also numerically transformed the shear-stress response function $G(t)$ to get various other linear response functions, which were then used to characterize the alpha-relaxation time $\tau_\alpha$ and to quantitatively compare with experiments. In accordance with experiments, we also found that many intensive properties depend to leading order linearly on the inverse thickness $(1/H)$ of our films. We tried to understand this effect by using a « layer-resolved » analysis of the shear modulus. We confirm the existence of soft « liquid-like » layers of several bead diameters at the film surfaces confirming the $1/H$ -dependence. Finally, we characterized the ensemble fluctuations of our time dependent instantaneous shear-stresses and its higher moments by assuming a stationary Gaussian process. We saw that these functionals deviate from the Gaussian prediction $\delta\mu_{F,G} \sim 1/\sqrt{\Delta t}$ in the non-ergodic limit for low temperatures.

Keywords : thin films, freestanding polymer films, molecular dynamics, glass transition temperature, rheological properties, shear modulus, local modulus, ensemble fluctuations